Study Of Lepton Flavour Universality Using Top Quark Decays

Zainab Alsolami

Physics Department, Lancaster University

A thesis submitted for the degree of

Doctor of Philosophy

Under the Supervision of Guennadi Borissov

December, 2024

Study Of Lepton Flavour Universality Using Top Quark Decays

Physics Department, Lancaster University

A thesis submitted for the degree of *Doctor of Philosophy.*

Abstract

Lepton flavor universality is one of the most important assumptions in the Standard Model, which states that all leptons (electrons, muons, taus) interact with the W boson with the same strength. This assumption can be tested by measuring the ratio of branching fractions of the decays ($W \to \mu\nu$) and ($W \to e\nu$), denoted by $R(\mu/e)$. To measure this ratio, the efficiency of the muon and electron is determined by using the decay of Z^0 boson to muon and electron. Comparing the number of detected electrons and muons from Z boson decays reveals any efficiency differences between the detector's response to these particles.

The analysis is based on data collected by the ATLAS experiment during Run 2 of the Large Hadron Collider (LHC), from 2015 to 2018. This data corresponds to an integrated luminosity of 140 fb^{-1}. The obtained uncertainty of $R(\mu/e)$ is 0.0064.

In addition to the lepton flavor universality test, our study also investigates the beam position and luminosity measurement for the ATLAS detector during Run 3 of the LHC. This investigation focuses on changes in the beam spot position and partial widths across four runs taken in 2022: the van der Meer (vdM) run, two LHCf runs, and a physics run. A comparison of X, Y, and Z beam spot positions for the investigated runs reveals a consistent shape and direction for the scans in the vdM run and the other runs, with differences due to a crossing angle present in LHCf and physics runs. The symmetry of the scans in terms of the beam spot width was investigated by studying the dependence of the absolute value of the nominal separation. This revealed no asymmetry between the ascending and descending parts of the beam scans.

Acknowledgements

I would like to express my sincere gratitude for the completion of this thesis. Firstly, I would like to acknowledge the invaluable support provided by the Embassy of Saudi Arabia and my country for the opportunity to pursue my academic goals.

I am deeply grateful to Lancaster University, particularly my supervisors, Guennadi and Valerie Lang, and the dedicated staff of the Physics Department, including Sara, Helen, and Deborah, for their guidance and assistance throughout this journey.

I would also like to acknowledge the support of the Top Physics Analysis Group and the Luminosity Group at ATLAS.

I am grateful to my family for their unwavering support. My father's trust and my mother's patience and strength have been instrumental in my success. My three children have inspired me to persevere through challenging times, and I am thankful for their presence in my life.

Finally, I would like to thank my friends for their supportive friendship.

Declaration

Due to the collaborative nature of particle physics research, certain elements of this thesis, such as the definitions of objects, processes and systematic uncertainties, have been adopted from the collaboration. This is explicitly mentioned within the text. In the collaboration, there are data sources and studies that are exclusively available to CERN users. For our study, we have referenced a few of these sources, which are mentioned in the references section. My contribution to this study involved investigating the Z^0 background, including the development of necessary codes, calculation of scale factors, event selection, and providing the histograms for the fitting process. I also created a configuration file for the TRexFitter and fitting procedure and conducted a comprehensive study of systematic uncertainties.

For the beam spot study, I employed n-tuples (data) provided by the luminosity group, after the reconstruction of the beam spot. My contribution to the luminosity study included developing all necessary code for analyzing beam spot position and width. Additionally, I generated all figures and calculations required for this study using these codes. The results of the beam spot studies have been published as a note in CERN documents (CDs) which are available for CERN members only [1].

The thesis has not been submitted, either in whole or in part, for a degree at this, or any other university.

Zainab Alsolami

Contents

List of Tables

List of Figures

Chapter 1

Introduction

Modern physics is built on rigorous experimentation and theoretical frameworks. A central challenge lies in unravelling the fundamental particles that constitute all matter and energy, along with the forces that govern their interactions. Despite remarkable discoveries, numerous fundamental questions about the universe remain unanswered.

In recent years, the Large Hadron Collider (LHC) has enabled groundbreaking studies and discoveries in this area. The LHC is primarily focused on fundamental particles and their interactions, but its impact extends beyond the scope of individual studies. It plays a crucial role in the broader effort to understand the universe's nature and existence.

This study delves into the Standard Model (SM), a foundational framework established in the 1970s within particle physics. The SM has been remarkably successful in explaining observed phenomena, but it has limitations. Discrepancies have emerged in specific areas, including:

Matter-antimatter asymmetry: The imbalance between matter and antimatter in the universe [2].

Neutrino mass: The existence of mass for neutrinos, which the SM predicts as massless [3].

Dark matter: The presence of invisible matter constituting a significant portion of the universe's mass and energy [4].

Hierarchy problem: The vast difference in mass between particles like the Higgs boson and elementary particles like electrons [5].

These inconsistencies suggest the Standard Model might be incomplete. This inquiry aims to contribute to the search for a more comprehensive model by thoroughly examining lepton flavor universality and its potential role in addressing these unresolved questions.

Lepton Flavor Universality (LFU) postulates that leptons of different flavors interact with gauge bosons identically. This principle can be tested by comparing the decay rates (widths) of W bosons produced in top quark decay, which decay into a lepton and a neutrino. This allows for a clean comparison between decays involving different lepton flavors. In this analysis, we utilize the decay of the $W^{\pm}$ boson to electrons and muons.

The analysis is performed using 140 fb^{-1} of pp collision data collected between 2015 and 2018 by the ATLAS detector at the Large Hadron Collider (LHC) at center-of-mass energy $\sqrt{s} = 13$ TeV.

Chapter 2 of this thesis will discuss the Standard Model and lepton flavour universality. Chapter 3 will then describe the ATLAS detector and Monte Carlo simulation. Chapter 4 will focus on the beam spot position and size, as well as the luminosity of the ATLAS detector. Finally, Chapter 5 will describe the study and analysis conducted to obtain the ratio of branching fraction of muons and electrons, to test lepton flavour universality.

Chapter 2

Theory

The Standard Model(SM) and Lepton Flavor Universality (LFU) will be considered in the following sections. We will discuss the processes that are used to test the LFU hypothesis. The first section considers the SM. The second section will discuss the weak interaction and LFU. The two types of weak interaction: the charged current interaction and neutral current interaction will be described in sections three and four, respectively including lepton and quark decays, pseudoscalar mesons decays and b-hadron decays and Z^0 decays Section 5 discusses high-energy processes at colliders and finally section 6, considers the neutral process, including Z^0 decays. In each part, I will describe every process by reviewing the results of previous research conducted in each part.

2.1 The Standard Model

SM has succeeded in laying the foundation for describing subatomic particles and describing the interaction of these particles with each other. The SM has classified the particles into two types, the first of which is fermions, matter particles, which consist of six quarks and six leptons divided into three generations. The first generation is the lightest quarks and leptons and the most stable particles in the model. The higher generations are heavy copies of the first generation and are

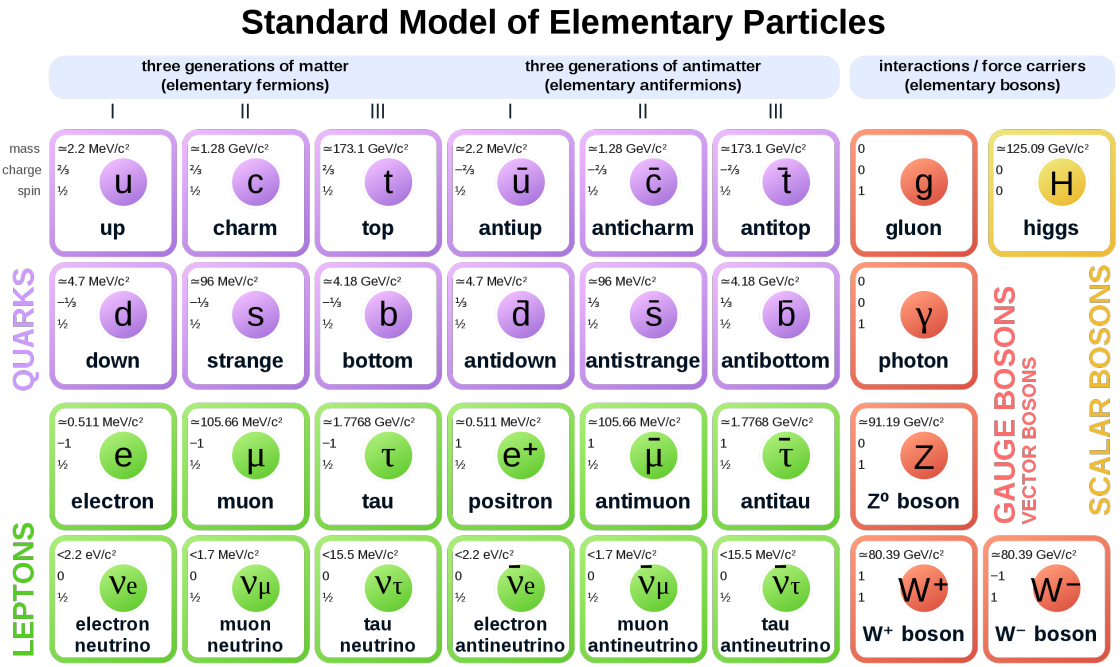

Figure 2.1: This table shows the standard model particles and their associated antiparticle and the force carriers from Ref.[6]

unstable. All three generations participate in similar interactions. The second type is bosons which are four force carriers and one Higgs boson. They are responsible for mediating the fundamental interactions between the various elementary particles. All fermions and bosons have their associated antiparticle which have the same mass and opposite quantum numbers. The Figure 2.1 shows all SM particles fermions, antifermions and bosons.

Quarks and leptons interact via fundamental forces by exchanging gauge bosons: gluons, photons, $W^{\pm}$, and Z^0 bosons.

There are three forces in the SM, the first being a strong force that uses the gluon to mediate the interaction between colour-charged particles (quarks). Quarks are never observed independently due to colour confinement. They usually exist as groups which are called hadrons. Hadrons are either mesons which contain quarks and antiquarks, or baryons which contain three quarks.

The second force is an electromagnetic force mediated by a photon interacting between charged particles, including quarks, and charged leptons. A weak interaction occurs between all particles by the exchange of W and Z^0 bosons. The W boson has a charge of ± 1, the up-type quark charge is $+2/3$ e, and the bottom-type quark charge is $-1/3$ e. Accordingly, "up-type" quarks transform to "bottom-type" quarks, and vice versa. The Z^0 boson is electrically neutral, so it interacts with left-handed and right-handed particles. Weak interactions will be discussed in more detail in the coming sections.

2.2 Weak interaction and lepton flavour universality

Weak interactions are divided into the charge current, associated with the W boson, and the neutral current, associated with the Z^0 boson. We will describe both of them in the sections below.

2.3 Charged current interaction

The weak interaction mediated by the W boson is shown in Figure 2.2, which presents a vertex of weak charged current lepton interaction. This interaction can induce various processes, including electron emission (beta decay) or positron emission, electron capture (absorption), and changing the flavour of a quark and its associated electrical charge. During beta decay, a new quark with a different flavour and charge is created.

The leptonic vertex factor associated with the $W^{\pm}$ boson is shown in Equation.2.1

$$\frac{ig_W}{\sqrt{2}}\frac{1}{2}\gamma^{\mu}\left(1-\gamma^5\right) \tag{2.1}$$

where g_w is the weak coupling constant and γ^{μ} and γ^5 are gamma matrices.

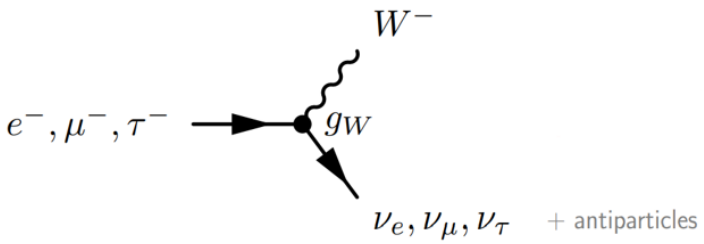

Figure 2.2: The vertex of the weak interaction mediated by the W boson.

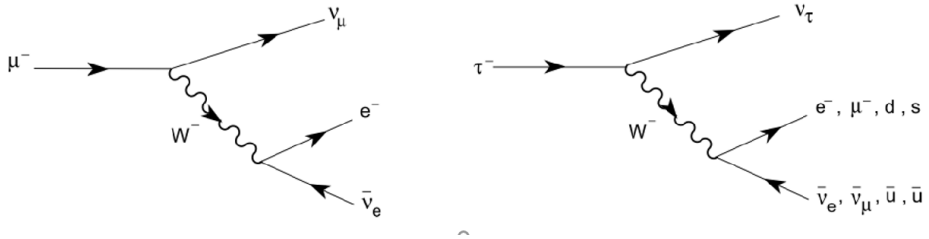

Figure 2.3: Feynman diagram for mu and tau lepton

The coupling strength of leptons g_W from different generations is predicted to be identical with the W boson in $g = g_e = g_\mu = g_\tau$. This assumption of equal coupling strength for different lepton flavours is known as lepton flavour universality (LFU). Table 2.1 shows the experimental measurements of the ratio of coupling constant for tau decays and in light hadron decays. Below we discuss all these results in detail.

2.3.1 Lepton decay

In this section, we will consider how LFU is measured in μ and τ decay through W exchange associated with charged current interactions as shown in Figure2.3.

The partial decay width of leptonic decay muon and tau are written in Equation 2.2, 2.3.

$$\Gamma\left(\mu^- \to e^- \bar{\nu}_e \nu_\mu\right) = \frac{g_e g_\mu m_\mu^5}{192\pi^3} \tag{2.2}$$

$$\Gamma(\tau^- \to e^- \bar{\nu}_e \nu_\mu) = \frac{g_e g_\tau m_\tau^5}{192\pi^3} \tag{2.3}$$

	$\Gamma_{\tau\to\mu}/\Gamma_{\tau\to e}$	$\Gamma_{\pi\to\mu}/\Gamma_{\pi\to e}$	$\Gamma_{K\to\mu}/\Gamma_{K\to e}$	$\Gamma_{K\to\pi\mu}/\Gamma_{K\to\pi e}$	$\Gamma_{W\to\mu}/\Gamma_{W\to e}$
$\lvert g_\mu/g_e\rvert$	1.0018(14)	1.0021(16)	0.9978(20)	1.0010(25)	0.996(10)
	$\Gamma_{\tau\to e}/\Gamma_{\mu\to e}$	$\Gamma_{\tau\to\pi}/\Gamma_{\pi\to\mu}$	$\Gamma_{\tau\to K}/\Gamma_{K\to\mu}$		$\Gamma_{W\to\tau}/\Gamma_{W\to\mu}$
$\lvert g_\tau/g_\mu\rvert$	1.0011(15)	0.9962(27)	0.9858(70)		1.034(13)
	$\Gamma_{\tau\to\mu}/\Gamma_{\mu\to e}$				$\Gamma_{W\to\tau}/\Gamma_{W\to e}$
$\lvert g_\tau/g_e\rvert$	1.0030(15)				1.031(13)

Table 2.1: Experimental measurement for measuring the couplings of W boson in different particles decay modes(tau, pion and kaon decay)and the decay of W boson in the right, these ratios show a good agreement with SM assumption for coupling strength of leptons [7]. The values of the W boson ratio are updated, and we illustrate this in the coming sections.

The lifetime of the leptons τ_l can be calculated by using the total decay width as shown in equation 2.4 where l is μ, τ.

$$\tau_l = \frac{1}{\Gamma} \tag{2.4}$$

In the case of taus, there are different decay modes: it can decay to electrons, muons or light mesons. Then, the lifetime is inversely proportional to it is total width. This is calculated by summing the partial decay widths for each possible decay channel.

Scientists have tested the validity of LFU by measuring the ratio of a particle's partial decay widths for different decay channels. Table 2.1 illustrates the ratio of the coupling constant for different particle decay modes. The Standard Model (SM) predicts these ratios to be equal to one. As can be seen from the table, the values are consistent with the SM expectation.

2.3.2 Quark decay

The weak interaction is the only force that can change the flavor (type) of a quark, for instance, in processes like neutron decay, where a down quark (d) changes into an up quark (u). The Cabibbo hypothesis explains the observed behaviour of weak

interactions between quarks. It proposes that the weak interaction does not directly act on the individual flavors of quarks, but rather on a combination of flavors. Cabibbo introduced an angle called Cabibbo angle (ϕ_C), which quantified the probability of transitions between different quark flavors during weak interactions. The weak interaction eigenstates and mass eigenstates are related by a unitary matrix, now known as the Cabibbo–Kobayashi–Maskawa (CKM) matrix (V_{CKM}).

$$\begin{pmatrix} d' \\ s' \\ b' \end{pmatrix} = V_{CKM} \begin{pmatrix} d \\ s \\ b \end{pmatrix} \tag{2.5}$$

$$V_{CKM} = \begin{pmatrix} V_{ud} & V_{us} & V_{ub} \\ V_{cd} & V_{cs} & V_{cb} \\ V_{td} & V_{ts} & V_{tb} \end{pmatrix} \tag{2.6}$$

$$\sim \begin{pmatrix} \cos\theta_1 & -\sin\theta_1\cos\theta_3 & -\sin\theta_1\sin\theta_3 \\ \sin\theta_1\cos\theta_2 & \cos\theta_1\cos\theta_2\cos\theta_3 - \sin\theta_2\sin\theta_3 e^{i\delta} & \cos\theta_1\cos\theta_2\sin\theta_3 + \sin\theta_2\cos\theta_3 e^{i\delta} \\ \sin\theta_1\sin\theta_2 & \cos\theta_1\sin\theta_2\cos\theta_3 + \cos\theta_2\sin\theta_3 e^{i\delta} & \cos\theta_1\sin\theta_2\sin\theta_3 - \cos\theta_2\sin\theta_3 e^{i\delta} \end{pmatrix}$$

Unlike leptons, which can exist freely, quarks are forever trapped within particles called hadrons due to the strong force, except for the top quark, which decays before hadronizing. This confinement forces quarks to form bound states, the hadrons, that we can observe. Consequently, in weak interactions involving quarks, we can only study the final state of these hadrons, not the individual quarks themselves.

Within hadrons, the relevant properties for weak interactions are the quark "flavors" (up, down, strange, charm, etc.). However, these flavor states don't always directly correspond to the actual quark states involved in the weak interaction. This is why all nine elements of the CKM matrix need to be measured independently. This complex matrix helps us understand the probability of different transitions between quark flavors during weak interactions within hadrons. Current measurements of the CKM matrix elements as presented in Ref.[8] are:

$$|V_{\mathrm{CKM}}| = \begin{pmatrix} 0.97435 \pm 0.00016 & 0.22501 \pm 0.00068 & 0.003732^{+0.000090}_{-0.000085} \\ 0.22487 \pm 0.00068 & 0.97349 \pm 0.00016 & 0.04183^{+0.00079}_{-0.00069} \\ 0.00858^{+0.00019}_{-0.00017} & 0.04111^{+0.00077}_{-0.00068} & 0.999118^{+0.000029}_{-0.000034} \end{pmatrix} \tag{2.7}$$

This matrix provides a complete description of the transitions between all six quark flavors (up, down, charm, strange, top, bottom) during weak interactions.

The charged-current $W^{\pm}$ interactions couple to the physical quarks with couplings given by

$$\mathcal{L}_{CC} = \frac{-g}{\sqrt{2}} \left(\overline{u_L}, \overline{c_L}, \overline{t_L}\right) \gamma^{\mu} W_{\mu}^{+} V_{\mathrm{CKM}} \begin{pmatrix} d_L \\ s_L \\ b_L \end{pmatrix} + h.c. \tag{2.8}$$

Where L are left-handed quark doublets, W_{μ}^{+} is the gauge field for the W^{+} boson and h.c. is the hermitian conjugate (h.c. is another matrix or operator constructed by take the complex conjugate of each element in A and get the (transpose) of A).

Decays of pseudoscalar mesons

Pseudoscalar mesons are mesons with total spin 0 and odd parity.

In this section, we will study leptonic decays of charged pions and kaons, which are unstable particles and decay through weak interaction as shown in Figure 2.4. The primary decay mode for Kaon is leptonic decay with branching fraction $63.55 \pm 0.11\%$. The Kaon decay will be used to probe lepton flavor universality (LFU) by checking for universality between muons and electrons as in Equation (2.9).

$$R_K \equiv \Gamma(K \to e\nu)/\Gamma(K \to \mu\nu) \tag{2.9}$$

This ratio has been tested experimentally $R_K^{exp} = (2.488 \pm 0.010) \cdot 10^{-5}$ [9] and the SM prediction is $R_K^{SM} = (2.477 \pm 0.001) \cdot 10^{-5}$ [10].

The primary decay mode of a pion is a leptonic decay into a muon and a muon neutrino, with a branching fraction of 0.999877. The second most common decay mode of pion, with a branching fraction of 0.000123, is also a leptonic decay into

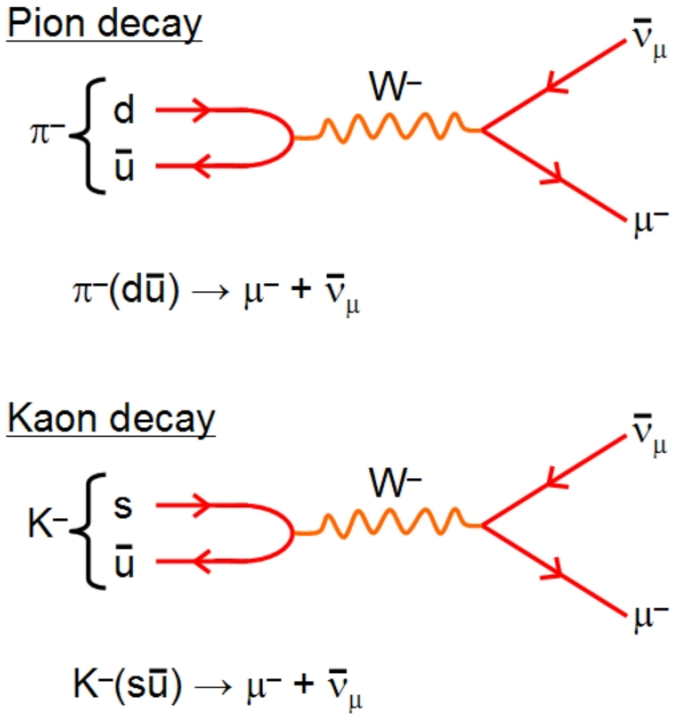

Figure 2.4: Feynman diagram for pion and kaon decay

an electron and the corresponding electron antineutrino. It has provided one of the best tests of e-μ universality in weak interactions for the charged current, giving sensitivity to new physics beyond the SM. The branching ratio of pion decays in Equation.2.10 has been measured as $R^{exp}_{e/\mu} = (1.2344 \pm 0.0023(\text{ stat }) \pm 0.0019(syst)) \times 10^{-4}$ [11] .

$$R_{e/\mu} = \Gamma(\pi^+ \to e^+\nu(\gamma)/\Gamma(\pi^+ \to \mu^+\nu(\gamma)) \tag{2.10}$$

This result is consistent with the prediction of SM $R^{SM}_{e/\mu} = (1.2352 \pm 0.0002) \times 10^{-4}$

Recalling again to Table 2.1 the ratio of coupling constant for decaying kaon and pion is calculated, and it shows a good agreement with the Standard Model.

B-Hadron decay

A B-Hadron contains a heavy bottom quark (b). It can exist in two forms: mesons or baryons. Mesons consist of a bottom quark and an anti-quark of another type (up, down, strange, or charm). And baryons, contain a bottom quark along

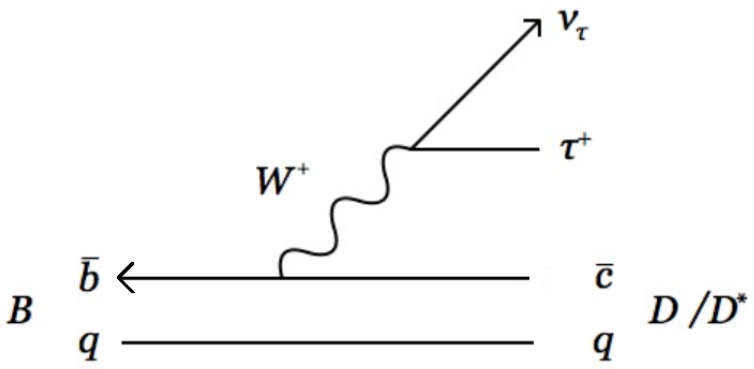

Figure 2.5: Feynman diagram for B meason decay to D

with two other quarks, making them a bit more complex than mesons. All B-mesons have approximately equal masses because the main contribution comes from heavy b-quark and its antiparticle, and approximately the same decay times because each mainly decays the b-quark into a c- or u-quark.

Semi-leptonic B decays of the type $b \to c\tau\nu_\tau$ see Figure 2.5 are good probes for physics beyond SM. Charged Higgs bosons may contribute to this decay due to the large mass of τ and a b-quark. The ratio of $R(D^*)$ Equation 2.11 is measured instead of the absolute branching fraction to reduce the systematic uncertainty. SM predictions for $R(D) = 0.298 \pm 0.004$ and $R(D^*) = 0.254 \pm 0.005$ [12].

$$R_{D^{(*)}} = \frac{Br\left(\bar{B} \to D^*\tau^-\bar{\nu}_\tau\right)}{Br\left(\bar{B} \to D^*\ell^-\bar{\nu}_\ell\right)}, \ell = e, \mu \tag{2.11}$$

The experimental average of this ratio is calculated to be R(D)= 0.344 ± 0.026 $R(D^*) = 0.285 \pm 0.012$ in the Heavy Flavor Averaging Group (HFLAV)[12]. Figure 2.6 shows the range of experimental results from different experiments and its average. This figure shows a tension between the average and SM values.

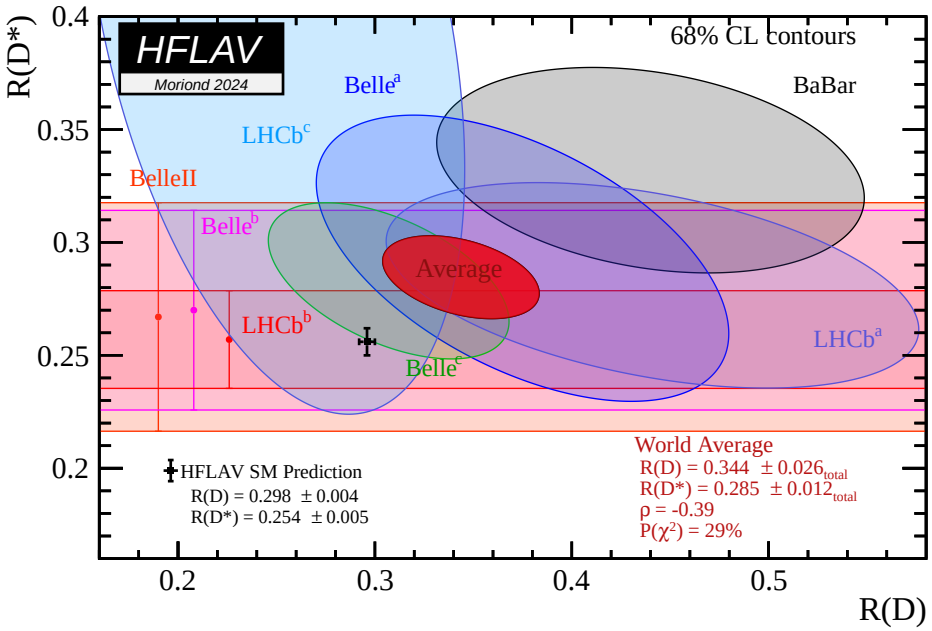

Figure 2.6: The value of different experiment for R(D)and R(D^*) with its average in the red oval [12].

2.4 Neutral current process

2.4.1 Quarkonia decays

Quarkonia are mesons, made up of a quark and its anti-quark, the J/ψ meson(charm and anticharm) is an example. Leptonic decays of quarkonia are used to probe LFU. The leptonic decay width, Γ_{ll}, characterizes the strength of the coupling between the quarkonium state and the lepton pair (e.g., electron-positron or muon-antimuon). The ratio of the leptonic decay widths for electron and muon pairs in the decay of the J/ψ meson(charm-anticharm) tests LFU using direct J/ψ decay measurements.

The branching ratios were measured experimentally at the VEPP-4M collider using the KEDR detector. The result obtained from this experiment is $\Gamma_{e^+e^-}(J/\psi)/\Gamma_{\mu^+\mu^-}(J/\psi) = 1.0022 \pm 0.0044 \pm 0.0048$. [13], and the result of Particle Data Group (PDG) for this decay is 1.0016 ± 0.0031.

2.4.2 Z^0 boson decay

Unlike charged current interactions, the Z^0 boson does not change the flavor of the interacting particles. It can transfer momentum and spin. While the Z^0 boson is the dominant mediator of the neutral current interaction, there are other possible diagrams involving the exchange of charged particles, such as two W bosons, that can contribute to this process but, it is less likely to occur compared to the Z^0 boson exchange.

The Z^0 boson primarily decays into hadrons about 70% of the time. These hadronic decays produce jets of particles. It also decays to pairs of charged leptons: electrons, muons, or tau particles with roughly equal branching ratios (around 10% each). These decays are called leptonic decays. Finally, about 20% of the time, the Z^0 boson decays into neutrinos. Since neutrinos interact very weakly with matter, these decays are invisible to detectors.

Precise measurements of the Z^0 bosons at the Large Electron-Positron (LEP) collider made high-statistics studies of the Z^0 boson's production and decay. The

events of the decays of Z^0 boson to final state l^+l^- ($e^+e^-, \mu^+\mu^-$and $\tau^+\tau^-$) in each experiment are selected with high efficiency. This allows us to probe the universality of the Z^0 boson's couplings to these leptons.

The ratios of decaying Z boson to $(ee, \mu\mu, \tau\tau)$ were measured at ATLAS.

The average value is also taken from the PDG [14] as follows:

$$\Gamma\left(Z \to \mu^+\mu^-\right)/\Gamma\left(Z \to e^+e^-\right) = 1.0001 \pm 0.0024$$

$$\Gamma\left(Z \to \tau^+\tau^-\right)/\Gamma\left(Z \to e^+e^-\right) = 1.0020 \pm 0.003$$

$$\Gamma\left(Z \to \tau^+\tau^-\right)/\Gamma\left(Z \to \mu^+\mu^-\right) = 1.0010 \pm 0.0026$$

These values are in good agreement with the SM.

2.5 LFU studies at high energy in W boson decays

LFU was studied in various experiments from the 1980s to the present, including LEP experiments, LHCb, CMS and ATLAS, by calculating the branching fraction of W boson decay to all possible final states. The LEP experiment (ALEPH, DELPHI, L3, and OPAL) achieved high-precision measurements of the W boson's branching ratios. From all four experiments, the values of W branching fractions are measured as shown in figure 2.7 and then they calculate the ratio of this branching fraction as in Equation 2.12, 2.13 and 2.14 [15].

$$Br\left(\mathrm{W} \to \mu\bar{\nu}_\mu\right)/Br\left(\mathrm{W} \to \mathrm{e}\bar{\nu}_\mathrm{e}\right) = 0.993 \pm 0.019 \tag{2.12}$$

$$Br\left(\mathrm{W} \to \tau\bar{\nu}_\tau\right)/Br\left(\mathrm{W} \to \mathrm{e}\bar{\nu}_\mathrm{e}\right) = 1.063 \pm 0.027 \tag{2.13}$$

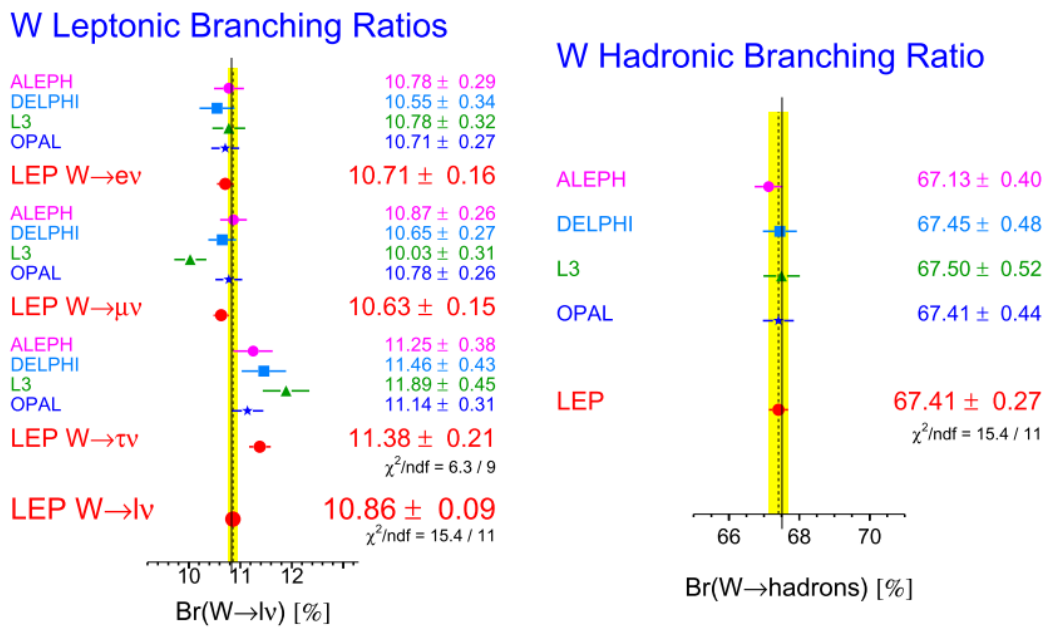

Figure 2.7: W branching fraction for hadronic and leptonic W boson decay in LEP experiments and its averages, recopied from [15]

$$Br\left(\mathrm{W} \to \tau\bar{\nu}_\tau\right)/Br\left(\mathrm{W} \to \mu\bar{\nu}_\mu\right) = 1.070 \pm 0.026 \tag{2.14}$$

In LHCb, the production of $W \to e\nu$ is characterized by a single, isolated high-pT charged particle. The reconstructed electron candidates should have P_T^e over 20 GeV. The differential $W^\pm$ cross-section measurement using electrons is compared to the measurement in the final muon state. Therefore the result determines the W boson's branching fractions to quantify the consistency with lepton flavor universality. $\mathcal{B}(W \to e\nu)/\mathcal{B}(W \to \mu\nu) \quad = 0.980 \pm 0.018$ [16].

In CMS, the value of $Br(\mu/e)$ also measured to be 1.009 ± 0.009 [17].

In ATLAS, the value of $Br(\mu/e)$ is measured by analyzing proton-proton (pp) collision events. These events were selected using triggers that required a single, high-transverse momentum (p_T) and isolated electron or muon. The ratio obtained from this process is $R(\mu/e) = 1.003 \pm 0.010$ [18].

The results of the branching ratio of W are collected, and averages have been

calculated in the Particle Data Group (PDG) as shown in Equations 2.15, 2.16 and 2.17 [14].

$$Br\left(W \to \mu\bar{\nu}_{\mu}\right)/Br\left(W \to e\bar{\nu}_{e}\right) = 1.002 \pm 0.006 \tag{2.15}$$

$$Br\left(W \to \tau\bar{\nu}_{\tau}\right)/Br\left(W \to e\bar{\nu}_{e}\right) = 1.015 \pm 0.02 \tag{2.16}$$

$$Br\left(W \to \tau\bar{\nu}_{\tau}\right)/Br\left(W \to \mu\bar{\nu}_{\mu}\right) = 1.002 \pm 0.02 \tag{2.17}$$

We note that the measured ratios agree well with the Standard Model predictions within a narrow uncertainty range.

2.6 Top quark properties, production and decay

The top quark, with a mass of 175 billion electron volts, is the heaviest particle in the Standard Model. The discovery of this quark was in March 1995 at Fermi National Accelerator Laboratory in Batavia [19]. Based on the Standard Model, the top quark's spin quantum number is 1/2 and the electric charge is +2/3. Due to its huge mass, producing top quarks requires enormous energy. Particle accelerators like the Large Hadron Collider (LHC) achieve these high energies through collisions between protons.

2.6.1 Top quark production

There are two categories of processes to produce top quark: top-pair production and single-top production.

Top quark pair production can occur through the strong interaction via three main processes: the first one is gluon-gluon fusion $gg \to t\bar{t}$, where two gluons fuse to produce a top quark-antiquark pair, this process is the dominant by 90% at LHC [8]. The second one is quark-antiquark annihilation $q\bar{q} \to t\bar{t}$, where a quark and

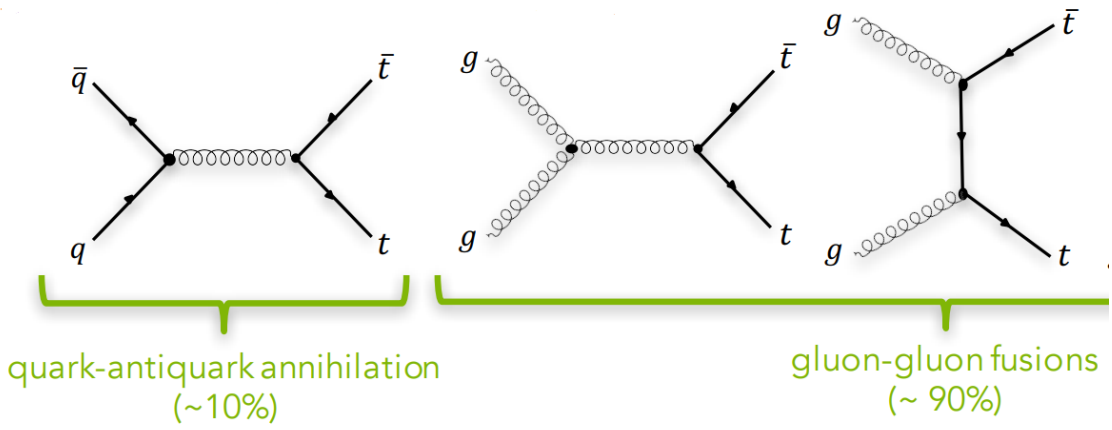

Figure 2.8: Top pair production, quark-anti quark annihilation and gluon-gluon fusion, recopied from [20].

its antiquark annihilate to produce a top quark and its antiparticle. While a third process exists involving the exchange of a W or Z^0 boson (t-channel), it contributes minimally at the Large Hadron Collider (LHC). Figure 2.8 shows Feynman diagrams for the first two top quark pair production processes.

Single-top quark production occurs through the electroweak interaction via three main processes:

S-channel annihilation $q\bar{q}' \rightarrow t\bar{b}$, where a quark and antiquark annihilate to produce a top quark and a bottom quark (anti-b quark), mediated by a virtual W boson. t-channel exchange $q\bar{b} \rightarrow q't$, where a quark interacts with a bottom antiquark, producing a top quark and a different quark, mediated by a W boson exchanged between them. tW-associated production $bg \rightarrow Wt$, where a bottom quark interacts with a gluon to produce a top quark and a W boson. Among these processes, the t-channel exchange is the dominant mode for single-top quark production in proton-proton collisions at the LHC. Figure 2.9 shows the Feynman diagrams for these three processes.

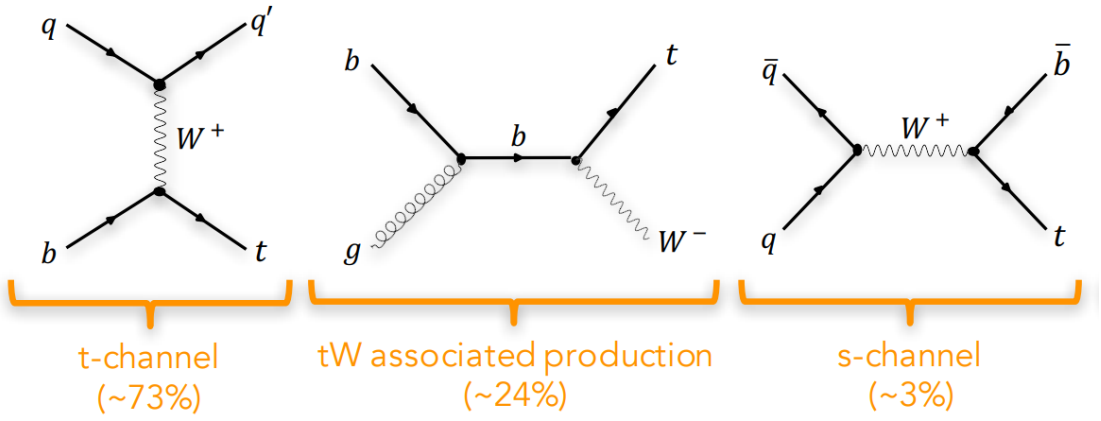

Figure 2.9: Single top quark production:s-channel, t-channel and tw production recopied from [20].

2.6.2 The decay of top quark

Due to its enormous mass, the top quark is extremely unstable. Unlike other quarks, it decays before hadronizing offering a unique opportunity to study it. Furthermore, its large Yukawa coupling with the Higgs boson makes it a particle of particular interest in theories beyond the Standard Model.

The identification of $t\bar{t}$ events at a collider rely solely on detecting their decay products because top quarks have an extremely short lifespan, around 5×10^{-25} seconds. The leading pair-production process decays into a W boson and a bottom quark. The branching ratio of this decay from CKM matrix is equal to $|V_{tb}|^2 = 0.99$ as mentioned in equation 2.7.

Because top quarks are most commonly produced in pairs, and each top quark and its antiparticle (antitop) decay independently, the final state we observe can be any combination of the two possible decay modes for each top quark. Three decay modes for the pair are possible [21]:

Hadronic($t\bar{t} \to W^+bW^-\bar{b} \to q\bar{q}'bq''\bar{q}'''\bar{b}$) (approximately 45.7%): The W boson decays into two quarks (e.g., u and d). This final state produces jets of particles.

Lepton + jets ($t\bar{t} \to W^+bW^-\bar{b} \to q\bar{q}'b\ell^-\bar{\nu}_\ell\bar{b} + \ell^+\nu_\ell bq''\bar{q}'''\bar{b}$)(approximately

43.8%): The W boson decays into a charged lepton (electron, muon, or tau) and a neutrino. This final state includes a lepton and jets of particles.

Dileptonic($t\bar{t} \rightarrow W^+bW^-\bar{b} \rightarrow \ell^+\nu_\ell b\ell'^-\bar{\nu}_{\ell'}\bar{b}$) (approximately 10.5%): The W boson decays into a charged lepton and its corresponding antineutrino (e.g., electron and electron antineutrino). This final state includes two charged leptons .

This research focuses on the decay mode $t \rightarrow bW$, where the W boson further decays into $W^\pm \rightarrow l^\pm + \nu_l (l = e, \mu, \tau)$. According to the Particle Data Group (PDG), the branching fractions for these specific decays are:

$$\Gamma_e/\Gamma_{total} = (11.10 \pm 0.30)\%$$

$$\Gamma_\mu/\Gamma_{total} = (11.40 \pm 0.2)\%$$

$$\Gamma_\tau/\Gamma_{total} = (10.7 \pm 0.5)\%$$

2.7 Summary

This chapter discussed the Standard Model, a highly successful theory that described elementary particles and their interactions. While the limitations of the Standard Model were also addressed, the concept of Lepton Flavor Universality (LFU) and how fermions decay through charged and neutral current interactions were explored. The chapter then examined research on LFU violation in various particle decays. These studies generally supported the predictions of the Standard Model, except for B-hadron decays. This discrepancy highlighted the importance of studying LFU as a potential avenue for uncovering new physics beyond the Standard Model.

Following our discussion of the Standard Model, we described the properties, production, and decay of the top quark, a particle of particular interest to our research. The top quark's decay was then used in Chapter 5 to test Lepton Flavor

Universality (LFU) and calculate the branching ratio of the W boson resulting from this decay.

Chapter 3

Large Hadron Collider and ATLAS experiment

The Large Hadron Collider (LHC) is the most powerful particle accelerator. It exists within a 26.7-kilometre tunnel that was constructed between 1984 and 1989 for CERN's LEP machine [22]. The LHC functions by smashing particles together. It achieves this by colliding two high-energy particle beams travelling at speeds close to the speed of light. This collision disintegrates the particles, allowing scientists to detect the resulting products. The four interaction points are surrounded by four main detectors: ATLAS, CMS, ALICE, and LHCb. Figure 3.1 shows the location of these four detectors on the LHC accelerator.

As this study originates from ATLAS, we will describe it in detail in the following sections.

3.1 ATLAS detector

ATLAS is a versatile particle detector at CERN, designed to investigate both proton-proton (p-p) and heavy ion (A-A) collisions. This cylindrical detector, 46 meters long and 25 meters in diameter, is buried 100 meters underground.

The ATLAS detector is nearly symmetrical around the collision point. It consists

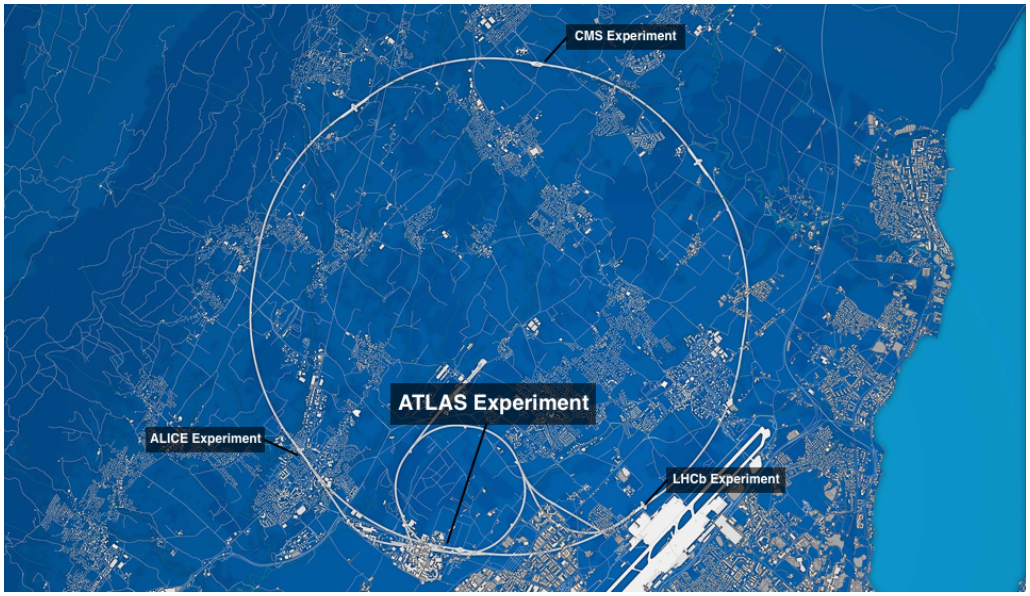

Figure 3.1: LHC ring and the four detectors ATLAS, CMS, ALICE and LHCb

of a large toroid magnet at its core to end the trajectories of charged particles towards the energy detectors. This design allows ATLAS to study particles emerging in all directions from the collision point.

ATLAS has five main parts that work together seamlessly to detect and measure the properties of particles produced in high-energy collisions. Each part plays a crucial role:

- Inner Detector (ID): This device precisely tracks the momentum of each charged particle.
- Calorimeter: This component precisely measures the energy released by the particles.
- Muon Spectrometer: Specifically designed to identify and measure muons.
- Trigger and Data Acquisition System (TDAQ): reduces data collection by selecting only events that meet certain criteria.
- Magnet System: A powerful system of magnets bends the trajectories of charged particles, enabling the measurement of their momentum. In the

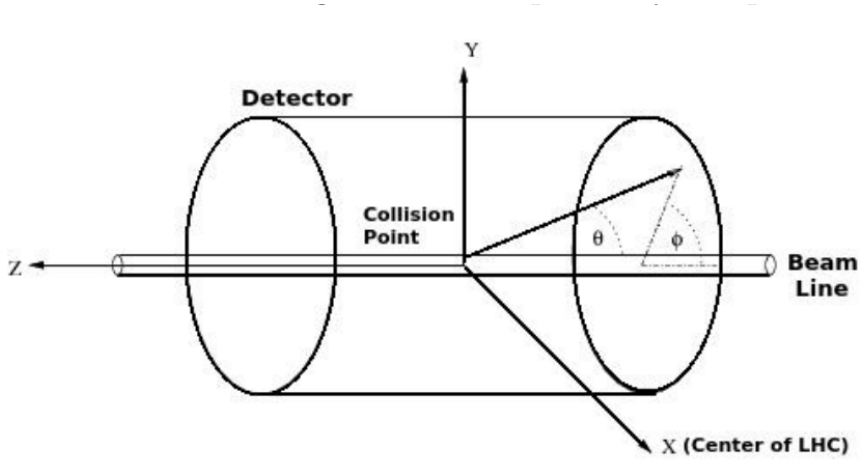

Figure 3.2: The coordinate and cylindrical system of ATLAS detector, reprinted from [23]

following sections, we will delve into each component and explore its unique functionality.

Before we delve into the ATLAS detector's components, we need to explain some important parameters used to describe the detector and collect data.

3.2 Key Parameters for ATLAS Detector Data

In the ATLAS detector, the coordinate system's origin is located at the interaction point. The z-axis is aligned with the direction of the beam, and the x-y plane is transverse to the beam, as shown in Figure 3.2.

In cylindrical coordinates, there are two angles to describe a particle's momentum. The azimuth angle,(ϕ), rotates around the beam axis, starting from zero on the positive x-axis and increasing in a clockwise direction. The polar angle, theta (θ), represents the angle relative to the beam axis itself. Finally, for a particle with momentum $p = (E, p_x, p_y, p_z)$, we can define its rapidity using the following equation.

$$y = \frac{1}{2} \log \frac{E + p_z}{E - p_z}$$

The pseudo-rapidity(η) is defined as:

$$\eta = -\ln \left(tan(\frac{\theta}{2}) \right).$$

For massless particles $y = \eta$.

In terms of η-ϕ, we define a distance measure called ΔR as

$$\Delta R = \sqrt{\Delta\eta^2 + \Delta\phi^2}.$$

Furthermore, several other relevant parameters are important to consider:

The transverse momentum (p_T): is the momentum value in x-y plan.

The transverse impact parameter (d_0): is the shortest distance, measured in the plane perpendicular to the beam axis, between the track and the primary vertex.

The longitudinal impact parameter(z_0): The minimum distance a particle's track gets to the point of collision measured along the beam axis (longitudinal plane).

Missing transverse energy(E_T^{miss}): The total energy of particles that escape undetected in the transverse plane of a particle detector.

3.3 Inner Detector

The Inner Detector (ID) encloses the Large Hadron Collider's (LHC) beam pipe, which is contained within a narrow radius of 36 millimetres. The ID operates in a strong magnetic field of 2 Tesla, produced by the surrounding central solenoid. This cylindrical magnet stretches 5.3 meters in length and reaches a diameter of 2.5 meters. Figure 3.3 shows the main components of the Inner Detector: Pixel Detector, Semiconductor Tracker (SCT), and Transition Radiation Tracker (TRT) [24].

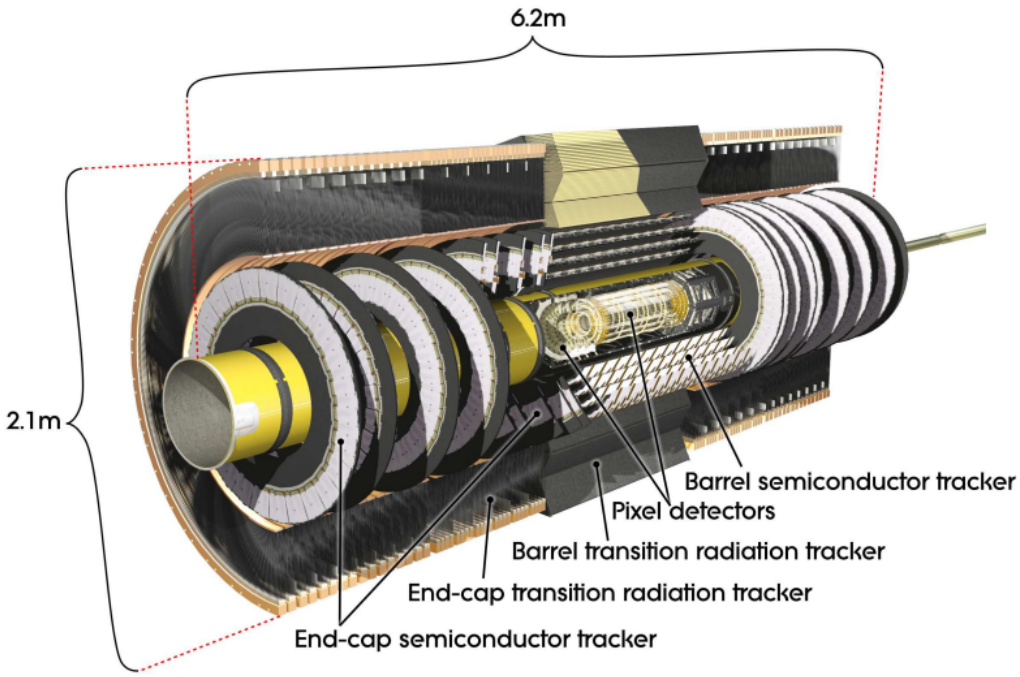

Figure 3.3: Sectional view of the ATLAS inner detector (Reprinted from[24].)

3.3.1 Tracking detectors (Pixels and the semiconductor Tracker (SCT)

The pixel detector consists of high-precision silicon pixel sensors arranged in concentric cylinders around the beam axis in the barrel region and on disks in the end-cap regions. The pixel detector provides the highest granularity measurements, particularly around the vertex region, using identical pixel modules with a minimum pixel size of 50 $\times$ 400 μm^2. It typically has three-pixel layers crossed by each track, with the first layer serving as the "vertexing layer" at a radius of 51 mm. The intrinsic accuracies of the pixel detector are around $10\mu m$ $R-\phi$ and $115\mu m$ (z) in the barrel region, and $10\mu m$ $R-\phi$ and $115\mu m$ (R) in the end-cap regions.

The Semiconductor Tracker (SCT) is another essential component of the ATLAS inner detector. The SCT consists of silicon microstrip detectors arranged in concentric cylinders around the beam axis in the barrel region and of disks in the end-cap regions. Each track typically crosses eight strip layers (four space points)

in the SCT. In the barrel region, the SCT uses small-angle stereo strips to measure both coordinates, with one set of strips in each layer parallel to the beam direction, measuring $R-\phi$. The intrinsic accuracies per module in the SCT are approximately $17\mu m$ $R-\phi$ and 580 μm (z) in the barrel region, and $17\mu m$ $R-\phi$ and $580\mu m$ (R) in the end-cap regions. The SCT provides high-precision tracking capabilities and contributes significantly to the overall performance of the ATLAS inner detector [24].

3.3.2 The Transition Radiation Tracker (TRT)

Transition Radiation Tracker (TRT) is an essential part of the ATLAS inner detector. It is made of straw tubes which are filled with a mixture of xenon-based gas for precise tracking in the barrel and end-cap regions. The TRT is composed of straw tubes with a diameter of about 4mm that provide high granularity and allow track-following up to $|\eta| = 2.0$. The TRT mainly supplies R-ϕ information per straw having an intrinsic precision of approximately one hundred and thirty micrometres. Moreover, it also contributes to electron segment reconstruction and identification as well as complements electromagnetic calorimeter and contributes to the reconstruction and identification of electron track segments.

3.4 Calorimeter

The ATLAS calorimeter system is designed to measure the energy of particles produced in high-energy collisions at the Large Hadron Collider. Calorimeters contain layers of dense material that are designed to absorb most of the particles coming from a collision and measure the energy deposited by these particles. It consists of three main components: the electromagnetic calorimeter (ECAL), the hadronic calorimeter (HCAL) and the forward calorimeter (FCal).

The ECAL is responsible for measuring the energy of electrons and photons. It is divided into a barrel section covering the central region and two end-cap sections

covering the forward regions. The ECAL uses lead absorber layers interspersed with liquid argon as the active medium to detect the electromagnetic showers produced by electrons and photons.

The HCAL, on the other hand, is designed to measure the energy of hadrons such as protons, neutrons, and mesons. It surrounds the ECAL and is divided into a barrel section and two end-cap sections. The HCAL uses layers of steel or plastic as absorbers and scintillators or tiles as the active medium to detect the hadronic showers produced by these particles.

The FCAL is placed at either end of the main detector to capture the particles at very small angles relative to the beam direction. Together, the ECAL and HCAL provide comprehensive energy measurements of particles produced in collisions, allowing for the identification of different types of particles and the reconstruction of the total energy deposited in the calorimeter system.[25]

3.5 Muon Spectrometer

The muon spectrometer is a vital component designed to accurately measure the trajectories and momenta of muons produced in high-energy particle collisions and ignoring most other particles, shown in Figure 3.4. It covers the pseudorapidity range of $|\eta| < 2.7$ and enables the identification of muons with momenta above 3 GeV/c, providing a precise determination of transverse momentum up to about 1 TeV/c. A magnetic field generated by superconducting toroid magnets used to bend muon trajectories, tracking chambers like Monitored Drift Tubes (MDTs) and Cathode Strip Chambers (CSCs) for precise position measurements, a trigger system for efficient event selection, and integration with the inner detector for comprehensive particle measurement. The muon spectrometer plays a crucial role in identifying and studying muons, contributing to the exploration of various physics phenomena and the validation of theoretical models [26].

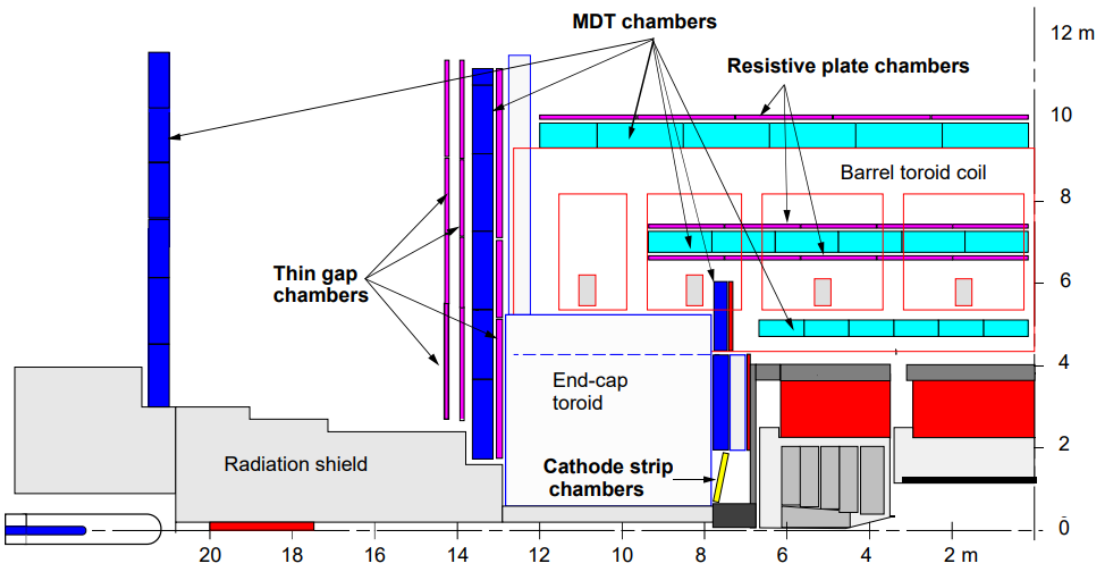

Figure 3.4: ATLAS muon spectrometer(Reprinted from [26])

3.6 Trigger and Data Acquisition System (TDAQ)

The triggering process in the ATLAS experiment involves three levels of event selection: Level 1 (L1), Level 2 (L2), and Event Filter (EF) collectively known as the High-Level Trigger (HLT). The triggering process is designed to capture physics events of interest with high efficiency while effectively reducing the event rate to manageable levels for offline analysis and storage, adapting to changing beam conditions and detector requirements. Level 1 Trigger (L1): The L1 trigger system operates at the full LHC bunch crossing rate of 40 MHz and must make rapid decisions within 2.5 μs to reduce the output rate to 75 kHz. It utilizes data from the calorimeter and muon detectors to make decisions based on energy thresholds and multiplicities of various objects such as electromagnetic clusters, taus, jets, missing transverse energy, and muons.

Level 2 (L2): The L2 algorithms provide a refined analysis of the L1 features using fine-grained detector data and optimal calibrations to improve resolution. L2 algorithms can use detector information not available at L1, such as reconstructed

tracks from the Inner Detector. The L2 system aims to provide additional rejection compared to L1 to reduce the output rate down to around 2 kHz during nominal operations.

Event Filter (EF): The EF is the final online selection stage, running software algorithms on a farm of processors. It receives events accepted by L2 at a rate of 2 kHz and further refines the event selection to reduce the output rate to around 200 Hz. [27].

3.7 Magnet System

The magnet system of the ATLAS detector at the Large Hadron Collider consists of a central solenoid that generates a strong magnetic field of 2 Tesla. This magnetic field extends over a length of 5.3 meters with a diameter of 2.5 meters.

The magnetic field affects the trajectories of charged particles, causing them to curve in the presence of the field. By measuring the curvature of these tracks, the momentum of the particles can be determined. This information is crucial for the identification and reconstruction of the particles produced in high-energy collisions [28].

3.8 Luminosity in the detector

The ATLAS experiment measures a quantity called integrated luminosity. This value reflects the total number of proton-proton collisions that occur during a specific data collection period, typically expressed in units of inverse femtobarn (fb^{-1}). This is especially important when measuring the cross-section, where it is a major source of uncertainty. The same goes for searches of new physics beyond what is predicted - figuring out background levels and how sensitive the experiment requires accurate luminosity measurements. The instantaneous luminosity, $\mathcal{L}$, quantifies the rate (R) of interactions in a process by its proportionality to the process cross-section (σ).

This relationship is expressed as $R = \mathcal{L}\sigma$. The luminosity in proton-proton (pp) collisions at the LHC at a given crossing of proton bunches is given as:

$$\mathcal{L}_b = \frac{\mu \cdot f_{rev} \cdot \Delta t}{\sigma_{inel}} \tag{3.1}$$

Where μ is the expected number of inelastic interactions per bunch crossing, f_{rev} is the revolution frequency of protons in the LHC (=11245.5 Hz), and σ_{inel} is the cross section for inelastic collisions [29]. ATLAS measures collision rates within short intervals called luminosity blocks (LBs). These LBs represent periods where data-taking conditions, including the rate of collisions itself, are assumed to be constant. The ATLAS trigger system defines the start and end of each LB. During Run 2 operations, these LBs were usually one minute long but could be shorter if issues like detector problems arose [30].

ATLAS data collection is structured into runs, these runs typically correspond to a single filling cycle of the LHC, including periods with and without stable beams for collision such as injection, acceleration, and other setup phases. To calculate the integrated luminosity for each run, ATLAS multiplies the average collision rate (L_{inst}) by the duration of each luminosity block (LB) within the run. The resulting values are then stored in the ATLAS database [31]. Within the LHC ring, each proton bunch has a unique identifier called the Bunch Crossing Identifier (BCID). This ID ranges from 0 to 3563, signifying the bunch's specific position along the ring. Which is determined by the maximum number of bunches that the LHC can accommodate. The BCID can also provide timing information about the collision and be used to synchronize the various components of the LHC experiment.

Beam spot and luminosity were studied in chapter 4, and contains a study and analysis of four runs taken in 2022.

3.9 Reconstruction and identification of the key particles produced in the collision

During the collision of particles, thousands of particles can be produced and scattered in all directions within the detector. The type, or identity, of these particles can be determined using various techniques that exploit the unique properties of each particle type. In this section, we will explore the reconstruction and the methods used to identify the key particles produced in these collisions. Relevant particles for the study will be discussed in this section. Figure 3.5 illustrates the reconstruction of various particles in the ATLAS detector. It highlights the detector components that interact with different particle types.

3.9.1 Electron

Electrons interacting with the ATLAS detector leave a trail of ionization and excitation, creating signals in various detector components through produced charged particles and photons.

To reconstruct the electrons, the charged particle tracks in the inner detector in the magnetic field are measured, allowing determination of the particle's momentum and charge.

The energies deposited in the ECAL cells within the cluster are used to estimate the total electromagnetic energy of the cluster. This is because electrons primarily interact with the ECAL. The pre-selection criteria require clusters with electromagnetic energy exceeding 400 MeV, which are likely to originate from electrons or photons. The typical energy released by a minimum ionizing particle (MIP) in the electromagnetic calorimeter is around 100 MeV. This means that the clusters selected by the pre-selection criterion have significantly higher energy than those from MIPs, suggesting they are more likely to be associated with electrons or photons. [32].

These clusters are then matched to one or more tracks detected by the tracking

system. Basic selection criteria are applied to filter out unlikely electron candidates. This might involve cuts based on the momentum of the track, the energy deposited in the ECAL, or the consistency between the track and the shower direction.

Electrons are identified based on a set of criteria that take into account the energy deposition pattern in the calorimeter, the track quality, the matching between the track and the calorimeter cluster, and other discriminating variables. Different identification levels (e.g., loose, medium, tight) [33] are defined based on the selection criteria. The efficiency of electron reconstruction and identification is measured by comparing the reconstructed electrons to known truth-level electrons in simulation or from specific processes. Efficiencies are quantified to understand how well the reconstruction algorithms perform in selecting true electrons.

3.9.2 Photons

Photons interact electromagnetically with the detector material, depositing energy primarily in the electromagnetic calorimeter (ECAL) due to their lack of charge. The energy deposited by photons in the ECAL is used to reconstruct their properties. Photons are identified based on energy deposition patterns and the absence of associated tracks[34].

3.9.3 Jets

Jets are reconstructed through a multi-step process. Calorimeter energy deposits are first grouped into clusters and corrected for their position relative to the collision point. Then, the anti$-k_t$ algorithm, a sophisticated method that considers both energy deposits and distances between particles, is used to cluster these corrected deposits, identifying them as jets [35].

3.9.4 Muons

The reconstruction and identification process of muon includes several steps:

Muons are independently reconstructed in the Inner Detector (ID) and the Muon Spectrometer (MS). Also, information from the energy deposits left in the calorimeters by the muons is used.

Different algorithms are used based on information from ID, MS, and calorimeters [36]. By combining this information and applying specific identification criteria, we ensure accurate reconstruction and identification of muons. There are several ways to identify muons:

Standalone Muons: These muons are reconstructed using only information from the (MS).

Tagged Muons: Tagged muons rely primarily on information from the Inner Detector (ID). However, to confirm the presence of a muon, the information from either the (MS) or the calorimeter was also used.

Combined Muons: This is the most precise method and combines information from both the ID and MS. The ID track is first reconstructed, providing an initial estimate of the muon's trajectory. This ID track is then matched with a compatible track segment in the MS, confirming that the particle penetrated the outer layers of the detector. Finally, a combined fit is performed using data from both the ID and MS [26].

3.10 Monte Carlo simulation(MC)

Due to the complexity involved in the process of proton-proton collisions, describing the final state is very difficult. The simulation process consists of several steps, each handled by different algorithms. A proton is a composite particle that contains partons. A parton is any particle within a hadron that can interact with other particles, such as quarks and gluons. The properties of a parton can be described by the Parton Distribution Functions (PDFs). These functions depend on the parton's longitudinal momentum and the momentum of the parent proton.

Heavy particles can be produced when the momentum transfer between two

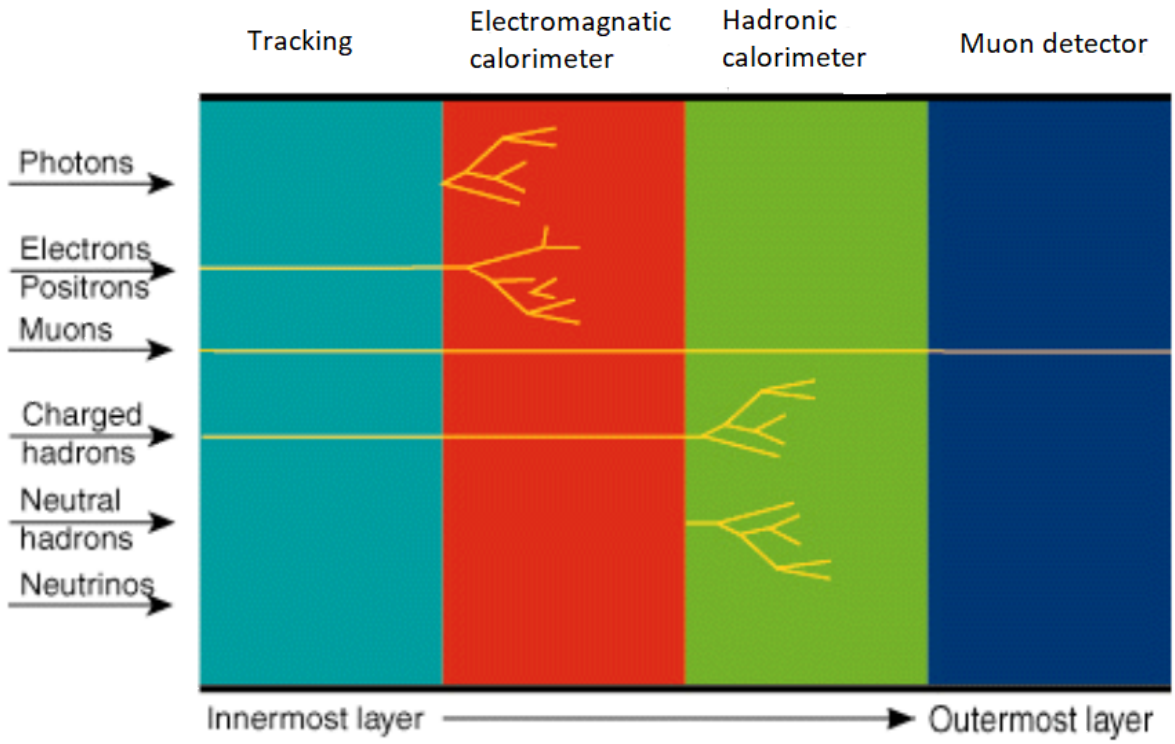

Figure 3.5: Schematic of the different parts of the detector layers and how they interact with different types of particles.(Reprinted from [37])

colliding partons is large. This process is known as **hard scatter** which is the first step of MC simulation. Figure 3.6 shows the different steps of MC simulation with different colours for each step.

- **Hard scatter**

  Monte Carlo (MC) samples of hard scattering events are generated by defining the initial and final state particles. The partonic cross-section of a final state can be calculated using the matrix element. This calculation can then be used to simulate hadron scattering processes.

- **Parton showering** During the parton showering process, partons radiate gluons or split into quark-antiquark pairs. These emitted partons can then radiate even more partons, creating a cascade of emissions. This cascade continues until the emitted partons have low energy, at which point they transform into observable particles through a process called hadronization. The parton shower algorithm describes the decrease in the momentum transfer scale of partons before they combine to form the final particles [38].

- **Hadronization**: Hadronization is the process by which partons (quarks and gluons) transform into colour-neutral final-state hadrons that can be observed in particle detectors. The hadronization process occurs after the parton showering phase in Monte Carlo event generators for hadron colliders.

  Two widely used models for hadronization:

  - String Model: Hadrons are formed by colour strings connecting quarks and antiquarks.
  - Cluster Model: Partons are grouped into clusters based on colour flow, and these clusters evolve into hadrons through a series of transitions[38].

- **Underlying event** The underlying event refers to the additional activity in a high-energy hadron collision that is not associated with the primary hard scatter process. In a typical hadron collision, the primary interaction involves

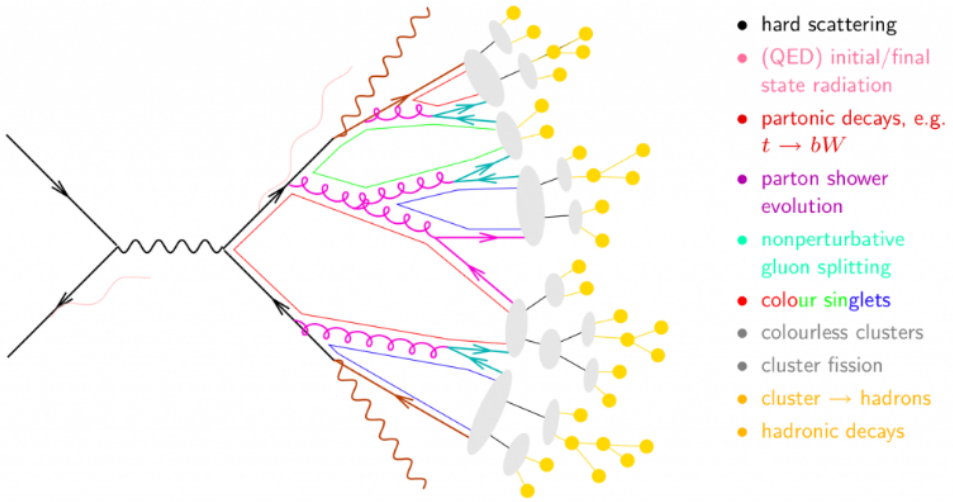

Figure 3.6: A schematic diagram shows the different stages and development of a proton-proton collision in MC simulation. (unknown source)

the scattering of partons (quarks or gluons) at high momentum transfers, leading to the production of high-energy particles. MC event generators incorporate models for simulating the underlying event, which is essential for accurately predicting the full final state of a hadron collision.

- **Pile-up**

  Pile-up arises from the dense concentration of protons in the colliding bunches, resulting in multiple interactions occurring in a single bunch crossing. Dealing with pile-up is a significant challenge, as it can impact the identification of interesting physics processes and increase background noise in the data. Different modeling and correction techniques can effectively handle the challenges posed by pile-up. MC simulate these events by overlaying multiple inelastic pp collisions obtained with a generator called Pythia8. A definition of different generators will be presented in the next section of this chapter. [39].

3.10.1 Detector simulation

This simulation is essential for understanding the response of the detector to various particles and processes. Simulated particles are propagated through a detailed model of the detector geometry and response. These simulations provide a realistic representation of how particles traverse the detector layers and interact with the detector materials. Geant4 is a widely used toolkit for detector simulation [40].

3.10.2 Event simulation tools (generators)

Several Monte Carlo simulation generators exist, and we will define some of the ones used in this study in Chapter 5.

Herwig [41]: This generator is general-purpose and can handle both leading-order (LO) and next-to-leading-order (NLO) hard scattering processes. Its strength lies in providing a comprehensive description of the subsequent stages, including Parton showering, hadronization, and particle decay.

Sherpa[42]: Sherpa is an all-in-one generator for LHC collisions. It excels at simulating final states with many jets by merging NLO calculations with showering algorithms.

Madgraph [43]: This generator also calculates LO and NLO QCD scattering processes. It introduces one-loop corrections and removes double-counting with parton showers, leading to weighted events (positive or negative) that average out to positive final distributions.

Pythia [44]: This is another leading generator that provides precise modelling of QCD and QED radiation, especially suited for small-angle emissions, often used with higher-order matrix elements generators like Madgraph or Powheg.

Powheg[45]: is a tool for interfacing NLO calculations with showering generators (unlike Madgraph, which directly generates events). Powheg produces positive weight events by filtering unlikely emissions, while Madgraph uses negative weights to handle overlap with showering.

evtgen[46]: It can be used to generate entire events, including the initial

state particles, final state particles, and their momenta. This generator accurately simulates bottom and charm quarks, integrating with showering tools like Pythia or Herwig.

3.11 Summary

In this chapter, we have described the main components of the ATLAS detector, the luminosity of the collision point, and the reconstruction and identification of key particles relevant to this study. And described the Monte Carlo simulation and the relevant generators used in our study in Chapter 5. The following chapter will focus on the reconstruction and properties of beam spots in Run 3 data collected in 2022.

Chapter 4

A study of beam position and luminosity measurement for Run-3 in ATLAS detector

4.1 Introduction

The Large Hadron Collider(LHC) [47], is a complex and powerful particle accelerator. LHC relies on understanding and controlling interaction region and interaction rate, reflected in the beam spot and the luminosity to increase the efficiency of collisions. The beam spot, a tiny region where the two beams of particles collide, is of paramount importance as it directly influences the collision rate and the amount of data collected by the LHC experiments. A smaller beam spot enhances the likelihood of head-on collisions, providing more information about the interacting particles.

Luminosity is defined as a measure of the collision rate. However, maintaining a stable and well-defined beam spot and luminosity poses significant challenges. Their knowledge is essential for accurate interpretation of the data collected by the LHC experiments and for ensuring the safe and efficient operation of the machine.

The parameters of th e single-Gaussian model of bunch densities and their impact

on the luminosity calibration by the van der Meer method were studied in [48]. It was determined that the single-Gaussian model can be used to accurately describe the linear movement of the beam spot but, high-separation scan data necessitates a more sophisticated approach to account for the beam spot's non-linear behaviour.

Protons in the LHC beam are not continuously distributed but organized into bunches separated by short gaps. The number of bunches, the number of protons per bunch, and the spacing between bunches are critical parameters for studying the properties of the beam spot. Through a fitting process, we can calculate various properties of the beam spot, including its size, position, shape, tilt, stability, and intensity. This process is called beam spot reconstruction and it will be described in section 4.2.

This study investigated the development of the beam spot's position and width during several scans recorded by the ATLAS detector at a center-of-mass energy of 13.6 TeV in 2022. The reconstruction of the beam spot is described in section 4.2. Several runs were used for this comparison: one vdM run, two LHCf runs, and one physics run. These runs will be described in section 4.3. Subsequently, we will introduce the analyses and the beam spot position and width during the scan in Section 4.4, 4.5 and 4.6. The evolution of beam spot position as a function of nominal separation is described in section 4.7 and 4.8. Next, we investigate the beam spot's symmetry in section 4.9. Finally, the conclusions drawn from this analysis will be summarized in Section 4.10.

4.2 Beam spot reconstruction

The ATLAS experiment employs various methods to analyze the luminous region and its parameters. The primary method relies on reconstructing and analyzing the distribution of primary vertices (PV) collected across numerous events. A primary vertex is a point within the Large Hadron Collider (LHC) where protons collide and generate new particles. The charged particles, upon moving through a detector,

leave behind trajectories called tracks. These tracks are reconstructed from signals detected by the ATLAS inner detector and used to identify and reconstruct the primary vertices [49].

The beam spot parameters are beam spot position ($posX$, $posY$, $posZ$), the correlation in the x-y plane ($rhoXY$), r.m.s. width of the beam spot distribution (assuming Gaussian shape)(σ_X, σ_Y, σ_Z). Throughout this chapter, we will use the width of the beam spots to refer to this variable and its equal to:

$$\sigma = \sqrt{(\text{emittance} * \beta^*)} \tag{4.1}$$

Where the emittance is a measure of the phase space area occupied by a beam of particles. It characterizes the spread of the particles in both position and momentum space.

β^* is the value of the beta function at the interaction point, which is the location where the beams collide.

These parameters are determined using an unbinned maximum likelihood fit to the spatial distribution of primary vertices. A single primary vertex is selected per event based on the highest value of Σp_T^2, where the sum is taken over all charged tracks included in the vertex fit.

The following criteria are applied for primary vertex selection:

- At least 5 tracks must be associated with the vertex.
- The probability of the vertex fit ($\chi^2, NDoF$) must be greater than 0.1%.

LB refers to a fixed time window, typically lasting 60 seconds. During this period, it is assumed that both the instantaneous luminosity and the data collection configuration remain constant.[29].

The fit takes into account the vertex resolution during the determination of important parameters like the position of the spot and the orientation in x-z and y-z planes as well as the resolution-corrected size of the luminous beam.

For a given primary vertex (PV)with (x_i, y_i, z_i), the beam spot position in the transverse plane is:

$$\vec{B_i} = \begin{pmatrix} posX + tiltX \cdot (posZ - z_i) \\ posY + tiltY \cdot (posZ - z_i) \end{pmatrix} \tag{4.2}$$

For a given sample of N events the likelihood is $\mathcal{L} = \prod_{i=1}^{N} f_i$,

where Probability density function f_i assumes a Gaussian shape of beam spot:

$$f_i = \frac{1}{2\pi\sqrt{|V_i|}} \exp\left(-\frac{1}{2}\left(\vec{B_i} - \vec{P_i}\right)^T\right) V_i^{-1} \left(\vec{B_i} - \vec{P_i}\right) \times \frac{1}{2\pi\,\sigma_Z} \exp\left(-\frac{(\mathrm{posZ} - z_i)^2}{2\,(\sigma_Z)^2}\right) \tag{4.3}$$

with $\vec{P_i} = (x_i, y_i)$ and with V_i being the covariance matrix which includes the uncertainties of beam spot and PV

$$V_i = V_B + \mathrm{k} \cdot V_i^{PV} \tag{4.4}$$

The scale factor k adjusts the uncertainty level in a combined covariance matrix V_i based on the difference between the expected and actual precision of PV reconstruction, and V_B is the covariance matrix of the beam spot in the x-y plane:

$$V_B = \begin{pmatrix} {\sigma_X}^2 & rhoXY \cdot \sigma_X \cdot \sigma_Y \\ rhoXY \cdot \sigma_X \cdot \sigma_Y & {\sigma_Y}^2 \end{pmatrix} \tag{4.5}$$

The beam spot calculation typically occurs offline within the calibration loop. This calculation uses a dedicated data stream called the calibration beam spot, and the final results are uploaded to the ATLAS COOL (Conditions Online Offline Library) database. COOL refers specifically to the ATLAS Conditions Database. It is a specialized system for storing and managing conditions data, which is information that affects the detector's performance but not the particle collisions themselves for more details on beam spot reconstruction, see[50].

4.3 Used dataset

In the following, four different LHC fills, recorded by the ATLAS experiment are analysed. The ATLAS runs differ by parameters, such as the average number of simultaneous interactions μ, the crossing angle of the beams at the interaction point or β^* value. The latter describes the size of the focused proton beams at the interaction point.

The analysis presented in this work is based on data collected from runs collected in 2022. A scan is a specialized type of run where researchers deliberately manipulate certain parameters of the LHC beams to obtain specific information about the detector's response or the beam itself. There are different types of scans performed with the ATLAS detector, each serving a specific purpose.

4.3.1 vdM scan

The purpose of this scan is to measure the luminosity of the particle beams colliding

How the LHC performs a vdM scan:

The luminosity of the Large Hadron Collider (LHC) is measured using a technique known as a luminosity scan. During a scan, the two beams of particles are brought into collision at a specific interaction point. The luminosity monitor systems are activated to record the collision rate. The separation between the two beams is then systematically increased or decreased in a controlled manner by adjusting the magnetic fields of the focusing elements in the accelerator. At each separation value, the collision rate is measured. This process is typically performed in both the horizontal and vertical directions. The recorded collision rates are analyzed to determine the luminosity as a function of the beam separation. A theoretical model, based on the Gaussian beam profile assumption, is fitted to the data. The parameters of the model, such as the beam sizes and the luminosity, are extracted. The luminosity at zero beam separation corresponds to the peak luminosity of the collision. The accuracy of the luminosity measurement depends on the precision of

the beam profile measurements and the fitting procedure.

4.3.1.1 Run 439428

In a van-der-Meer (vdM) run, the luminosity of the particle beam collision is conducted before and after the physics run. The average value μ for this run is 0.85. The luminosity is then measured as a function of the beam separation. The resulting curve can be used to extract the beam size and the luminosity calibration factor[29].

Run 439428 was a long run that lasted for more than 2500 luminosity blocks (1 day, 2 hours, and 18 minutes). The luminosity profile for this run is shown in Figure 4.1. It has scans in both vertical direction (Y scan) and horizontal directions(X scan). There is no crossing angle in this run and β^* is equal to 19.2 m. The half-crossing angle and the β^* are displayed in Figure 4.2. The nominal separation between beams during the run is shown in Figure 4.3 for vertical and horizontal directions at the same time. Eight of twelve scans are on-axis scans and 4 off-axis scans, where the on-axis denotes the particle beams colliding head-on in the non-scanning plane and the off-axis is the scans where the beams are intentionally separated by a fixed amount in the non-scanning plane.

4.3.2 LHCf emittance scan

Emittance scans are a newer technique introduced in 2018, which are essentially mini-vdM scans conducted under normal physics conditions. They aim to measure luminosity by estimating the average number of interactions at different beam separations, similar to vdM scans but with a focus on operational efficiency and stability during regular physics runs. In an emittance scan, beams are separated and scanned through each other similarly to a vdM scan to measure the emittance of the particle beams conducted periodically throughout the experimental program to monitor the beam quality.

How LHCf scans are performed:

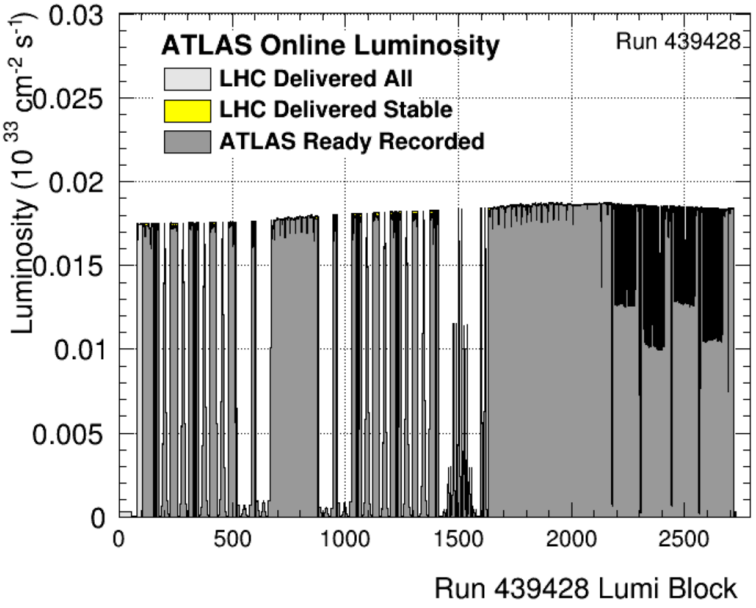

Figure 4.1: Luminosity profile for run 439428 [51]

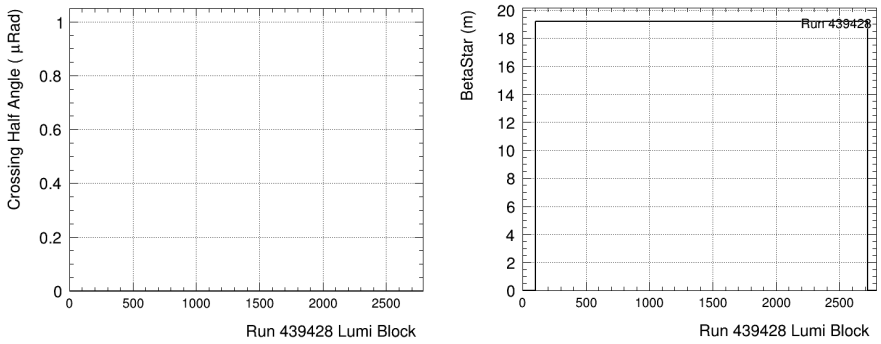

Figure 4.2: Half-crossing angle and β^* values as a function of LB for run 439428. During the run, the crossing angle was zero and the β^* value was 19.2m [51].

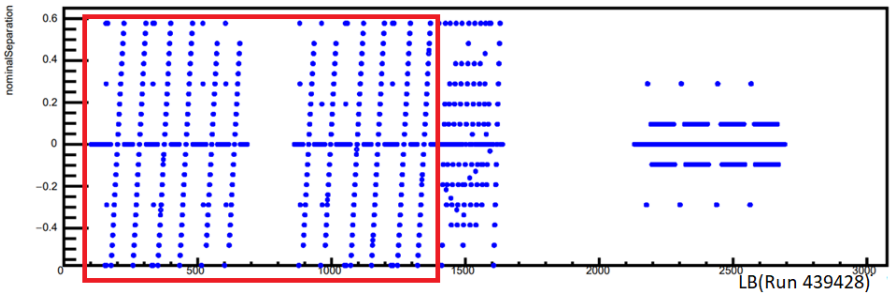

Figure 4.3: The 12 one-dimensional scans were changing nominal separation as a function of LB in Run 439428 inside the red square.

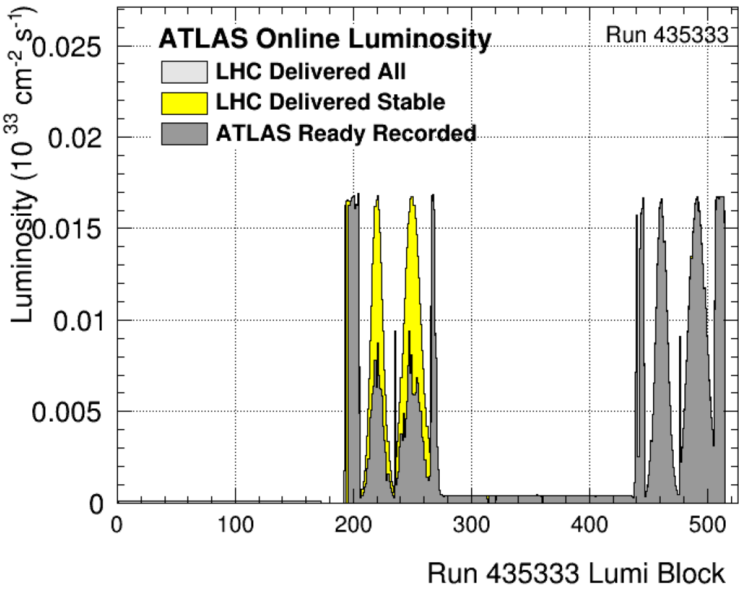

Figure 4.4: Luminosity profile for run 435333 [51]

The LHC is operated in a special configuration for LHCf scans, with the beams colliding at a very small angle. This creates a region of overlap between the two beams, where the forward hadrons are produced.

As the LHC beams collide, the LHCf detector records the energy and momentum of the produced forward hadrons. This data is then analyzed to study the properties of these particles. LHCf scans involve varying the collision energy and the angle between the two beams. This allows researchers to study how the properties of forward hadrons depend on these parameters. [29].

4.3.2.1 Run 435333

This is a short run which lasts only for 300 luminosity blocks (6 hrs, 58 min). The luminosity profile for this run is shown in Figure 4.4. The half-crossing angle and β^* are shown in Figure 4.5. The nominal separation between beams during the run is shown in Figure 4.6 for both vertical and horizontal directions. The first scan is the Y-axis direction and the second is the X-axis direction.

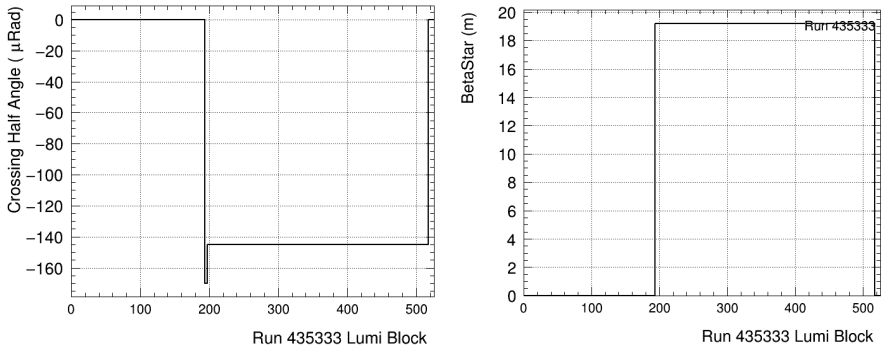

Figure 4.5: Half-crossing angle and β^* values as function of LB for run 435333 [51]

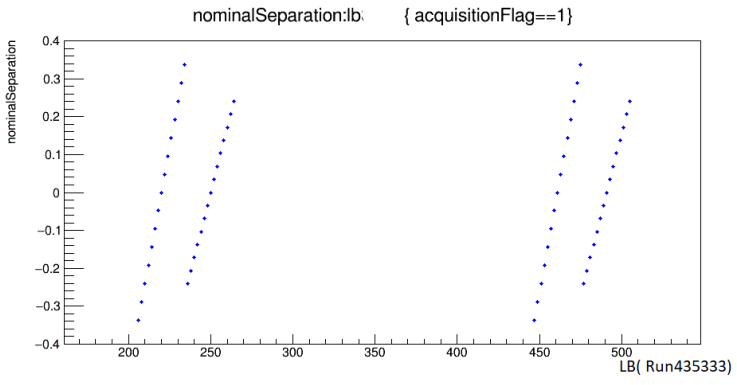

Figure 4.6: The two pairs scan for Run435333

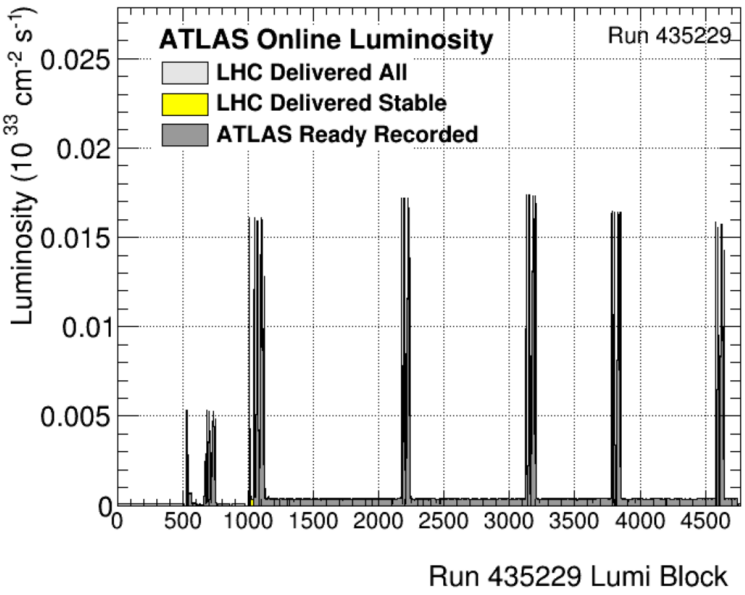

Figure 4.7: Luminosity profile for run 435229 [51]

4.3.2.2 Run 435229

This is the longest run recorded by ATLAS and delivered by the LHC so far, lasting for 4500 luminosity blocks (2 days, 20 hours, and 55 minutes). Figure 4.7 illustrates the luminosity profile for this run. The nominal separation between beams during the run is shown in Figure 4.9 depicting seven scans. The first two pairs are unusable for this analysis because the distribution of events is random and different from the rest of the scans and therefore cannot be compared or used in this study, narrowing our analysis to the remaining five scans. The half-crossing angle and β^* are displayed in Figure 4.8.

4.3.3 Physics run

The value of μ in this run (29.9) is 77 times larger than the previous runs (0.319), and the number of bunches is nearly twice as many, with 302 bunches for this run compared to 144 for previous runs. This run was part of the ramp-up of the LHC each year where they go from a low number of bunches to the full machine in several steps.

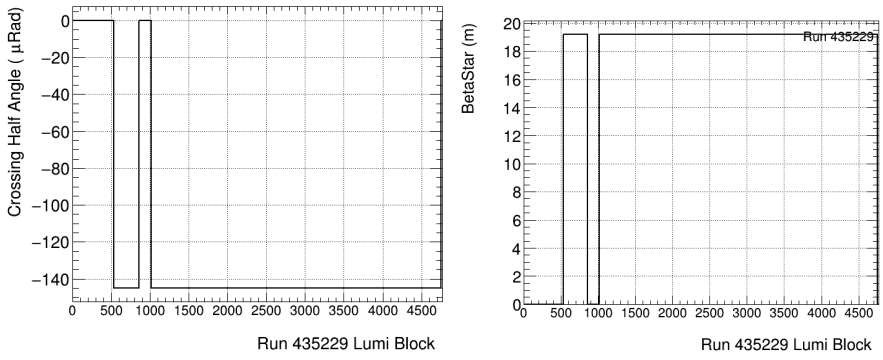

Figure 4.8: Half-crossing angle and β^* values as function of LB for run 435229 [51]

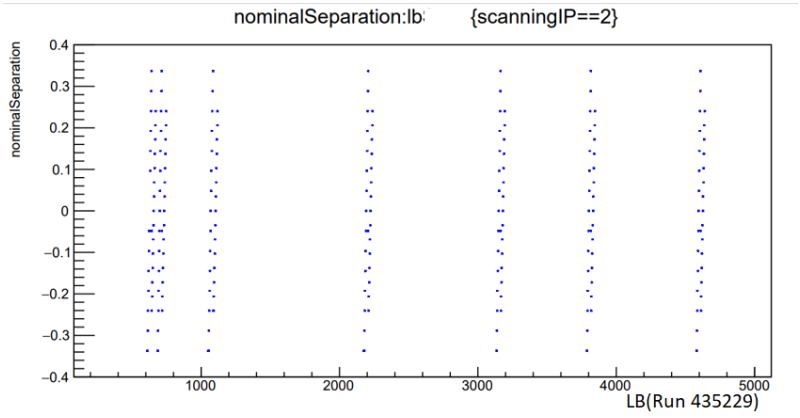

Figure 4.9: The nominal separation between beams as a function of LB during run 435229, the vertical and horizontal direction together

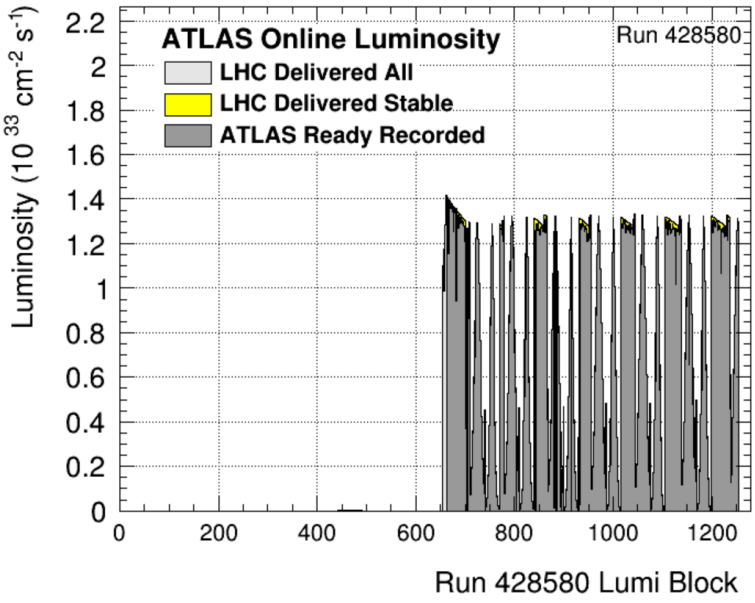

Figure 4.10: Luminosity profile for run 428580 [52]

4.3.3.1 Run 428580

This run lasted for 600 luminosity blocks (15 hours and 12 minutes), with a half crossing angle of -160μRad. The luminosity profile for this run is shown in Figure 4.10. The nominal separation between beams during the run is shown in Figure 4.12 demonstrating the presence of six scans within this run. The half-crossing angle and β^* are illustrated in Figure 4.11.

Table 4.1 shows a comparison of the main parameters for all runs of the current study.

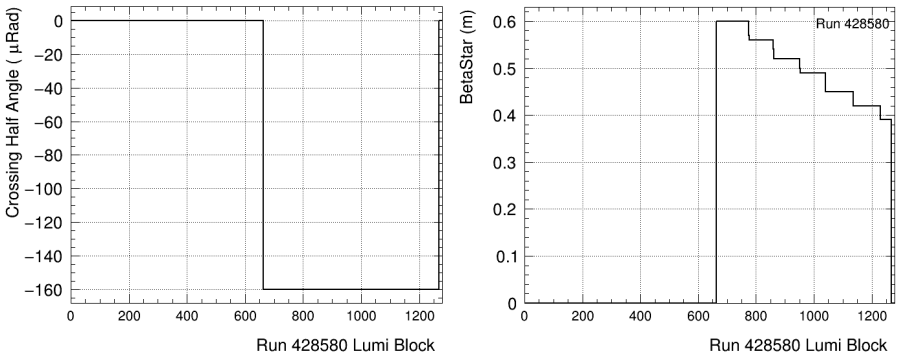

Figure 4.11: Half-crossing angle and β^* values as function of LB for run 428580 [52]

	Run 439428	Run 435333	Run 435229	Run 428580
Beam Energy GeV	6800	6800	6800	6800
Bunches colliding	144	144	144	302
Peak$< Events >$/BX	0.928	0.837	0.859	33.3
Avg$< Events >$/BX	0.852	0.651	0.319	29.9
Beta*	19.2 m	19.2 m	19.2 m	60 cm − 39 cm

Table 4.1: Comparison of the important beam parameters of the four runs investigated

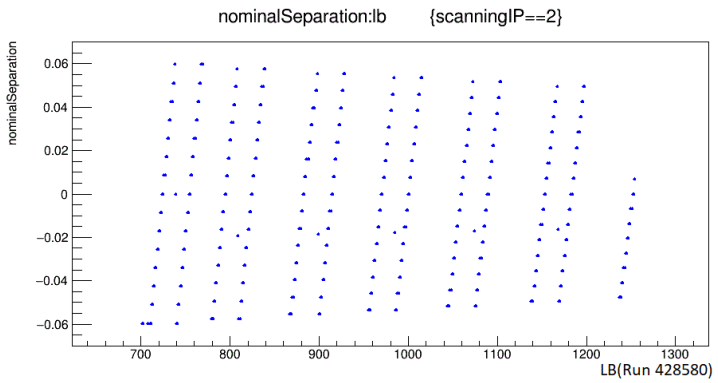

Figure 4.12: Nominal separation for six pairs of scans in Run 428580, as a function of LB

4.4 Study of beam spot position during scan

We will study the position and width of the beam spot concerning the parameters of the scans. The beam spot has been reconstructed as discussed in Section **??**, for every LB and every bunch crossing identifier separately. In this section, we will show the beam spot position for different BCIDs(bunch crossing identifier (number)) discuss the behaviour of the beam spot position during scans, and then discuss the behaviour of the beam spot width during scans.

4.4.1 Beam spot position for different BCIDs

In this section, we will study the position values (X, Y, and Z) for different BCIDs. Figure 4.13 shows the first scan (on-axis) as an example and Figure 4.14 shows the fifth scan (off-axis). For all investigated runs beam spot position is very similar between the different scans, and variations occur mainly in the lower statistics regions at large beam separations.

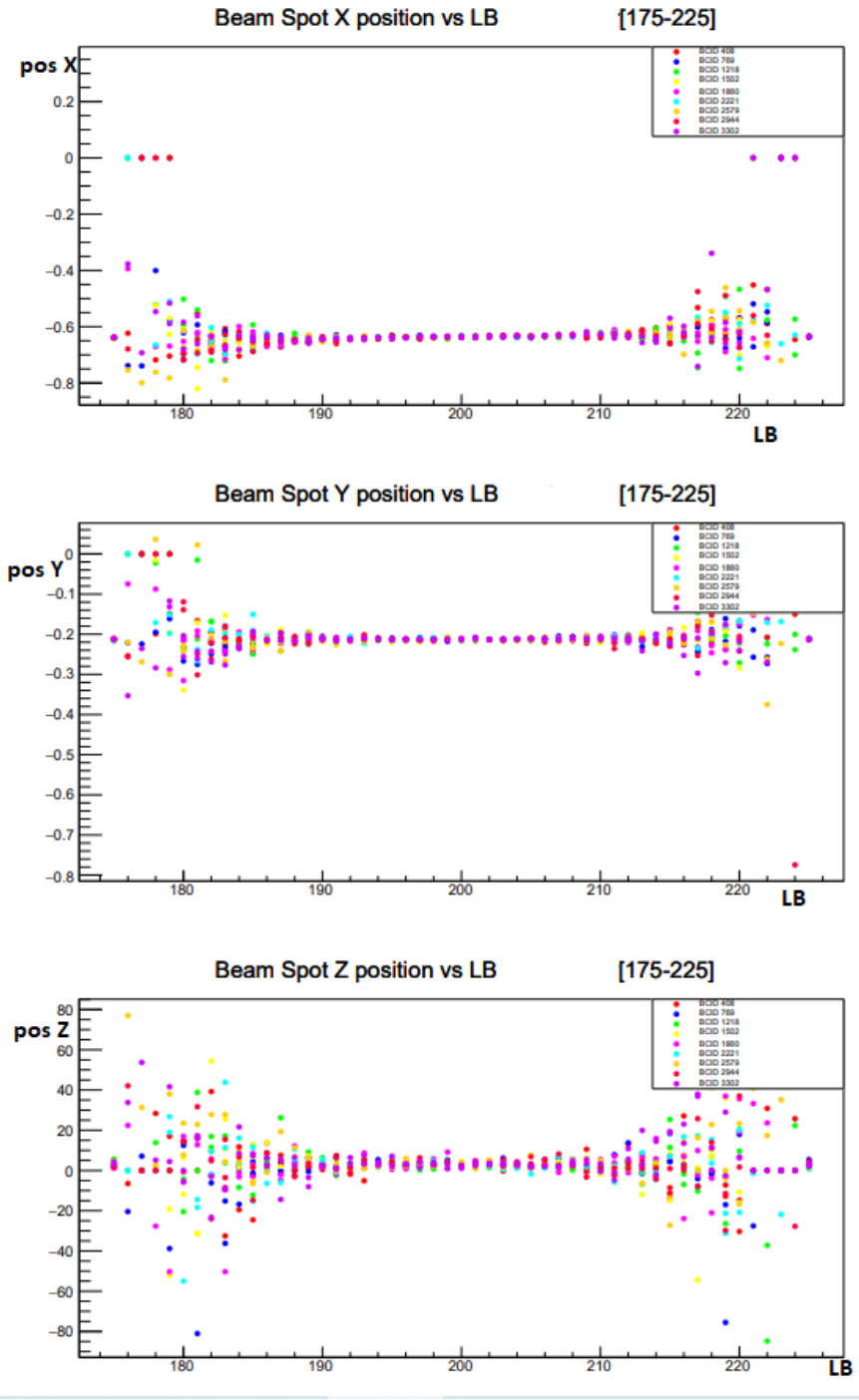

Figure 4.13: The beam position (mm) as a function of LB for different BCIDs value for the first on-axis scan for run 439428. The y-axis represents the position in millimetres.

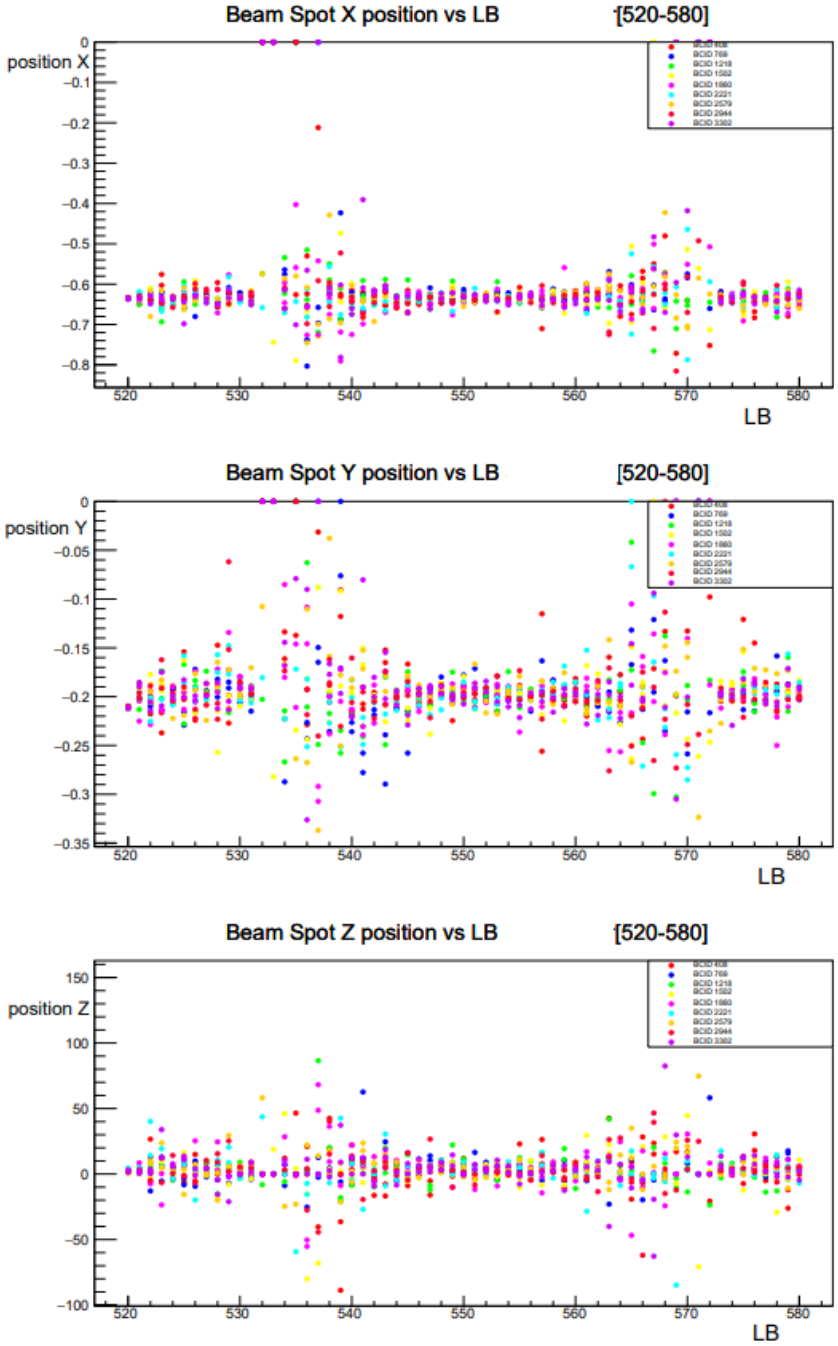

Figure 4.14: The beam position (mm) as a function of LB for different BCIDs value for the fifth off-axis scan for run 439428. The y-axis represents the position in millimeters.

4.5 Evolution of beam position and RMS width as a function of luminosity block

The movement or stability of the beam spot position during scans is studied in the following by averaging over the different BCIDs, defining the mean position as follows:

$$Mean(posX, Y, Z) = \sum_{BCID} \frac{posX, Y, Z}{n} \tag{4.6}$$

where n is the number of averaged BCIDs. The associated uncertainty is given by:

$$Uncertainty = \sqrt{rms^2 + \sigma^2} \tag{4.7}$$

Where rms of the position is the root square of the variance of the beam spot measurement for a given LB over several BCIDs.

$$rms = \sqrt{\left(\sum pos^2/n\right) - \left(Mean^2\right)}$$

And $\underline{\sigma}$ is the measurement uncertainty averaged over the BCIDs.

$$\sigma = \sqrt{\sum posError^2/n}$$

The evolution of the position in the X, Y, and Z-directions for the four runs as a function of LB can be seen in Figures 4.15-4.17 For each run, only example scans are displayed. For additional results from all scans in runs 439428, 435333, 35229, and 428580, please refer to Appendix A,B,C, and D, respectively.

Position X in Figure 4.15 (a) displays a slight increase in scan X similar to Figures 4.15 (b) and (c); note that vdM run starts with X-scan and the rest start with y-scan. Scans in the direction of Y for all runs are stable except for the physics run in plot 4.15(d) showing the reverse trend through an unexpected increase in scan Y. More studies are needed on this point to understand the observation and possible interpretation better.

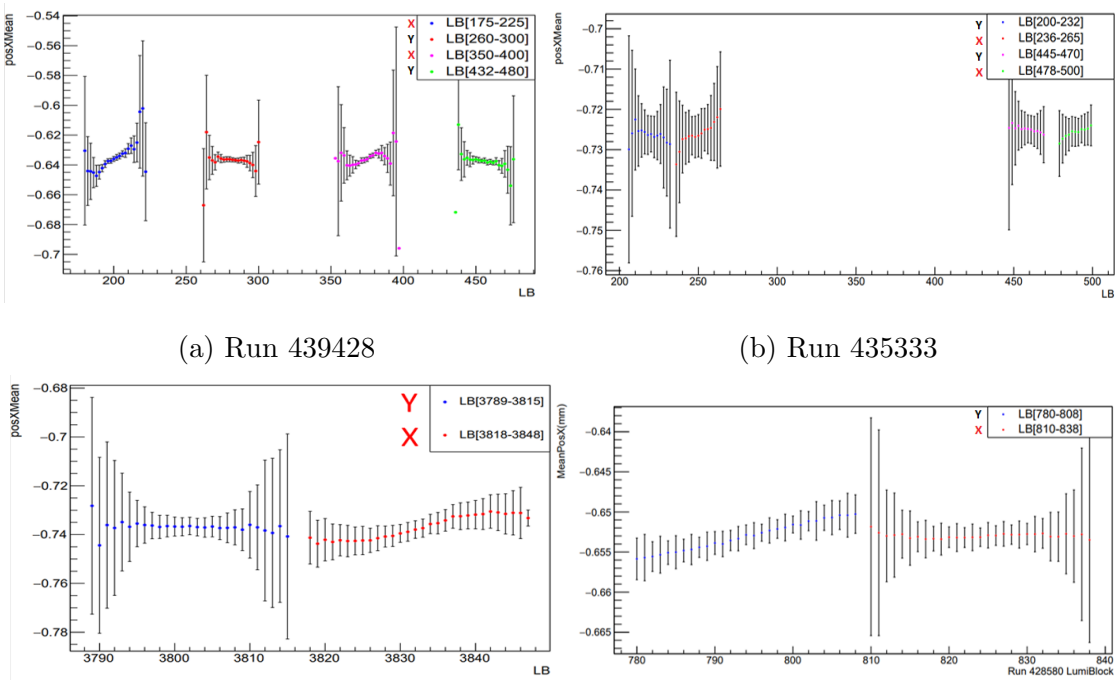

(a) Run 439428

(b) Run 435333

(c) Run4 435229

(d) Run 428580

Figure 4.15: Mean position X (mm)vs LB, for the four investigated runs. In (a), X-scans are always recorded first, then Y-scans. In (b)-(d), it is reversed, and Y-scans are recorded before X-scans. The letters X and Y in the legend indicate the type of the scan X for X-scan and Y for Y-scan.

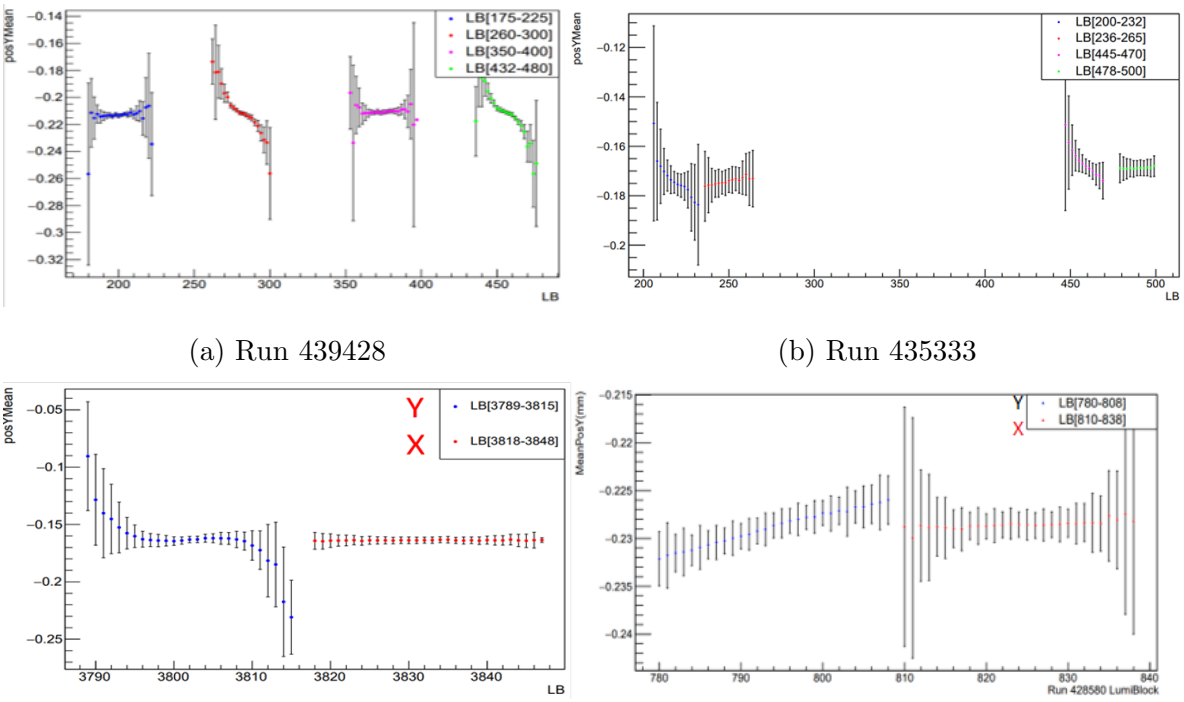

(a) Run 439428

(b) Run 435333

(c) Run 435229

(d) Run 428580

Figure 4.16: Mean position Y (mm) vs Luminosity Block

Position Y in Figure 4.16(a),(b),(c) and(d) have a movement in the Y direction No impact is observed from X scans on the position Y, partially non-linear behaviour and a slight upwards slope during the physics run are observed for Y scans. The non-linear behaviour for large separations in vdM scans has been observed before - [48].

Position Z in Figure 4.17 (a) has a steady pattern and 4.17 (b), (c) and (d) show a similar decreasing shape for scans in Y affected by the crossing angle in the Y direction. If the beams have a crossing angle during scans, the mean of the position in the Z-direction moves over a distance of 30-50 μm during the LHCf runs and over nearly 150 μm during the physics run. The larger movement during the physics run is likely the result of the stronger focusing, i.e. the smaller value of β^*.

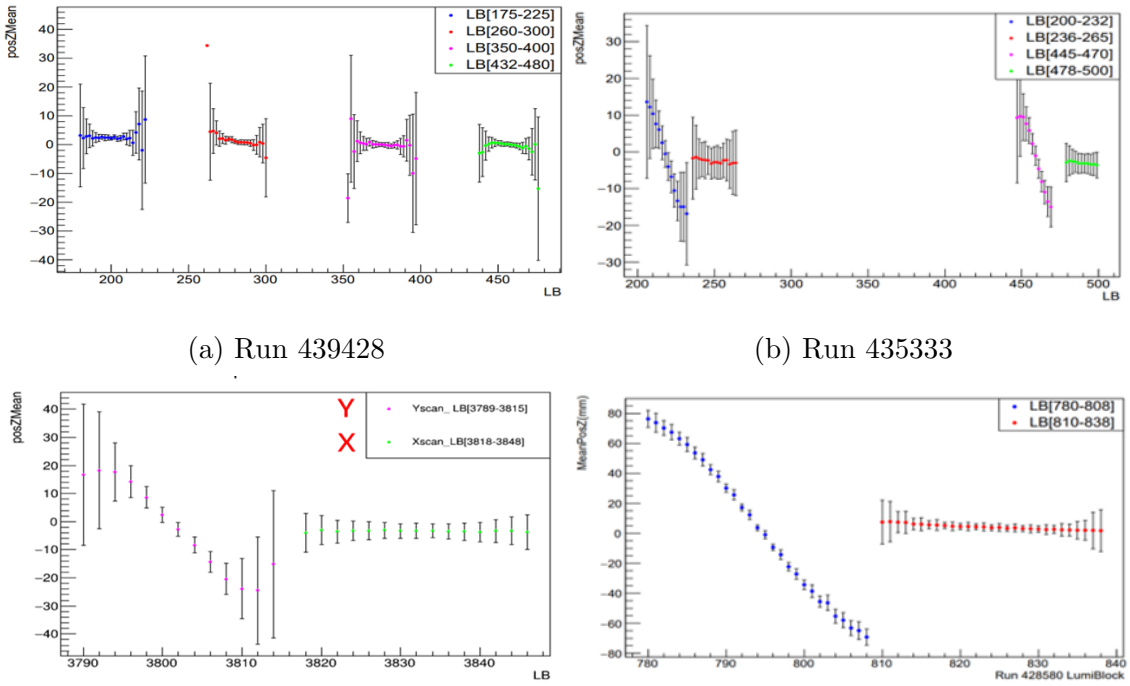

(a) Run 439428

(b) Run 435333

(c) Run 435229

(d) Run 428580

Figure 4.17: Mean position Z (mm)vs Luminosity Block

4.6 Behavior of beam spot width during scans

The behaviour of beam spot width during scans is studied in the following by averaging over the different BCIDs. The width (sigma) of the beam spot during scans is studied in the following by averaging over the different BCIDs, in the same way as calculating the mean of the position:

$$Mean(sigmaX, Y, Z) = \sum_{BCID} \frac{sigmaX, Y, Z}{n} \tag{4.8}$$

The associated uncertainty is determined with the same equation as the position uncertainty. The mean width X, Y and Z plotted against the Lumi Block (LB) can be seen in Figure 4.18 to 4.20 for each run: 439428 (a), 435333 (b), 435229 (c), and 428580 (d). Only example scans are displayed. The remaining ones can be found in the appendix A,B,C, and D, respectively.

For width X in 4.18 the data consistently reveal that the transverse beam spot broadens as the beam separation increases across all runs.

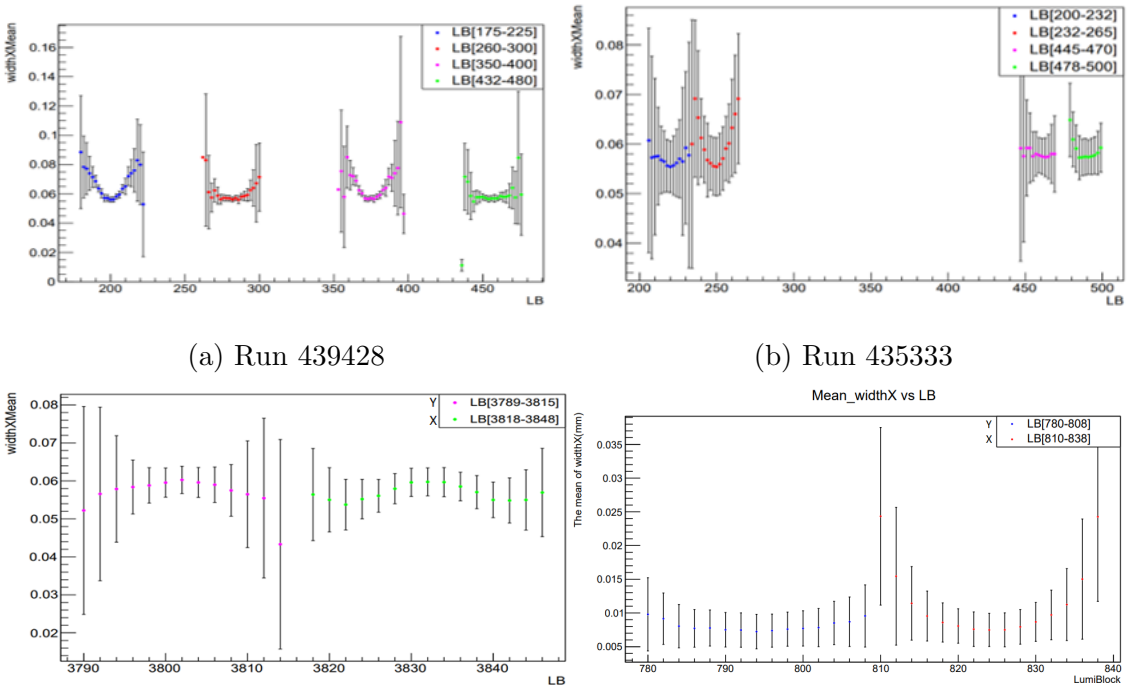

(a) Run 439428

(b) Run 435333

(c) Run 435229

(d) Run 428580

Figure 4.18: Mean width X(mm) vs LB, for the four investigated runs. In (a) X-scans are always recorded first, then Y-scan. In (b)-(d), it is reversed, and Y-scans are recorded before X-scans

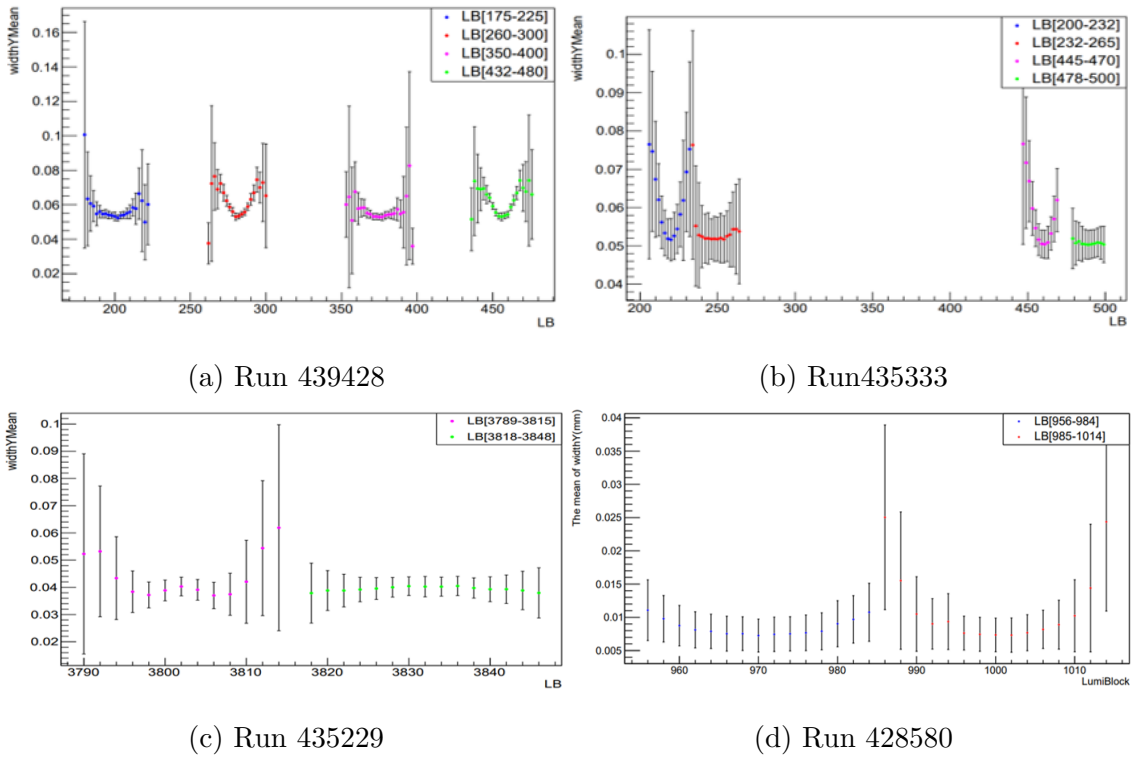

(a) Run 439428

(b) Run435333

(c) Run 435229

(d) Run 428580

Figure 4.19: Mean width Y (mm) vs LB, In (a) X-scans are always recorded first, then Y-scan. In (b)-(d), it is reversed, and Y-scans are recorded before X-scans

For width Y in Figure 4.19 we can see a clear trend of beam broadening with increasing separation between the two beams similar to width X. Width Z in Figure 4.20(a)-(c)shows a small variation of the Z width of the beam spot, i.e. its length during the scan, where larger separations (LBs on the outside of the scan) result in shorter beam spots and central collisions give a slightly longer beam spot. For Figure 4.20 (d), this trend is reversed, i.e. larger separations result in a longer beam spot, and small separations, i.e. more head-on collisions give a shorter beam spot. Interesting is also that the trends are similar for the vdM run without a crossing angle (4.20(a)), and the LHCf runs with a crossing angle (4.20(b)+(c)), while it is different for the physics run which also has a crossing angle (4.20(d)). The presence or absence of a crossing angle can thus not be the driving force for the different patterns, and more studies are needed to pin this down further. Note, that the patterns are similar for other scans in the respective runs. For runs 439428, 435333,

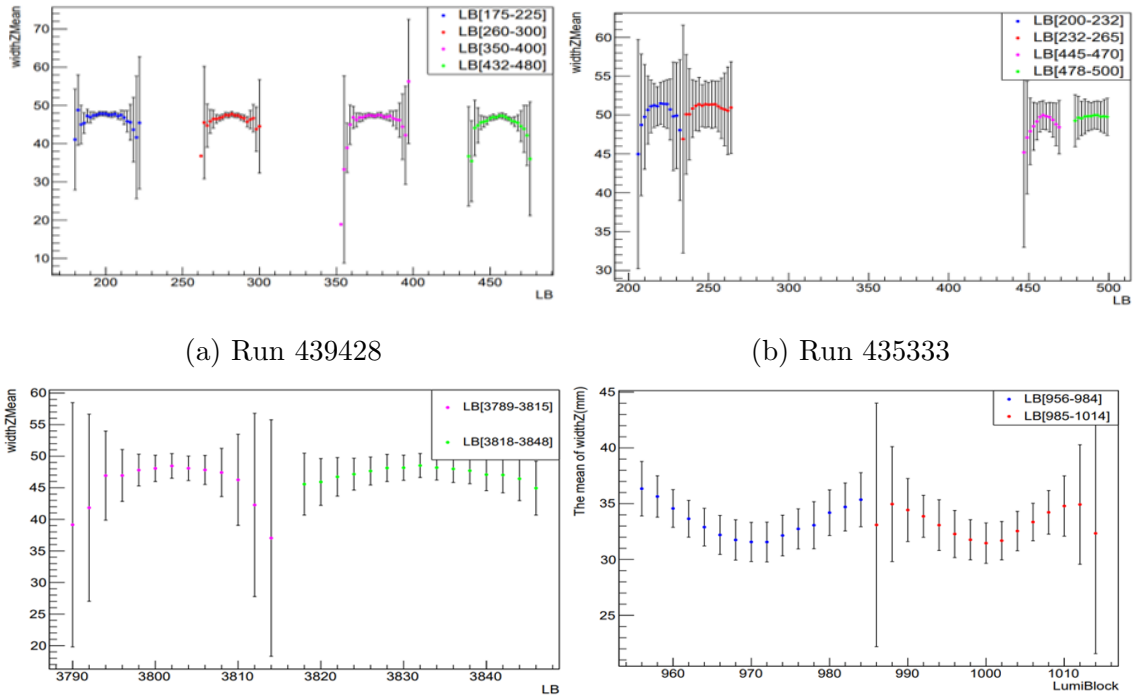

(a) Run 439428

(b) Run 435333

(c) Run 435229

(d) Run 428580

Figure 4.20: Mean width Z(mm) vs Lumi Block, In (a) X-scans are always recorded first, then Y-scan. In (b)-(d), it is reversed, and Y-scans are recorded before X-scans

435229, and 428580, please refer to Appendix A,B,C, and D, respectively.

4.7 Evolution of beam spot position as a function of nominal separation

The evolution of the position in the X, Y, and Z directions for the four runs as a function of nominal separation can be seen in Figures 4.21 to 4.23. For each run, only example scans are displayed. For additional results from all scans in runs 439428, 435333, 35229, and 428580, please refer to Appendix A,B,C, and D. Figure 4.21 presents the position X scan data plotted against the nominal separation(NS). Scans in the direction of X in all subfigures have a slight tilt, while scans in the direction of Y show a steady behaviour except 4.21(d) which shows the reverse

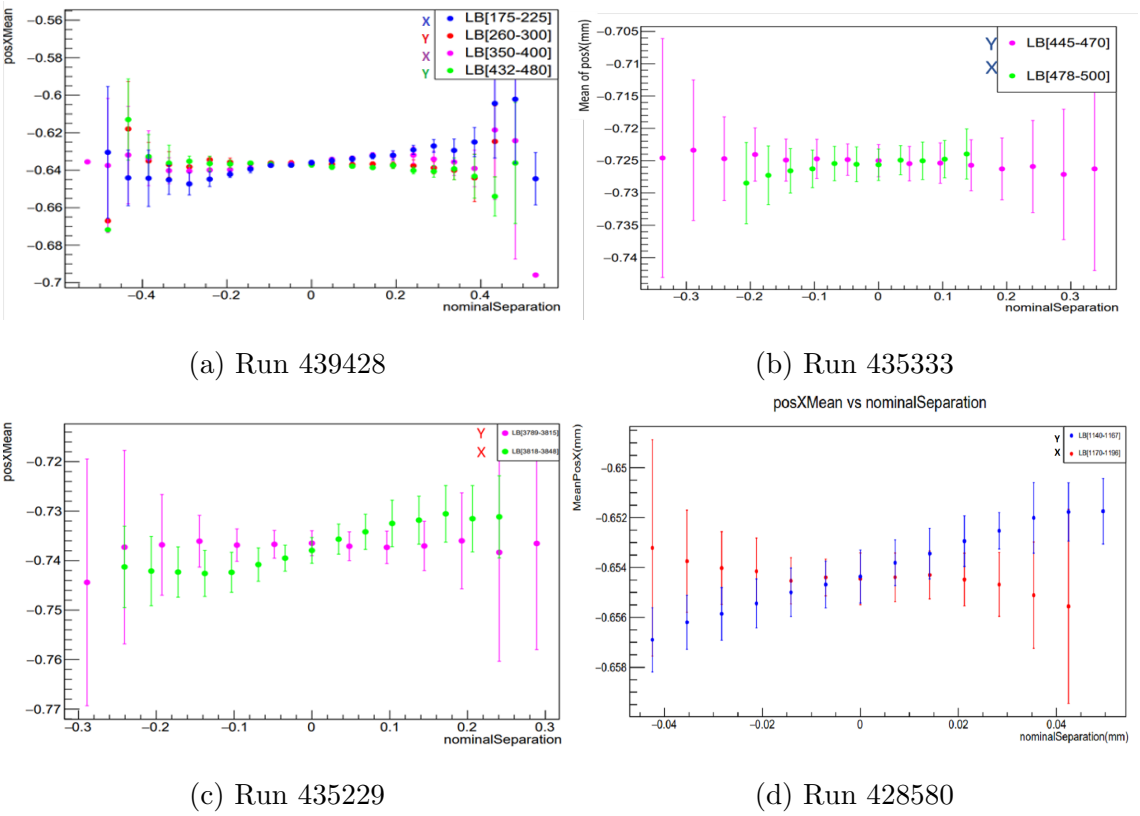

(a) Run 439428

(b) Run 435333

(c) Run 435229

(d) Run 428580

Figure 4.21: Mean position X (mm) vs Nominal Separation (mm), for the four investigated runs. Scans in the X direction are performed before (after) the Y direction for Run 439428 (the other runs). In the LHCf runs ($(b) + (c)$), the separation steps are not necessarily of the same size for the X and Y scans.

trend through an increase in scan Y as observed previously for Figure 4.15. For position, Y in Figure 4.22, scans X in all subfigures show a steady behavior and have slight movement in scans of direction Y which reflect the same pattern seen in Figure4.16.

For position Z in Figure 4.23 scan X is steady in all four runs but, scan Y has a steady pattern in the plot(a) and a decrease in the rest of the subfigure affected by the crossing angle which makes the beam spot move in a large range as seen in the figures.

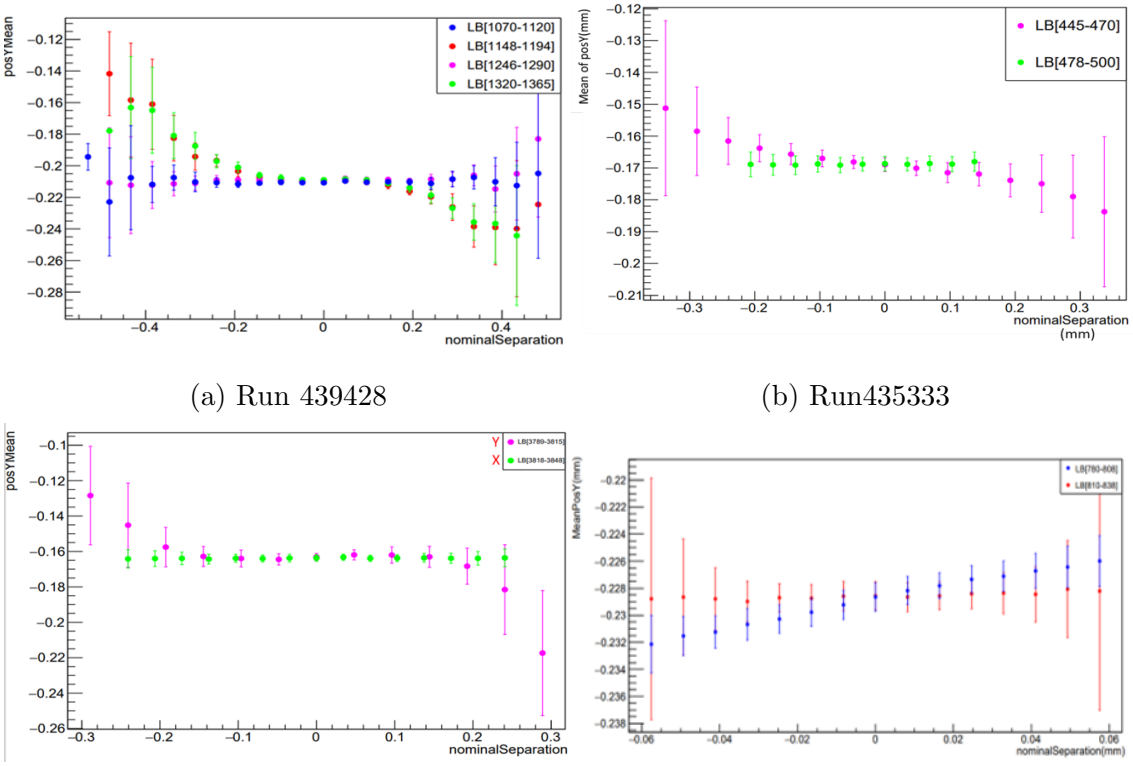

(a) Run 439428

(b) Run435333

(c) Run 435229

(d) Run 428580

Figure 4.22: Mean position Y (mm) vs Nominal Separation (mm), for the four investigated runs. Scans in the X direction are performed before (after) the Y direction for Run 439428 (the other runs). In the LHCf runs ($(b) + (c)$), the separation steps are not necessarily of the same size for the X and Y scans.

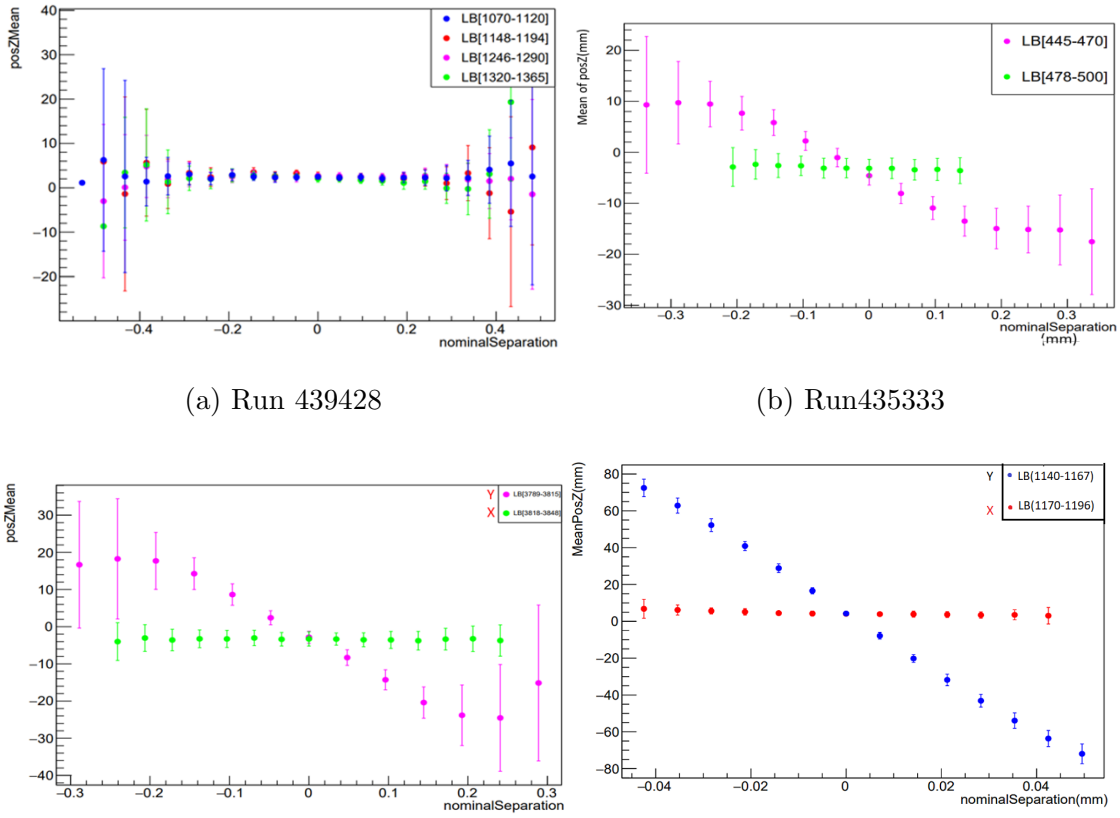

(a) Run 439428 (b) Run435333

(c) Run 435229 (d) Run 428580

Figure 4.23: Mean position Z (mm) vs Nominal Separation (mm), for the four investigated runs. Scans in the X direction are performed before (after) the Y direction for Run 439428 (the other runs). In the LHCf runs ($(b) + (c)$), the separation ranges and step sizes are not of the same size for the X and Y scans.

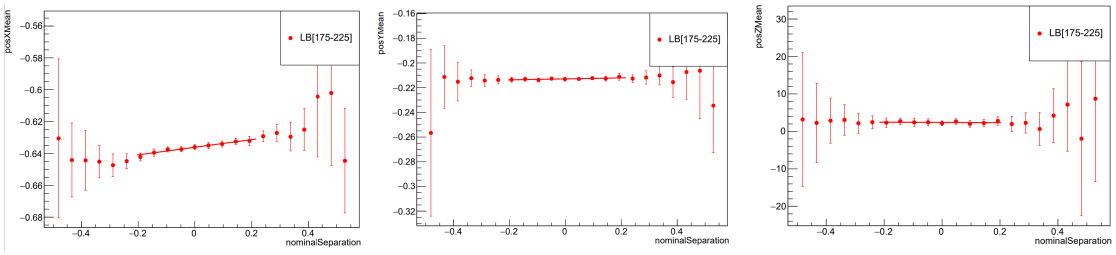

(a) (b) (c)

Figure 4.24: Beam spot positions (mm) in X- (a), Y- (b) and Z-directions (c) as a function of nominal separation (mm) for the first X-scan in run 439428. The data points have been fitted with a polynomial of first order in the range between -0.2 to 0.2mm.

4.8 Quantifying the beam spot position dependence on beam separation

In the following, the beam spot position as a function of nominal separation is fitted with a polynomial of first order, i.e., a linear function. This allows us to quantify the dependence of the beam spot position on the nominal separation.

For the runs,439428, 435333 and 435229 the beam spot position dependence on the nominal separation was fitted in the range of -0.2 to 0.2 mm in the nominal separation with a polynomial of the first order. For the first run, the fits were applied to eight on-axis and four off-axis scans, and for the second to four on-axis scans. For the third run, the fits were applied to 14 on-axis scans. The fitted parameters for the slope and offset were extracted and compared. Example fits can be seen in Figure 4.24. A summary of the slope values of these runs is given in Appendices A and B.

Figure 4.25 displays the fitted slopes for the on-axis scans of Run 439428 for X and Y position (a) and Z position (b), separately. For Figure 4.25 (a), the slope X during the X-scan has a value different from zero, indicating that the position varies with NS. In contrast, slope X during the Y-scan is near zero, suggesting that the

position remains stable as NS changes. Conversely, the Y slope exhibits the opposite pattern: it is close to zero for scan X but significantly non-zero in scan Y. In Figure 4.25 (b), the Z slope agrees with zero within uncertainties for X-scans and twice the uncertainties for Y-scans. So, the beam spot position in the Z-direction can be seen as rather constant for scans without a crossing angle.

For off-axis scans shown in Figure 4.26 (a), the slopes of both beam spot positions X and Y are close to zero, indicating that the positions of X and Y remain relatively unchanged despite changes in nominal separation along for either scan direction. Due to the smaller statistics of off-axis scans, the uncertainties are however also larger. The slope of the beam position movement in the Z-direction in Figure 4.26 (b) is found to be consistent with zero for both X- and Y- scans, given the uncertainties.

Figure 4.27 shows the slopes of the beam spot positions for the first LHCf run 435333. Similar to those from the vdM run, both exhibit near-zero slopes for beam positions during X and Y scans, indicating minimal positional changes in those dimensions except for small non-zero Y-slope during Y-scans, indicating small movements in this direction during Y-scans. As a consequence of the non-zero crossing angle in the LHCf runs, where the crossing plane is in the Y- Z-direction, the Z slope deviates significantly from zero, demonstrating a change of the beam position in the Z-direction during a Y-scan.

Figure 4.28 shows the slopes of the beam spot positions for the second LHCf run 435229. During X-scans, the Y-slope exhibits no change, indicating minimal positional changes in the Y dimension. Conversely, during Y-scans, the X-slope exhibits no change, indicating minimal positional changes in the X dimension. However, a small non-zero Y-slope persists during Y-scans. Additionally, due to the non-zero crossing angle in the LHCf runs, where the crossing plane lies in the Y-Z direction, the Z-slope deviates significantly from zero, demonstrating a change in the beam position along the Z-axis during a Y-scan.

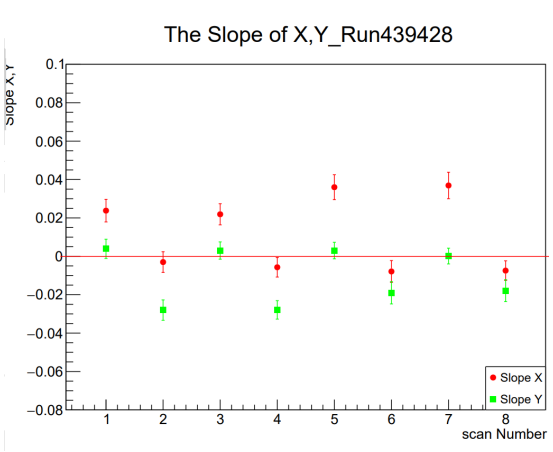

(a)

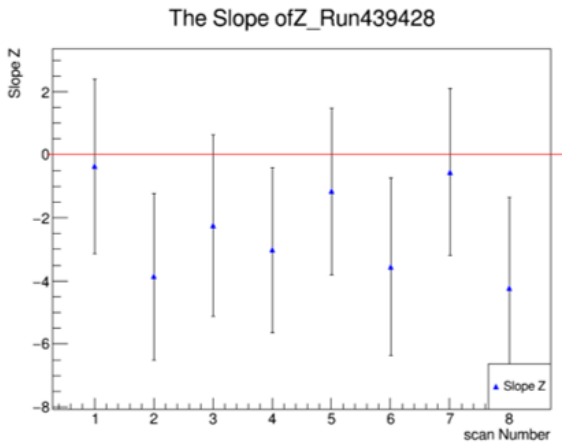

(b)

1 = $LB[175-225]$ x-scan
2 = $LB[260-300]$ y-scan
3 = $LB[350-400]$ x-scan
4 = $LB[432-480]$ y-scan
5 = $LB[1070-1120]$ x-scan
6 = $LB[1148-1194]$ y-scan
7 = $LB[1246-1290]$ x-scan
8 = $LB[1320-1365]$ y-scan

(c) X-axis indication

Figure 4.25: Slopes of the linear fits the beam position in X - and Y-direction (a) and Z-direction (b) as a function of nominal beam separation for on-axis scans in run 439428. The scans are numbered, where the assignment of the numbers to the LB range is indicated in (c). In this run, X-scans are performed always before Y-scans, i.e., odd numbers correspond to X-scans, even numbers to Y-scans. A horizontal line at zero is drawn to guide the eye for easier visual inspection.

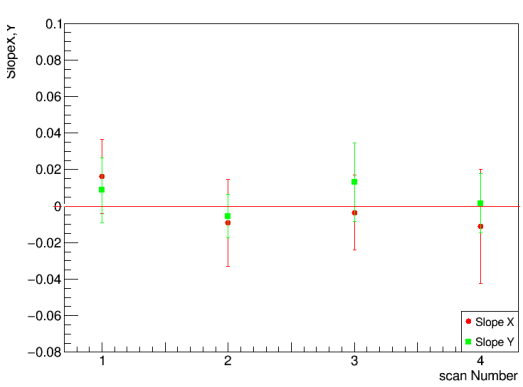

(a)

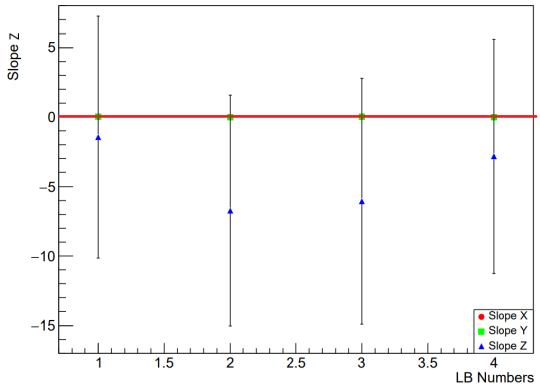

(b)

Numbers on x-axis

1 − LB[532 − 572] y-scan
2 − LB[618 − 654] x-scan
3 − LB[894 − 933] y-scan
4 − LB[980 − 1015] x-scan

(c) X-axis indication

Figure 4.26: Slopes of the linear fits the beam position in X - and Y-direction (a) and Z-direction (b) as a function of nominal beam separation for off-axis scans in run 439428. The scans are numbered, where the assignment of the numbers to the LB range is indicated in (c). In this run, X-scans are performed always before Y-scans, i.e. odd numbers correspond to X-scans, even numbers to Y-scans. A horizontal line at zero is drawn to guide the eye for easier visual inspection.

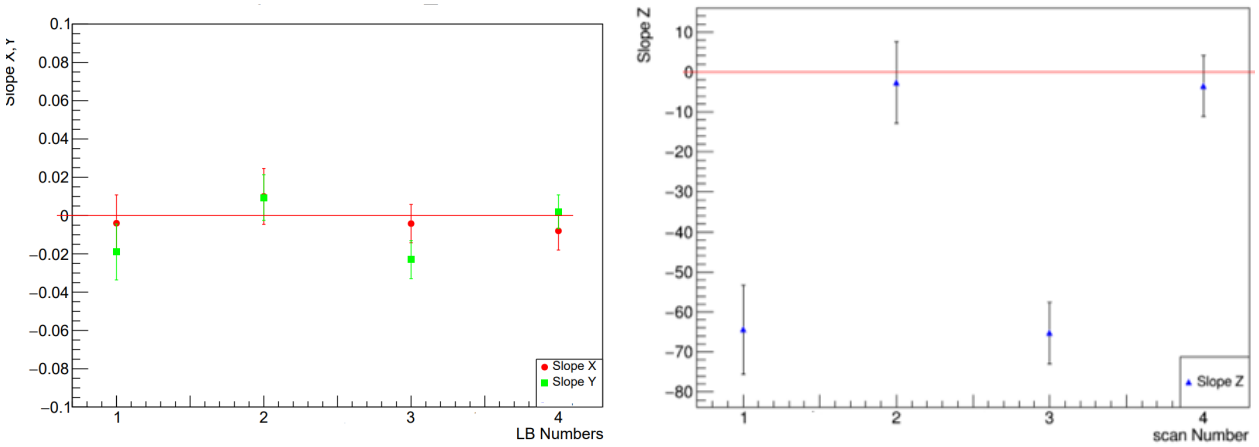

(a) (b)

(c) X-axis indication

Figure 4.27: Slopes of the linear fits the beam position in X - and Y-direction (a) and Z-direction (b) as a function of nominal beam separation in run 435333. The scans are numbered, where the assignment of the numbers to the LB range is indicated in (*c*). In this run, Y-scans are performed always before X-scans, i.e. odd numbers correspond to Y-scans, even numbers to X-scans. A horizontal line at zero is drawn to guide the eye for easier visual inspection.

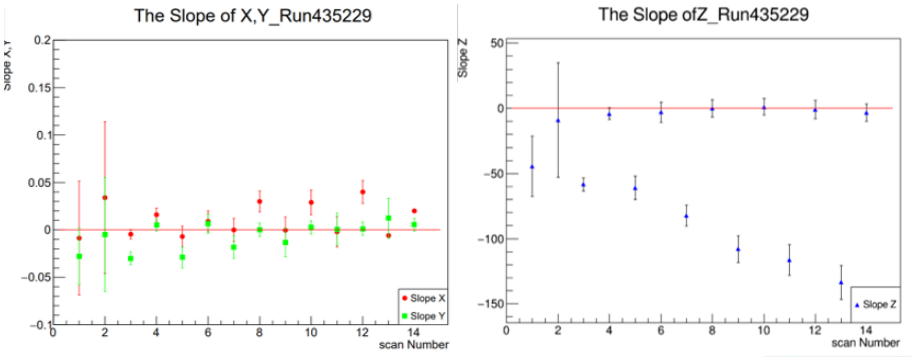

(a) (b)

Scans
1=612-642 (Yscan)
2=643-673 (Xscan)
3=684-716 (Yscan)
4=718-748 (Xscan)
5=1053-1086 (Yscan)
6=1088-1118 (Xscan)
7=2174-2207 (Yscan)
8=2208-2239 (Xscan)
9=3134-3164 (Yscan)
10=3165-3195 (Xscan)
11=3789-3815 (Yscan)
12=3818-3848 (Xscan)
13=4582-4609 (Yscan)
14=4610-4640 (Xscan)

(c) X-axis indication

Figure 4.28: Slopes of the linear fits the beam position in X - and Y-direction (a) and Z-direction (b) as a function of nominal beam separation in run 435229. The scans are numbered, where the assignment of the numbers to the LB range is indicated in (c). In this run, Y-scans are performed always before X-scans, i.e. odd numbers correspond to Y-scans, even numbers to X-scans. A horizontal line at zero is drawn to guide the eye for easier visual inspection.

4.9 Study of the symmetry of the beam spot during the scan

One of the reasons we looked at the beam profiles for the LHCf emittance scans was to see whether the asymmetries we observed in the LHCf scans in [53] had any relation with the beam spot.

The absolute value of nominal separation provides a clear idea of the degree of symmetry of the scans when we monitor the beam spot widths separately for the ascending and descending parts of the scans.

Figures 4.29, 4.30, and 4.31 show the beam spot width in the X, Y, and Z directions, respectively. Example scans from each of the four runs are displayed in each figure, the remaining scans can be found for, runs 439428, 435333, 35229, and 428580, in Appendix A,B,C and D, respectively. Within uncertainty, no difference between ascending and descending parts of the scans in terms of the beam spot widths in either beam spot direction (X, Y, Z) and neither scan direction (X-scan, Y-scan), i.e. no asymmetry is observed.

During the physics run, the beam spot at the collision point was much narrower (around 7-8 micrometres) in both the X and Y directions compared to previous vdM and LHCf runs. In those earlier runs, the beam spot was typically wider, ranging from 50-60 micrometres, with the Y direction being around 40 micrometres specifically for the head-on collisions in the second LHCf run. The reason for this is the significantly smaller β^* value of the physics run ($\beta^* <= 60cm$) compared to the vdM and LHC runs (β^*=19.2m).

4.10 Conclusion

We investigated the behaviour of the beam spot position and size for four runs recorded in 2022 pp collisions: 439428, 435333, 435229, and 428580. Subsequently, we compared the beam spot parameters across these runs.

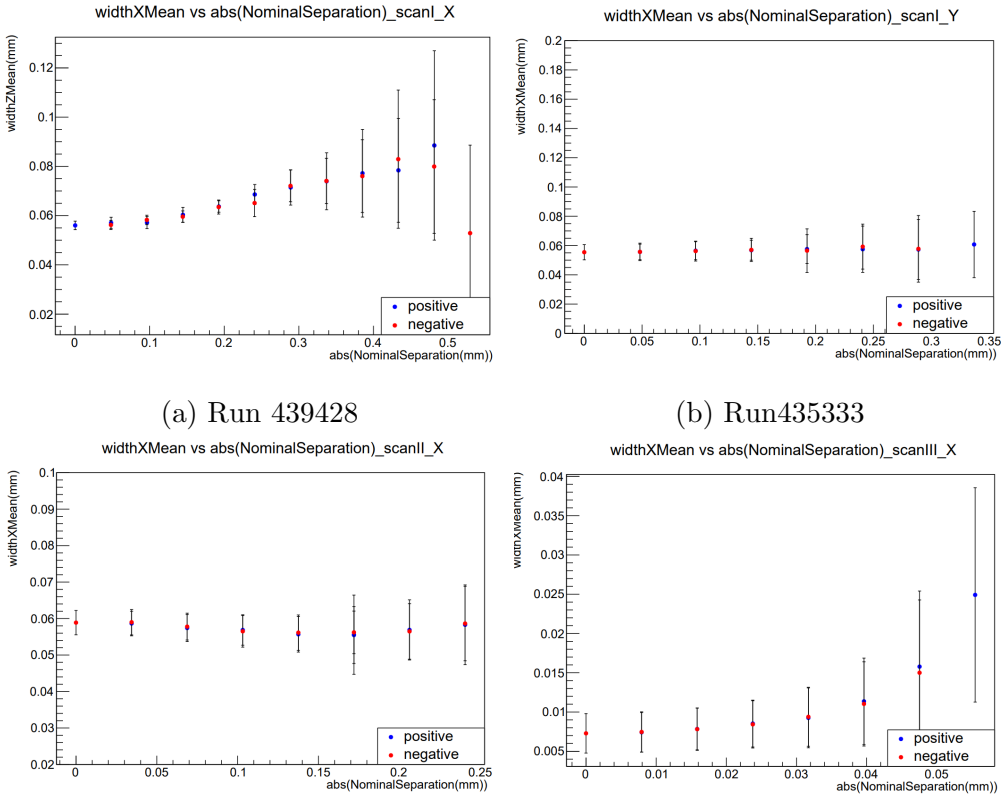

(a) Run 439428

(b) Run435333

(c) Run 435229

(d) Run 428580

Figure 4.29: Mean width X (mm) vs the absolute value of the nominal separation in mm, for the four investigated runs. Example scans are displayed from each of the runs. The full set of scans can be found in the Appendix. The ascending (negative separation)and descending(positive separation) parts of the scans are displayed separately.

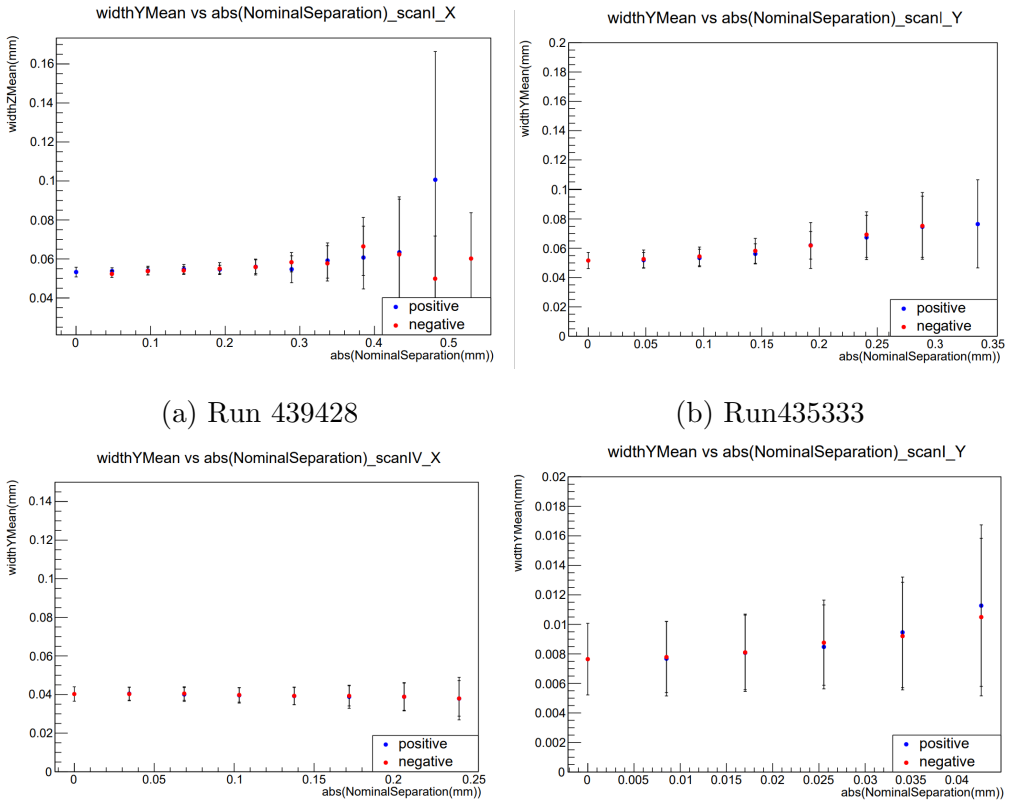

(a) Run 439428

(b) Run435333

(c) Run 435229

(d) Run 428580

Figure 4.30: Mean width Y (mm) vs the absolute value of the nominal separation in mm, for the four investigated runs. Example scans are displayed from each of the runs. The full set of scans can be found in Appendix A,B,C and D. The ascending (negative separation)and descending(positive separation) parts of the scans are displayed separately.

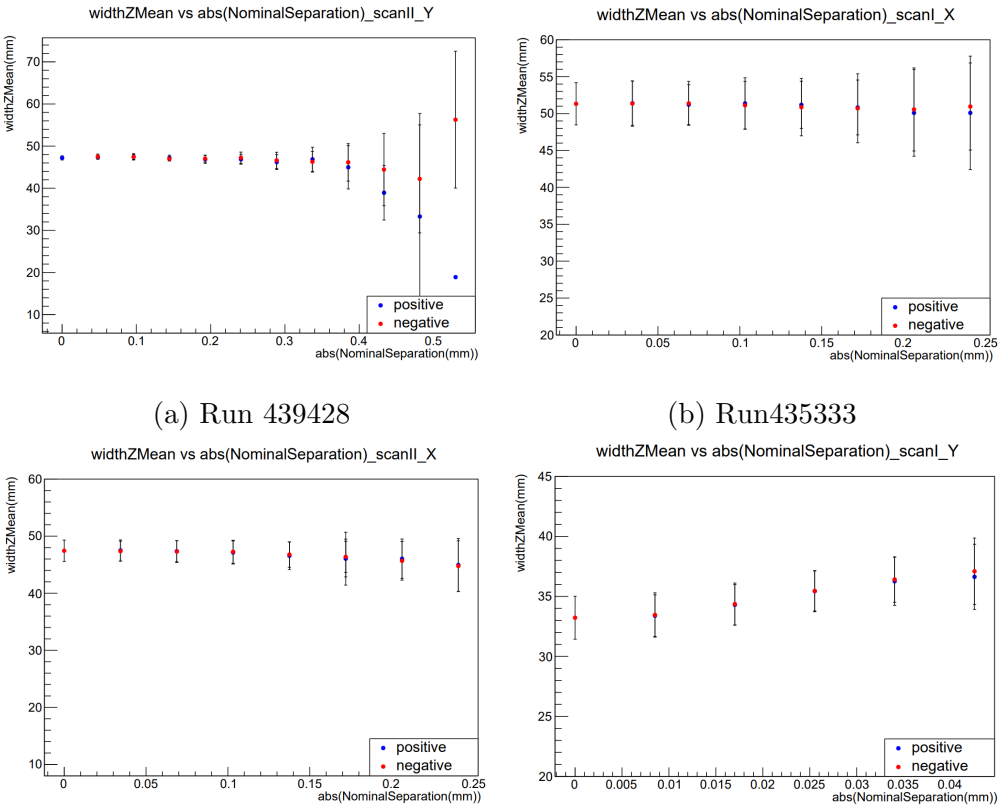

(a) Run 439428

(b) Run435333

(c) Run 435229

(d) Run 428580

Figure 4.31: Mean width Z (mm) vs the absolute value of the nominal separation in mm, for the four investigated runs. Example scans are displayed from each of the runs. The full set of scans can be found in Appendix A,B,C and D. The ascending (negative separation)and descending(positive separation) parts of the scans are displayed separately.

All scans followed the same pattern in both the vdM and LHCf runs, with some differences due to the presence of the crossing angle in the physics and LHCf runs. The physics run exhibited two unexpected features: the movement in the beam spot position X in the Y direction and an increase in the width of position Z in both X and Y directions for larger beam separations.

Scans for runs 439428, 435333 and 435229 were fitted to analyze the relationship between position and nominal separation. These scans revealed the same pattern in the beam spot position movement across the three investigated runs.

Finally, the symmetry of the scans in all runs was tested, and no significant differences were found between the positive and negative parts. The vdM scan analyzed above is to have a reference for a symmetric scan - just in case we would have seen differences. However, in our studies, we could not find any relation to the beam spot, so other explanations have to be followed up. The results of this study provide a valuable foundation for further investigation into the interplay between beam spot and luminosity. A more comprehensive analysis could potentially reveal subtle effects that may impact the accuracy of luminosity measurements, ultimately contributing to a more precise understanding of particle physics phenomena.

Chapter 5

The study of lepton flavour universality using decays $W \to \mu\nu$ and $W \to e\nu$.

5.1 Introduction and Analytical Methods

In Chapters 1 and 2, we explained the importance of lepton flavor universality in studying the Standard Model. In this chapter, we will illustrate the study mechanism, the sample used, and the data selection criteria. After that, we will explain the fit process to calculate the ratio of the number of events of electron and muon with the uncertainty.

In this study, we aim to measure $R(\mu/e)$ and its uncertainty, the ratio of branching fractions of $W \to \mu\nu$ and $W \to e\nu$ defined as:

$$R(\mu/e) = \frac{\mathrm{Br}(W \to \mu\nu)}{\mathrm{Br}(W \to e\nu)}. \tag{5.1}$$

We measure $R(\mu/e)$ using the decays of the top quark to muon and electron through the channels $t \to Wb \to l\nu b$ where $l = \mu, e$. The branching fraction of decay $t \to Wb$ is almost 100 % as mentioned in chapter 2. Therefore, by measuring the ratio of branching fractions of top-quark decay to muon and electron we effectively

extract $R(\mu/e)$.

At the LHC the top quark is dominantly produced in pair with anti-top quark but the decays of the top and anti-top quarks are uncorrelated. In this analysis we select events containing $\mu^+\mu^-$ or e^+e^- pairs produced in the decays of the top and anti-top quarks and extract $R(\mu/e)$ from the ratio of the cross sections of the processes $pp \to t\bar{t}X \to \mu^+\mu^-\nu\bar{\nu}b\bar{b}X$ and $pp \to t\bar{t}X \to e^+e^-\nu\bar{\nu}b\bar{b}X$, where X denotes all unidentified particles accompanying the production of $t\bar{t}$ in pp collisions. More specifically, we use the relation

$$R^2(\mu/e) = \left(\frac{\sigma(pp \to t\bar{t}X \to \mu^+\mu^-\nu\bar{\nu}b\bar{b}X)}{\sigma(pp \to t\bar{t}X \to e^+e^-\nu\bar{\nu}b\bar{b}X)}\right), \tag{5.2}$$

where $\sigma(pp \to t\bar{t}X \to l^+l^-\nu\bar{\nu}b\bar{b}X)$ is the cross section of the corresponding channel.

Technically, we select events with two leptons of opposite charge and two b quarks and measure the ratio

$$R_{ll} = \left(\frac{N^{\mathrm{RD}}(t\bar{t} \to \mu^+\mu^-\nu\bar{\nu}b\bar{b})}{N^{\mathrm{RD}}(t\bar{t} \to e^+e^-\nu\bar{\nu}b\bar{b})}\right) \cdot \left(\frac{N^{\mathrm{MC}}(t\bar{t} \to e^+e^-\nu\bar{\nu}b\bar{b})}{N^{\mathrm{MC}}(t\bar{t} \to \mu^+\mu^-\nu\bar{\nu}b\bar{b})}\right) \cdot \frac{1}{C_{\mathrm{eff}}} \tag{5.3}$$

and obtain $R(\mu/e)$ as

$$R(\mu/e) = \sqrt{R_{ll}}. \tag{5.4}$$

In this expression $N^{\mathrm{RD/MC}}(t\bar{t} \to l^+l^-\nu\bar{\nu}b\bar{b})$ is the number of selected events with two leptons (muons or electrons) in data or Monte Carlo (MC), respectively. In our MC

$$\left(\frac{\sigma(t\bar{t}X \to \mu^+\mu^-b\bar{b}X)}{\sigma(t\bar{t}X \to e^+e^-b\bar{b}X)}\right) = 1$$

The efficiency of the selection of events with two muons or electrons can differ in data and MC. To take into account this difference we include in Eq. 5.3 the correction factor C_{eff}, which is defined as

$$C_{\mathrm{eff}} = \left(\frac{\mathrm{eff}(\mu^+\mu^-)}{\mathrm{eff}(e^+e^-)}\right)^{\mathrm{RD}} \cdot \left(\frac{\mathrm{eff}(e^+e^-)}{\mathrm{eff}(\mu^+\mu^-)}\right)^{\mathrm{MC}}. \tag{5.5}$$

C_{eff} is measured using the decays $Z^0 \to l^+l^-$ $(l = e, \mu)$. It is obtained as

$$C_{\mathrm{eff}} = \left(\frac{N^{\mathrm{RD}}(Z^0 \to \mu^+\mu^-)}{N^{\mathrm{RD}}(Z^0 \to e^+e^-)}\right) \cdot \left(\frac{N^{\mathrm{MC}}(Z^0 \to e^+e^-)}{N^{\mathrm{MC}}(Z^0 \to \mu^+\mu^-)}\right). \tag{5.6}$$

The electrons and muons from the Z^0 decays are selected using the same requirements as in the signal processes with top and anti-top quarks.

5.1.1 A few details regarding the sample used and the source of uncertainty

By using the decays of Z^0 we assume that $\mathrm{Br}(Z^0 \to \mu^+\mu^-) = \mathrm{Br}(Z^0 \to e^+e^-)$. Experimentally, the ratio of these branching fractions is found to be [8]

$$\frac{\mathrm{Br}(Z^0 \to \mu^+\mu^-)}{\mathrm{Br}(Z^0 \to e^+e^-)} = 1.0001 \pm 0.0024. \tag{5.7}$$

Therefore, the uncertainty of 0.0024 contributes to our result.

The efficiency of reconstruction and identification of electrons and muons is sensitive to the presence of additional particles in the events. In the processes with top and anti-top quarks, two leptons are accompanied by two b-jets. To ensure a similar particle environment for the measurement of C_{eff}, we determine this quantity in the processes where Z^0 is produced in association with at least two jets.

To select the events with $t\bar{t}$ production we require the presence of at least two b jets. The efficiency of b tagging is almost independent of the presence of the two isolated leptons in the event. Therefore, R_{ll} is not sensitive to the systematic uncertainties due to b tagging. Any residual contribution of these uncertainties, as well as the uncertainties due to the electron and muon selection, are obtained using the procedures prescribed by the corresponding Combined Performance (CP) groups of ATLAS. CP group is a team of physicists who specialize in developing and maintaining the software tools used to reconstruct, identify, and measure various physics objects, such as electrons, muons, jets, and photons, from the raw detector data.

In addition to $t\bar{t}$, the production of $Wt \to l^+l^-\nu\bar{\nu}b\bar{b}$ also contributes to the selected final state at the level of 3%. In this process, two leptons are produced in the decays of real W bosons. Therefore, this contribution in our analysis is counted as the signal.

The decay $W \to \tau\nu$ also contributes to the sample of selected events, although this contribution is suppressed by the strong cut on the transverse momentum of the leptons. In the Standard Model, the branching fractions of W boson decays

to different leptons are the same as mentioned in Chapter 2. In our analysis, we assume that

$$\mathrm{Br}(W \to \tau\nu) = \frac{1}{2}\left(\mathrm{Br}(W \to \mu\nu) + \mathrm{Br}(W \to e\nu)\right) \tag{5.8}$$

According to the current experimental results given in Eq. 6.1 the $\mathrm{Br}(W \to \mu\nu)$ and $\mathrm{Br}(W \to e\nu)$ agree within 0.6%, and this assumption produces a negligible impact on our result.

This chapter proceeds as follows: Section 5.2 gives details of the ATLAS Run-2 pp collision dataset and Monte Carlo simulated samples used in this analysis. Section 5.3 describes the event selection used in this analysis. Section 5.5 describes a study for background efficiencies and scale factor calculations. Section 5.7 describe all systematic uncertainties included in this analysis. Section 5.6 describes the fit procedure and Section 5.9 illustrates the result of this study.

5.2 Data and Monte Carlo simulated Samples

The analysis is performed on pp collisions at $\sqrt{s} = 13$ TeV using the data collected in 2015-2018. Events fulfil the standard data quality requirements specified in the good run lists (GRL), GRL is a critical tool for sifting through the massive amount of data collected by the detector and identifying the high-quality samples ideal for physics analysis. The corresponding GRL files and integrated luminosity of the selected samples are provided in Table 5.1. Events are selected using TOPQ1 derivation [1] in the main `Physics` stream. This derivation contains all events that have at least one lepton with $p_T > 20$ GeV. All data samples from 2015-2018 were used with an integrated luminosity of $140 fb^{-1}$.

[1] Within the ATLAS experiment, data from collisions undergoes a series of reconstruction steps. These steps are used to identify and measure the particles involved. TOPQ1 refers to a specific derivation format used within the Athena software framework that defines a particular sequence for processing this data.

Year	GRL File	$\int Ldtfb^{-1}$
2015	`data15_13TeV/20170619/physics_25ns_21.0.19.xml`	3.2
2016	`data16_13TeV/20180129/physics_25ns_21.0.19.xml`	33.4
2017	`data17_13TeV/20180619/physics_25ns_Triggerno17e33prim.xml`	44.6
2018	`data18_13TeV/20190318/physics_25ns_Triggerno17e33prim.xml`	58.8
	Total	140.1

Table 5.1: GRLs for each year and their corresponding integrated luminosity used in this analysis.

The main signal (both $t\bar{t}$ and Wt) and background samples were processed through the Full ATLAS detector Simulation(FS) based on GEANT4. FS simulation requires significant computing power and time to generate all particle interactions within the detector, aiming for the most accurate representation of real-world physics processes. Studies on MC generator systematic were done with ATLAS Fast (AF) simulation samples. This simulation provides a faster alternative, sacrificing some detail for speed. It can be useful for studying specific aspects of collisions or analyzing large datasets.

The full list of the datasets used in the analysis is given in Section 5.2.1.

5.2.1 MC samples

Monte Carlo simulation is a numerical method that employs random sampling to solve problems involving probabilistic interactions of particles and their detection. It is used to develop the analysis, to compare to data and to evaluate the signal and background efficiencies. The simulation process steps are detailed in Chapter 3.

The list of MC samples used in this analysis is shown in Tables 5.2 and 5.3. The last column states whether full (FS) or fast (AF) simulation was used.

Table 5.2: Top MC Samples

Sample	Cross-section (pb)	Simulation
$t\bar{t}$ (di-leptons) Powheg + Pythia8	76.95	FS
$t\bar{t}$ (non all-hadronic) Powheg + Pythia8	396.87	FS
$t\bar{t}$ (non all-hadronic) Powheg + Pythia8	396.87	AF
$t\bar{t}$ Powheg + Herwig	320.11, 77.00	AF
$t\bar{t}$ Powheg + Pythia8 hdamp	320.00, 76.94	AF
$t\bar{t}$ (di-leptons) Powheg + Pythia8 pthard =1	76.92	AF
$t\bar{t}$ (di-leptons) top recoil	76.93	AF
$t\bar{t} + W$ aMC@NLO	0.55	FS
$t\bar{t} + Z(\nu\nu)$ aMC@NLO	0.15	FS
$t\bar{t} + Z(q\bar{q})$ aMC@NLO	0.53	FS
$t\bar{t} + l\bar{l}$ aMC@NLO	0.037	FS
Wt inclusive Powheg + Pythia8	37.94, 37.91	FS
Wt di-leptons Powheg + Pythia8	4.00, 3.99	FS
Wt di-leptons Powheg + Pythia8	4.00, 3.99	AF
Wt di-leptons Powheg + Herwig	4.00, 3.99	AF
Wt inclusive Powheg + Pythia8 - DS	36.93, 37.66	FS
Wt di-leptons Powheg + Pythia8 - DS	3.89, 3.97	FS

Table 5.3: Background MC Samples

Sample	Simulation
W + jets Sherpa	FS
l^+l^- + jets Sherpa	FS
l^+l^- + jets (low mass) Sherpa	FS
l^+l^- + jets (Madgraph+Pythia)	FS
$ZZ \to q\bar{q}l\bar{l}$ Sherpa	FS
$WZ \to q\bar{q}l\bar{l}$ Sherpa	FS
$WW \to q\bar{q}l\nu$ Sherpa	FS
$ZW \to q\bar{q}l\nu$ Sherpa	FS
$VV \to 4\ l$ Sherpa	FS
$VV \to 3\ l + \nu$ Sherpa	FS
$VV \to 2\ l + \nu\nu$ Sherpa	FS
Single t, s-channel Powheg + Pythia8	FS
Single t, t-channel Powheg + Pythia8	FS

5.2.2 Signal Simulation Samples

The analysis focused on events where top quark pairs $t\bar{t}$ decay into one or more electrons e or taus τ that ultimately produce electrons through the intermediate production of W bosons. This selection strategy ensured a very clean sample of $t\bar{t}$ decays with minimal background from other processes.

As specified by ATLAS, The description of the Monte Carlo samples below is provided by the Atlas Publication Committee(text provided by ATLAS [54]), to be used in all ATLAS publications [55]. The extract of this description is given below.

5.2.2.1 $t\bar{t}$

The production of $t\bar{t}$ events was modelled using the PowhegBoxv2 [56, 57, 58, 59] generator, which provided matrix elements at the next-to-leading order (NLO) in the strong coupling constant α_s, and the NNPDF3.0nlo [60] parton distribution function (PDF). The h_{damp} parameter, which controls the matching in Powhegb and effectively regulates the high-p_T radiation against which the $t\bar{t}$ system recoils, was set to $1.5m_top$ [61]. The functional form of the renormalisation and factorisation scales was set to the default scale ($\sqrt{m_{top}^2 + {p_T}^2}$). The events were interfaced with PYTHIA8.230 [62] for the parton shower and hadronisation, using the A14 set of tuned parameters [63] and the NNPDF2.3lo set of PDFs [64]. The decays of the bottom and charm hadrons were simulated using the Evtgen1.6.0 program [65].

The $t\bar{t}$ sample was normalised to the cross-section prediction at next-to-next-to-leading order (NNLO) in QCD including the resummation of next-to-next-to-leading logarithmic (NNLL) soft-gluon terms calculated using $TOP_{pp}2.0$ [66, 67, 68, 69, 70, 71, 72]. For proton-proton collisions at a centre-of-mass energy of ($\sqrt{s} = 13TeV$), this cross-section corresponds to $\sigma(t\bar{t})_{\text{NNLO+NNLL}} = 832 \pm 51\text{pb}$ using a top-quark mass of $m_{top} = 172.5GeV$. The uncertainties in the cross-section due to the PDF and α_s were calculated using the PDFforLHC[15] prescription [73] with the $MSTW2008_{nnlo}$ [74, 75], $CT10_{nnlo}$ [76, 77] and $NNPDF2.3_{lo}$ [64] PDF sets in the five-flavour scheme and were added in quadrature to the effect of the scale

uncertainty.

5.2.2.2 W t-channel single top

The associated production of top quarks with W bosons (tW) was modelled by the PowhegBoxv2 [78, 57, 58, 59] generator at NLO in QCD using the five-flavour scheme and the NNPDF3.0nlo set of PDFs [60]. The diagram removal scheme [79] was used to remove interference and overlap with $t\bar{t}$ production. The events were interfaced to PYTHIA8.230[62] using the A14 tune [63] and the NNPDF2.3lo set of PDFs [64].

5.2.2.3 $t\bar{t}V$

The production of $t\bar{t}V$ refers to the creation of a top quark-antiquark pair ($t\bar{t}$) along with a massive vector boson (V), where V can represent a Z boson, a W boson (W^+ or W^-), or even a pair of W bosons (WW) involves the electroweak interaction. This process is less frequent compared to standard $t\bar{t}$ production. The production of $t\bar{t}V$ events was modelled using the MadGaph5_aMC@NLO2.3.3[80] generator at NLO with the NNPDF3.0nlo[60] parton distribution function (PDF). The events were interfaced to PYTHIA8.210 [62] using the A14 tune [63] and the NNPDF2.3lo [60] PDF set. The decays of bottom and charm hadrons were simulated using the EvtGen1.6.0 program [65].

5.2.2.4 $t\bar{t}H$

$t\bar{t}H$ refers to the creation of a top quark-antiquark pair ($t\bar{t}$) alongside a Higgs boson (H).This process is even rarer than $t\bar{t}V$ production. The production of $t\bar{t}H$ events was modelled using the PowhegBoxv2 [56, 57, 58, 59, 81] generator at NLO with the NNPDF3.0nlo [60] PDF set. The events were interfaced to PYTHIA8.230 [62] using the A14 tune [63] and the NNPDF2.3lo [60] PDF set. The decays of bottom and charm hadrons were performed by EvtGen1.6.0[65].

5.2.3 Background Simulation Samples

The background for this analysis comes from two main sources: high-p_T processes producing two prompt leptons and processes that are misidentified as signals. The first mainly comes from Drell-Yann processes and the second from 'fakes'. The description of the Monte Carlo generators is provided by the ATLAS publication committee [55], [54].

5.2.3.1 V+jets

The production of V+jets ($V = Z, W$) was simulated with the SHERPA2.2.1[82] generator using next-to-leading-order (NLO) matrix elements (ME) for up to two partons, and leading-order (LO) matrix elements for up to four partons calculated with the Comix [83] and OPENLOOPS [84, 85, 86] libraries. They were matched with the SHERPA parton shower [87] using the MEPS@NLO prescription [88, 89, 90, 91] using the set of tuned parameters developed by the SHERPA authors. The NNPDF3.0NNLO set of PDFs [60] was used and the samples were normalised to a next-to-next-to-leading-order (NNLO) prediction [92].

5.2.3.2 Dibosons

Samples of diboson final states (VV) were simulated with the SHERPA2.2.1 or 2.2.2 [82] generator depending on the process, including off-shell effects and Higgs boson contributions, where appropriate. Fully leptonic final states and semileptonic final states, where one boson decays leptonically and the other hadronically, were generated using matrix elements at NLO accuracy in QCD for up to one additional Parton and at LO accuracy for up to three additional Parton emissions. Samples for the loop-induced processes $gg \to VV$ were generated using LO-accurate matrix elements for up to one additional parton emission for both the cases of fully leptonic and semileptonic final states. The matrix element calculations were matched and merged with the SHERPA parton shower based on Catani–Seymour dipole factorisation [83, 87] using the MEPS@NLO prescription [88, 89, 90, 91]. The

virtual QCD corrections were provided by the OpenLoops library [84, 85, 86]. The NNPDF3.0nnlo set of PDFs was used [60], along with the a dedicated set of tuned parton-shower parameters developed by the Sherpa authors.

5.2.4 Fakes

5.2.4.1 $t\bar{t}$ and W t-channel single top

The main contribution to the events with at least one fake lepton comes from $t\bar{t}$ or Wt production where only one of the leptons comes from $W \to l\nu$ decay. The simulation of such events is described above. We used in the analysis the non-all-hadronic $t\bar{t}$ and inclusive Wt samples.

5.2.4.2 s and t-channel single top

s- and t-channel single top production can also produce di-lepton events with at least one fake lepton.

Single-top t-channel production was modelled using the PowhegBoxv2 [93, 57, 58, 59] generator at NLO in QCD using the four-flavour scheme and the corresponding NNPDF3.0nlo set of PDFs [60]. The events were interfaced with PYTHIA8.230 [62] using the A14 tune [63] and the NNPDF2.3lo set of PDFs [64].

Single-top s-channel production was modelled using the PowhegBoxv2 [94, 57, 58, 59] generator at NLO in QCD in the five-flavour scheme with the NNPDF3.0nlo [60] parton distribution function (PDF) set. The events were interfaced with PYTHIA8.230[62] using the A14 tune [63] and the NNPDF2.3lo PDF set.

5.3 Object, Event Selection and Calibration

5.3.1 Object Definitions

In this section, we will describe the tools used to reconstruct and identify the main particles in this study.

Muons: Muons are required to pass a specific isolation and medium criteria defined by Atlas CP Group which is called `PFlowTight_FixedRad` isolation and medium quality criteria, have $|\eta| < 2.5$ and p_T to be greater than 27 GeV.To reduce pile-up and remove cosmics and extremely badly reconstructed muons we require the distance to the primary vertex along the z-axis, z_0, to be $|z_0 \sin\theta| < 0.5$ mm. Here θ is the polar angle of the track. We also require that the significance of the impact parameter in the plane perpendicular to the beam direction be $|d_0/\sigma(d_0)| < 3$. (μ, p_T, z_0, d_0) are defined previously in Chapter 3.

Electrons: Electrons are required to pass FixedCutTight isolation requirement (`FCTight`)and the tight log-likelihood (`TightLH`) criteria, have $|\eta| < 2.47$ and p_T greater than 27 GeV. Electrons in the crack region of the electromagnetic calorimeter, $1.37 < |\eta_{\text{cl}}| < 1.52$, are excluded. Here η_{cl} is the pseudorapidity of the cluster produced by the electron in the calorimeter. To reduce pile-up and extremely badly reconstructed electrons we require $|z_0 sin\theta| < 0.5$ mm and $|d_0/\sigma(d_0)| < 5$.

Jets: Jets from the jet collection use `AntiKt4EMPFlowJets` which is a name for a specific jet clustering algorithm used to identify jets of particles in the detector. A radius of 0.4 indicates the size of the cone used by the jet algorithm to cluster particles together. The jet collection uses information from both electromagnetic and hadronic energy deposits in the detector and utilizes a sophisticated technique that combines information from tracks and energy deposits in the detector to reconstruct jets. The jets in the Monte Carlo are smeared to correct for differences in the jet resolution between data and Monte Carlo. For jets with $25 < p_T < 60$ GeV and $|\eta| < 2.4$ pile-up suppression cuts in the form of Jet Vertex Tagger(JVT). Jet Vertex Tagger is a technique used to distinguish between jets originating from the primary proton-proton collision and jets arising from other processes,`JVT` > 0.59 are applied. Only jets with $p_T > 25$ GeV are considered in the analysis.

B-tagging: Or b-quark tagging, is a method used to identify jets originating from b-quarks, they decay into other particles before they can travel a measurable distance within the detector. The decay of a b-quark within the detector leaves a

signature of a secondary vertex, slightly displaced from the primary collision point where the b-quark was created. The particles produced by the b-quark's decay often have high momentum compared to particles from lighter quark decays. To classify jets as containing a b-hadron we use the 70% efficiency working point of the `DL1r` algorithm (`FixedCutBEff_70`).

Overlap Removal: Overlap procedures are used in detectors to prevent a single physical object from being misinterpreted as two separate objects. This is particularly important for separating signals from leptons (like electrons or muons) in the calorimeter from signals originating from hadronic jets. This is performed using the standard methods provided by the top reconstruction group.

5.4 Event Selection

In this section, we will describe the criteria applied to obtain the signal and control samples, as well as the weights assigned to those samples.

5.4.1 Signal sample

We select a *signal sample* enriched in $t\bar{t}$ events. This selection process involves criteria isolating signal events and reducing background contributions. The details of this selection process are as follows:

- Two leptons (electrons or muons) of the same flavour and opposite charge;
- One of the lepton must be trigger-matched to one of the single lepton triggers.
- At least two b-tagged jets
- The invariant mass of the tag and probe leptons must exceed 15 GeV to exclude low-mass resonances
- Events with a resonant mass of two leptons between 85 and 95 GeV [95] are excluded to suppress events that could come from Z^0 production.

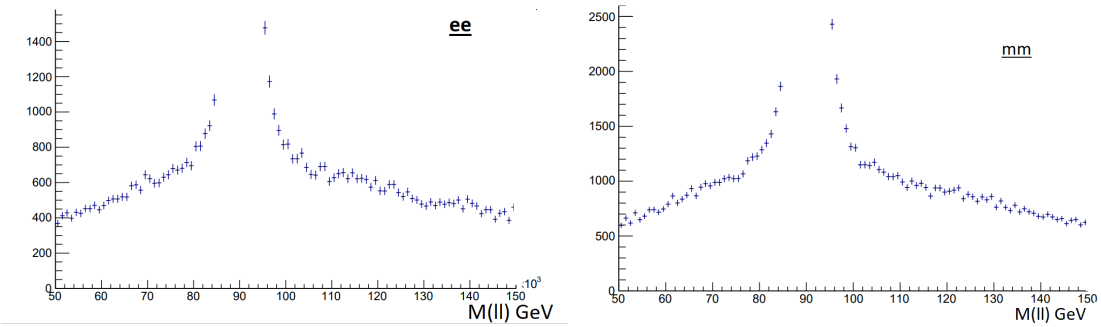

Figure 5.1: Mass distribution of electron and muon events for data (left/right) after excluding those from Z^0 production [95].

5.4.2 Control sample

We use a *control sample* containing mainly $Z^0 \to l^+l^-$ events to measure C_{eff}. This sample is selected by applying the following requirements:

- Two leptons (electrons or muons) of the same flavour and opposite charge;
- One of the lepton must be trigger-matched to one of the single lepton triggers. The required triggers are the same as for the signal sample specified above;
- at least two jets in the event;
- The invariant mass of two leptons must be in the range between 80 and 105 GeV;

5.4.3 Weights applied to MC events(calibration)

The weight assigned to each Monte Carlo (MC) event is a product of several factors calculated by the top reconstruction group. These factors account for the weight produced by the MC generators (`weight_mc`), adjustments to match the pileup distribution in data (`weight_pileup`), corrections for leptons (`weight_leptonSF`), trigger efficiencies for tagged leptons (`weight_tag_triggerSF`), b-tagging efficiency (`weight_bTagSF`), and the distribution of a variable called JVT (`weight_jvt`).

5.5 Background Efficiencies

5.5.1 Z^0 Correction Factor

The Drell-Yann process is the largest source of background for both e^+e^- and $\mu^+\mu^-$ channels. $Z^0 \to l^+l^-$ decay process is removed from the analysis using the cut on the mass of l^+l^- $85 < M(ll) < 95$ GeV [96]. However, a scale factor (SF) is needed to account for non-resonant Drell-Yann processes. This scale factor is measured directly in data. To do this, $Z^0 \to l^+l^-$ contribution is included (unlike in the main analysis) in the analysis sample. It is assumed that the non-resonant l^+l^- production scales similarly to $Z^0 \to l^+l^-$ decay. Therefore, the single correction factor is applied to both resonant and non-resonant Drell-Yann contributions.

The Z^0 correction factor is obtained as:

$$SF = \frac{N_{\text{data}}}{N_{\text{MC}}} \tag{5.9}$$

where N_{data} and N_{MC} are the number of events in the Z^0 resonance peak in data and MC, respectively.

To calculate the SF we fit the invariant mass distribution $M(ll)$ in the range of 50000 to 140000 MeV. We use the Voigt profile to describe the signal of Z^0. The Voigt profile is defined as the convolution of a Breit-Wigner distribution with a Gaussian distribution. Equation 5.10 shows the PDF of the signal.

$$VP(M; M_0, \sigma, \Gamma) = \int_{-\infty}^{\infty} \frac{e^{-(M-x)^2/\left(2\sigma^2\right)}}{\sqrt{2\pi}\sigma} \cdot \frac{\Gamma}{\pi\left(\left(x - M_0\right)^2 + \Gamma^2\right)} dx \tag{5.10}$$

Here M is the mass of l^+l^-, M_0 is the mass of the Z^0 boson, σ is the R.M.S. of the Gaussian distribution which represents the resolution of the detector and Γ is the width of the Breit-Wigner, which is fixed to the PDG value of the width of Z^0, $\Gamma = 2.495$ GeV. For the non-resonant PDF, we use the Chebychev polynomial of 3rd degree.

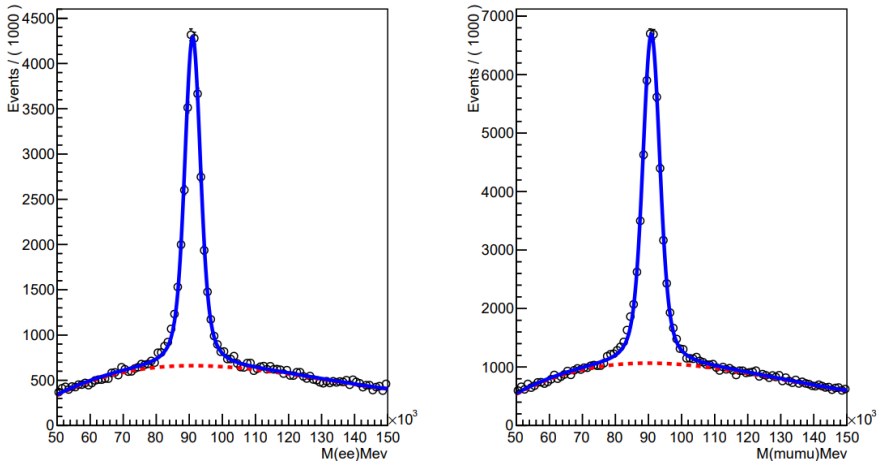

Figure 5.2: Fitted mass distribution with one Voigt profile for data: electron to the left and muon to the right. The blue line represents the signal and the red dotted line represents the non-resonant background.

Table 5.4 shows the values of M_0, σ, and the total number of events N for the data and MC. The fitted distribution of M for the data and MC are shown in figure 5.2 and 5.3, respectively.

One voigt profile	N_Z	σ	M_0
$Z^0 \to ee$(data)	26012 ± 225	1808 ± 31	91006 ± 24
$Z^0 \to ee$(MC)	20965 ± 208	1800 ± 35	90854 ± 27
$Z^0 \to \mu\mu$(data)	43025 ± 293	2013 ± 25	90855 ± 20
$Z^0 \to \mu\mu$(MC)	35265 ± 277	2072 ± 29	90792 ± 23

Table 5.4: The values of the main parameters for fitting the invariant mass distribution for data.

From these results we obtain

$$\begin{aligned} SF_{ee} &= 1.241 \pm 0.016 \\ SF_{\mu\mu} &= 1.220 \pm 0.013 \end{aligned} \tag{5.11}$$

There is a good consistency between the scale factors of electrons and muons.

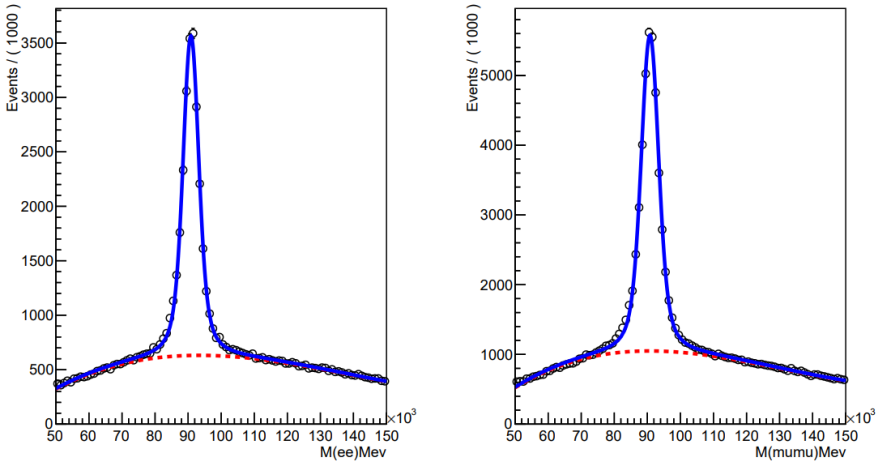

Figure 5.3: Fitted mass distribution with one Voigt profile for MC: electron to the left and muon to the right. The blue line represents the signal and the red dotted line represents the non-resonant background.

5.5.1.1 Systemic uncertainty for scale factors

When we fit with one Voigt profile, the data points deviate from the fitted curve for the low values of $M(ll)$ as shown in the figure 5.4 and5.5.

The reason for this tail is the photon radiation phenomenon. When an electron or muon passes through the detector material, it emits photons and loses energy as a result. Therefore, if we compute the mass of two leptons and one of them has a smaller energy, the resulting mass will be smaller than the initial mass of the two leptons. Although electrons or muons emit photons, they still originate from Z^0 and we need to include them in our signal. Therefore fitting with a single Voigt profile may be not perfect.

We can check the impact of this effect on our scale factors by fitting our distributions with two Voigt profiles. The PDF of the signal is given in Eq. 5.12.

$$VP2(M; M_1, M_2, \sigma, \Gamma) = VP(M; M_1, \sigma, \Gamma)\cdot f + VP(M; M_2, \sigma, \Gamma)\cdot(1-f) \quad (5.12)$$

Here f is the fraction of the first voigt profile, and M_1 and M_2 are free parameters in the fit. The resolution σ is a free parameter in the fit but it is the same for the two Voigt profiles. The width Γ is fixed to the PDG value of the Z^0 and it is the same

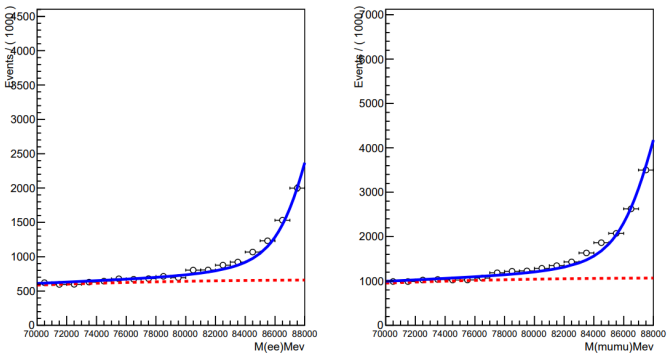

Figure 5.4: Zoom on the mass distribution fitted with one Voigt profile for data show the deviation of the fitted function from the data points

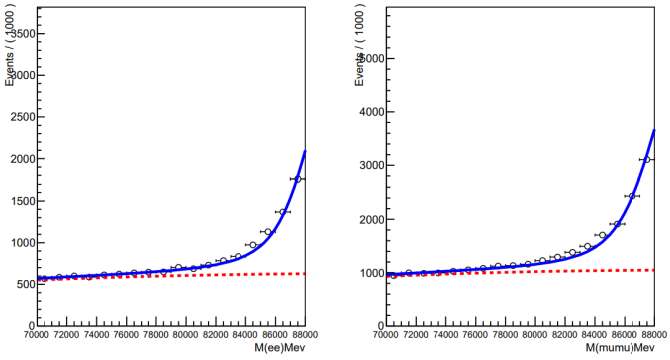

Figure 5.5: Zoom on the mass distribution fitted with one Voigt profile for MC show the deviation of the fitted function from the data points

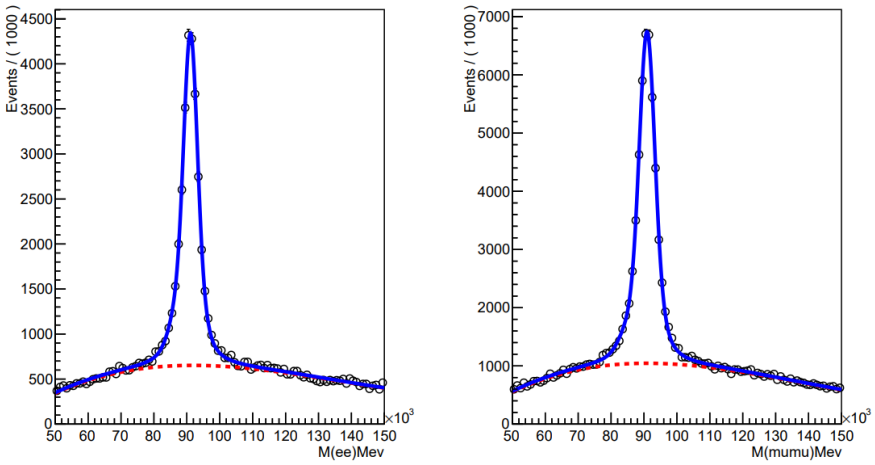

Figure 5.6: Fitted mass distribution with two Voigt profiles for data: electron to the left and the muon to the right

as the one Voigt profile. So the difference between the two and one Voigt profiles is only the central value of the mass.

Figure 5.6 and 5.7 show the fitted mass distribution with two Voigt profiles for data and MC, respectively. Table 5.5 shows the obtained parameters from the fit with two Voigt profiles in data and MC. In addition, we add the second mass M_2 and the fraction of the second Voigt profile (f) to this table.

By comparing the maximum log-likelihood between fitting of samples with one and two Voigt profiles we found that the value of maximum log-likelihood increased by 29 units for electron events and 32 units for muons, and in MC it is increased by 13 units for electrons and 22 units for muons which means the fit quality has improved. Figure 5.8 and 5.9 show this improvement in the tail of the mass distribution.

The systematic uncertainty on the scale factor for the Z^0 contribution to the signal sample has been determined by comparing the fit results using one and two Voigt profiles and comparing the fit results.

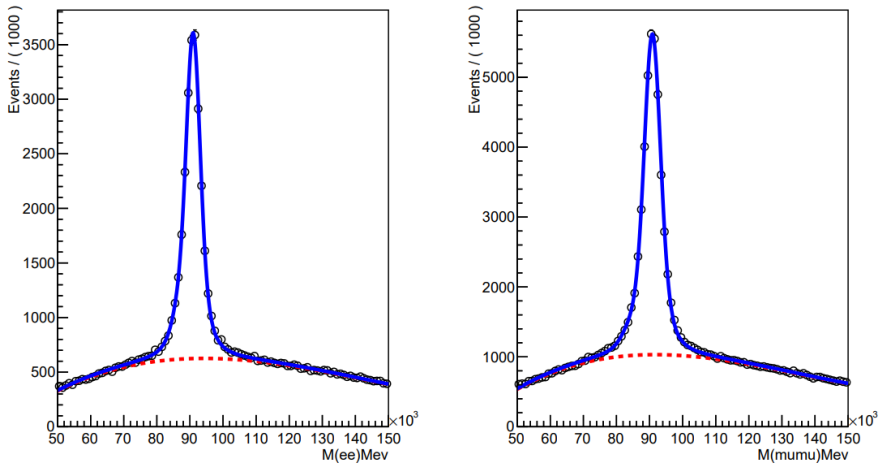

Figure 5.7: Fitted mass distribution with two Voigt profiles for MC: electron to the left and the muon to the right

Two Voigt profiles	N_Z	σ	M_1	M_2	f
$Z^0 \to ee(data)$	26408 ± 245	1684 ± 46	91109 ± 39	85802 ± 692	0.95 ± 0.01
$Z^0 \to ee(MC)$	21223 ± 221	1655 ± 53	90980 ± 50	86300 ± 686	0.94 ± 0.015
$Z^0 \to \mu\mu(data)$	43939 ± 329	1935 ± 31	90925 ± 25	84036 ± 564	0.96 ± 0.005
$Z^0 \to \mu\mu$(MC)	36033 ± 316	1996 ± 37	90860 ± 29	83848 ± 701	0.96 ± 0.006

Table 5.5: The values of the main parameters for fitting the invariant mass distribution for two Voigt profiles data

The results of the SF with two Voigt profiles are given in Eq. 5.13.

$$\begin{aligned} SF_{ee} &= 1.244 \pm 0.017 \\ SF_{\mu\mu} &= 1.223 \pm 0.013 \end{aligned} \tag{5.13}$$

The scale factors of the two Voigt profiles are very similar within the uncertainties of the fit. Since the difference between the two results is very small, we set the uncertainty derived from the uncertainty of the fit of the scale factor. The value of this uncertainty is given in 5.14:

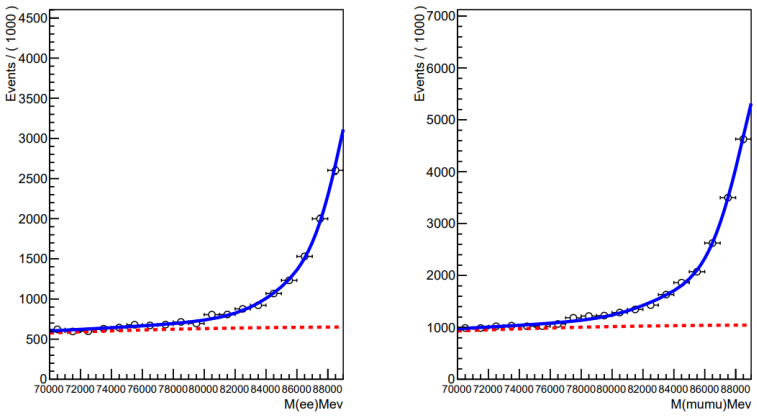

Figure 5.8: Fitted mass distribution with two Voigt profiles for data: electron to the left and the muon to the right

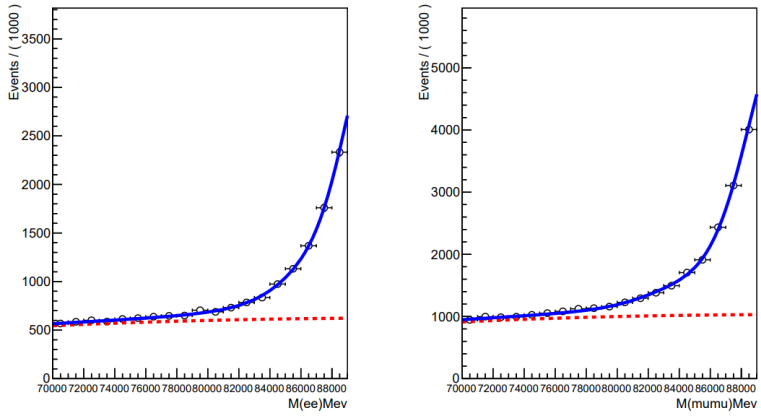

Figure 5.9: Fitted mass distribution with two Voigt profiles for MC: electron to the left and the muon to the right

$$\begin{aligned} \sigma(SF_{ee})/SF_{ee} &= 1.3\% \\ \sigma(SF_{\mu\mu})/SF_{\mu\mu} &= 1.0\% \end{aligned} \tag{5.14}$$

5.5.2 Fakes

Fake electrons and muons contribute significantly to the background noise. The procedure of measuring the scale factor of fake electrons and muons is described in [54]. The main idea of this study is to differentiate between fake electrons coming from different sources, such as photon conversion or decays of bottom mesons. By applying separate correction factors to these categories, a more accurate measurement is achieved. The method involves fitting the data to a model that considers the composition of fake electrons based on their origin and momentum. This allows for tailored correction factors for different types of fake electrons. The study also demonstrates the effectiveness of the new method by comparing the data before and after applying the correction factors. The results show a significant improvement in the agreement between data and simulations. The systematic uncertainties associated with the method, particularly the dependence on the simulation of the top quark pair production process are also included.

The scale factor C^{fake} for electrons and muons with $p_T > 20$ GeV is found to be

$$C^{\text{fake}}(e) = 0.88 \pm 0.04 \tag{5.15}$$

$$C^{\text{fake}}(\mu) = 1.36 \pm 0.03 \tag{5.16}$$

5.6 Model Fitting

To determine the ratio $R(\mu/e)$, this analysis employs a profile likelihood fit performed using ATLAS's TRExFitter package [97].

5.6.1 Fit setup

The analysis relies on a likelihood function that incorporates all the parameters being estimated. This function includes the parameter of interest (POI) for this analysis $R(\mu/e)$. It also takes into account uncertainties in our measurements as nuisance parameters, represented by the symbol θ.

Single-bin histograms are used for this analysis to calculate the number of events, the likelihood function represents the probability (P) of observing the actual number of events (n_i). Each measurement region is described by a Poisson distribution and the likelihood function is simply the product across all bins, with a probability density function for systematic. Here, G represents a Gaussian distribution and the number of bins is one.

$$L(n, \theta^0 | R(\mu/e), \theta) = \prod_{i \in \text{bins}} P(n_i | R(\mu/e)(\theta)) \times \prod_{j \in \text{NPs}} G(\theta_j^0 | \theta_j) \tag{5.17}$$

The fit is set up with four floating parameters: $R(\mu/e)$, the parameter of interest (POI), Normalization factor applied to MC $t\bar{t}$ events $C(t\bar{t})$,

$C(Z^0)$, normalization factor applied to MC ($Z^0 \to l\bar{l}$) events(e.g.The ratio of data to Monte Carlo for the number of events for Z^0 production applied both to ee and $\mu\mu$).

$C_{eff}(\mu/e)$, the ratio of selection efficiencies between $\mu\bar{\mu}$ and $e\bar{e}$, applied to the $\mu\bar{\mu}$ event, this factor takes into account that there could be differences in the efficiency between muon and electron. (described in section 5.5.1).

This scale factors applied as follows:

$$\begin{aligned} N^{Exp}\left(Z^0 \to ee\right) &= N^{MC}\left(Z^0 \to ee\right) \cdot \left(C(Z^0)\right) \\ N^{Exp}\left(Z^0 \to \mu\mu\right) &= N^{MC}\left(Z^0 \to \mu\mu\right) \cdot \left(C(Z^0)\left(C_{eff}(\mu/e)\right)\right) \end{aligned} \tag{5.18}$$

where N^{Exp} is the expected value. The configuration file used for the analysis defines four signal regions: e^+e^- events in $t\bar{t}$ selection ($t\bar{t} - ee$), $\mu^+\mu^-$ events in $t\bar{t}$ selection ($t\bar{t} - \mu\mu$), e^+e^- events in Z^0 selection ($Z^0 - ee$) and $\mu^+\mu^-$ events in Z^0

selection ($Z^0 - \mu\mu$). Additionally, it defines four validation regions based on Pseudo-rapidity(η) distributions: e^+e^- events in $t\bar{t}$ selection ($tt - ee - \eta$), $\mu^+\mu^-$ events in $t\bar{t}$ selection ($tt - \mu\mu - \eta$), e^+e^- events in Z^0 selection ($Z^0 - ee - \eta$), and $\mu^+\mu^-$ events in Z^0 selection ($Z^0 - \mu\mu - \eta$). The $t\bar{t}$ signal regions include six contributions,

Dilepton decays ($tt \to ll$): This includes decays where both the t and $\bar{t}$ quark decay into a W boson and a bottom quark (b). The W boson then subsequently decays into a lepton (e or μ) and a neutrino (ν_e or ν_μ). This results in final states with two leptons (either ee or $\mu\mu$).

Single-lepton + tau decays($tt \to l\tau$): In this channel, one of the t or $\bar{t}$ quarks decays into a tau lepton along with a b quark and a neutrino. The other t or $\bar{t}$ decays into a W boson and a b quark, which further decays into a lepton and a neutrino. This leads to a final state with one lepton (e or μ) and a tau lepton.

tau decays($tt \to \tau\tau$): Here, both the t and $\bar{t}$ quarks decay into a tau lepton and a b quark along with a neutrino. This results in a final state with two tau leptons. The additional contribution from the Z boson decay ($Z^0 \to e^+e^- or \mu^+\mu^-$). This process can mimic the genuine decays of tt.

fake leptons that mimic real leptons. These can arise from misidentified jets or other particles in the collision.

Decays from other sources: Processes decay into two leptons can also contribute to the overall dilepton sample.

The Z^0 regions include five contributions; it primarily consists of decays of the Z^0 itself into two leptons. And a contribution from the decay of $t\bar{t}$ leading to final states with two leptons($tt \to ll$), one lepton and a tau ($tt \to l\tau$), or two taus ($tt \to \tau\tau$) and a contribution of fake lepton, as shown in the table 5.6.

There are several other important normalization factors involved in the fitting process.

The normalization of the fake-lepton background is extracted from data, as described in Section 5.5.2,

Sample	**contribution**
$t\bar{t}$ samples	dilepton decay ($tt \to ll$) , $l = e, \mu$
	lepton-tau decay ($tt \to l\tau$)
	tau-tau decay ($tt \to \tau\tau$)
	prompt lepton ($Z^0 \to ll$)
	fake leptons (fake)
	other decay sources (other)
Z^0 samples	$(tt \to ll)_{Z0}$
	$(tt \to l\tau)_{Z0}$
	$(tt \to \tau\tau)_{Z0}$
	$Z^0 \to ll$
	fake

Table 5.6: The list of the $t\bar{t}$ samples and Z^0 samples.

The normalization of the Z+jets background is also determined directly from the experimental data as explained in section 5.5.1. This number is not considered a fixed value but a parameter that can vary within a certain range. The starting point (nominal value) for this parameter is set based on the data analysis, and the allowed variation around this value is set to 1σ(standard deviation) of the uncertainty in the data analysis method described in section 5.5.1.

All other backgrounds detailed in section 5.2.3 are normalised using calculations that predict how often these events should occur and are treated as nuisance parameters. This means they can vary within a certain range. The starting point (nominal value) for each parameter comes from the calculations, and the allowed variation around this value is set to 1σ of the uncertainty given by the uncertainties on these higher-order cross sections.

There can be other uncertainties that affect the analysis due to how well the data matches the expected pattern (shape effects) and how efficiently events are detected

(acceptance effects). These uncertainties are also considered as nuisance parameters during the process of fit.

5.7 Uncertainties due to systematic effects

This section will discuss the systematic uncertainties that affect the $R(\mu/e)$ calculation.

The analysis strategy reflected in Eq. 5.3 ensures that many systematic uncertainties are significantly reduced in the measurement of $R(\mu/e)$. In particular, the systematic uncertainties due to jet reconstruction and b-tagging cancel because the selection of jets and b-tagging is not sensitive to the flavour of the two isolated leptons present in the event. Similarly, the uncertainties related to the reconstruction and identification of electrons or muons are reduced because the impact of these uncertainties in the signal ($t\bar{t}$-enriched) and control (Z^0-enriched) samples is similar. The residual systematic uncertainties due to the above sources are determined using the procedure prescribed by the Top working group and Physics Modeling group.

For the experimental systematic uncertainties, we correlate each uncertainty component across various processes as well as across the signal and control samples using the correlation model that is provided by the relevant CP groups. We similarly correlate the theoretical modelling uncertainties across e^+e^- and $\mu^+\mu^-$ channels. The data-driven uncertainties we identified are specific to particular processes within this analysis. Their relationships with each other, or "correlation structure," are discussed in the following sections.

5.7.1 Smoothing of the Systematic Variations

Systematic uncertainties are included as nuisance parameters in TRExFitter [97]. To improve the fitting process, TRExFitter automatically removes unnecessary systematic uncertainties (pruning)and smooths out input histograms in the data. TRExFitter discards uncertainties whose impact on the fit results in terms of overall

normalization is smaller than a predefined threshold of 0.001. Figure 5.10 illustrates the final set of systematic uncertainties for the analysis.

5.7.2 Systematic Uncertainties from Data-driven Corrections

We determined the amount of fake-lepton background, as well as the backgrounds from $Z \to \mu^+\mu^-$, using special data samples as explained in Section 5.5. These background amounts, along with their uncertainties, are then included in the overall fitting process.

5.7.2.1 fake-lepton background

The uncertainty in the amount of fake leptons in our analysis comes from two sources, which are explained in more detail in Section 5.5.2. The first source is the uncertainty due to using a limited amount of data for the fake lepton estimate the same sign (SS dataset). The second source is the uncertainty derived by using different MC generators to simulate these fake leptons. The sizes of these uncertainties have been previously estimated in [98] and are summarized in Table 5.7.

Channel	Normalisation factor	`tt_fake_stat`	`tt_fake_gen`
e^+e^-	0.88	$\pm$ 4.3%	$\pm$ 5.1 %
$\mu^+\mu^-$	1.36	$\pm$ 3.1%	$\pm$ 5.1%

Table 5.7: Normalisation factors and the corresponding uncertainties on the fake electron and muon background.

5.7.2.2 $Z^0 \to e^+e^-$ and $Z^0 \to \mu^+\mu^-$ background

The amount of background from Z boson decays, ee and $\mu\mu$-channel is tightly controlled by analyzing a control region. The resulting background level and its

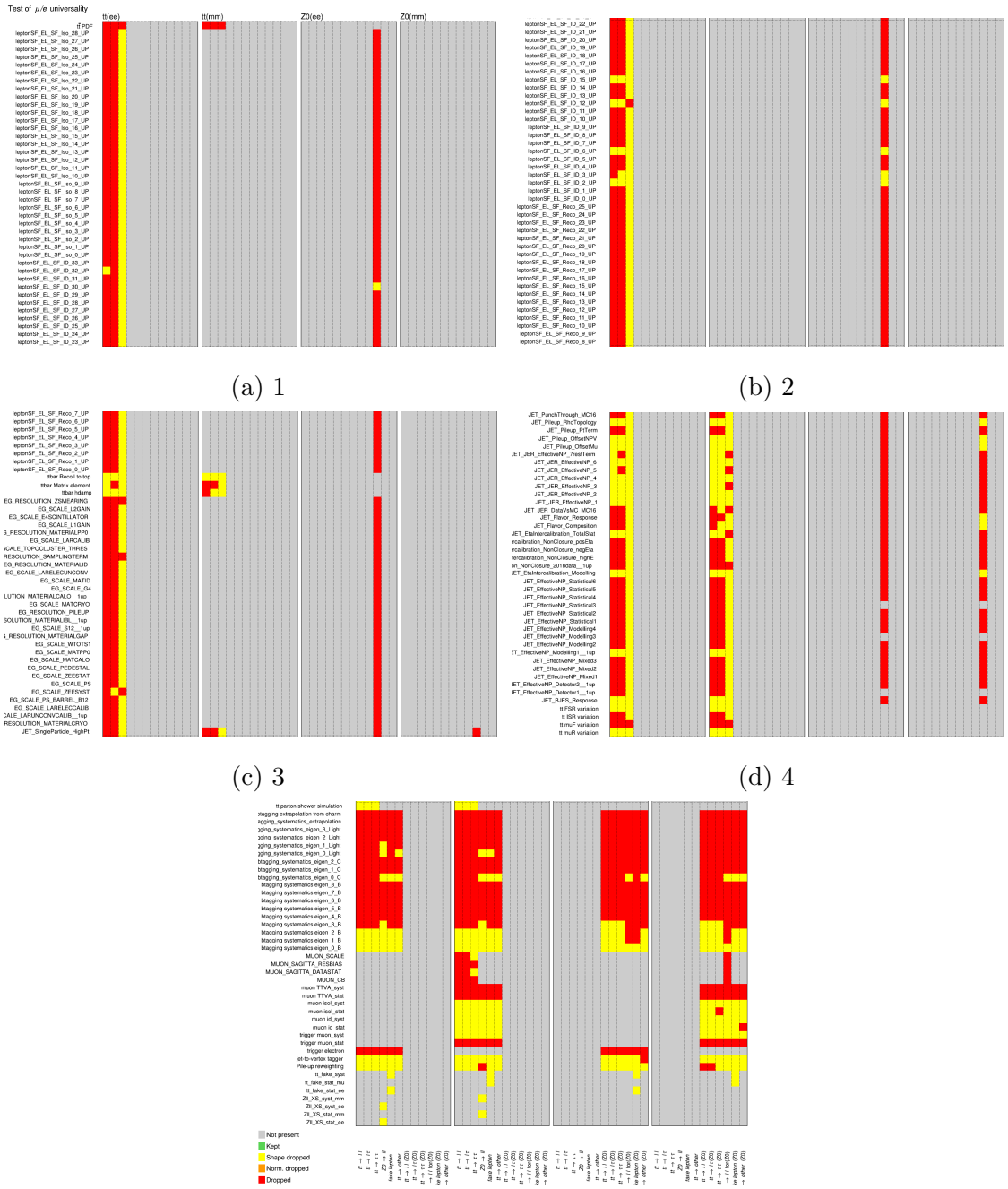

(a) 1

(b) 2

(c) 3

(d) 4

(e) 5

Figure 5.10: Pruning with a threshold of 0.001 applied in TRExFitter. The figure is divided into five parts to make it visible. Each systematic uncertainty for a given sample and region is categorized as normalization: the normalization kept(yellow) or completely dropped(red). Systematics that are not applied to a given sample and region are marked as grey.

uncertainty for both electron and muon channels are listed in Table 5.8. The details on deriving this factor are given in Section 5.5. The uncertainty itself comes from two sources: the limited size of the data and MC Z boson samples used in the analysis.

Additionally, we considered a potential uncertainty arising from the specific mathematical functions used to estimate the Z boson background level. Changing the signal model from a single Voigt function to a double Voigt function resulted in an additional uncertainty.

Channel	Normalisation factor	`XS_stat`	`XS_syst`
ee	1.241	$\pm$ 1.7%	$\pm$ 1.3%
$\mu\mu$	1.22	$\pm$ 1.3%	$\pm$ 1.0%

Table 5.8: Normalisation factors and the corresponding uncertainties on the $Z^0 \to e^+e^-$ and and $Z^0 \to \mu^+\mu^-$ background.

5.7.3 Systematic uncertainty from the reconstruction of muon and electron in simulated samples

5.7.3.1 Systematic from muon reconstruction and identification

Muon-related uncertainties are incorporated using dedicated systematic variations. Four prescription trees defined by the Muon CP group are employed for this purpose, specifically targeting the lepton scale factor due to muon reconstruction and identification within the 'AnalysisTop: Systematics AllMuons' configuration. These variations encompass both statistical and systematic uncertainties in muon identification and isolation. Additionally, uncertainties related to the correction of the muon momentum scale and resolution are included. These cover variations in combined track resolution, overall momentum scale, and charge-dependent variations in momentum scale based on residual bias after correction. The following

uncertainties are obtained by varying the muon scale factor:

- `muon_identification_syst`: identification statistical uncertainty;
- `muon_identification_stat`: identification systematic uncertainty;
- `muon_isolation_stat`: isolation statistical uncertainty;
- `muon_isolation_syst`: isolation systematic uncertainty.
- `MUON_CB`: Variations in the combined track resolution;
- `MUON_SCALE`: Variations in the momentum scale;
- `MUON_SAGITTA _RESBIAS`: Variations in the scale of the momentum (charge dependent), based on the residual charge-dependent bias after correction.

5.7.3.2 Systematic from electron reconstruction and identification

This analysis incorporates uncertainties related to the electron scale factor due to identification and reconstruction. The simulation of Z boson decay to electron-positron pairs ($Z^0 \rightarrow e^+e^-$) utilizes the Sherpa 2.2.1 Monte Carlo generator. Additionally, systematic variations are defined by the EGamma CP group (30 in total). We use the following configuration of AnalysisTop: ElectronEfficiencySystematicModel SIMPLIFIED EgammaSystematicModel FULL_ETACORRELATED_v1.

These variations encompass both statistical and systematic uncertainties in electron identification(ID), reconstruction(Reco), and isolation(iso). Each group (`Reco`, `ID`, or `Iso`) includes a large number of scale factors provided by the EGamma CP group (89 scale factors in total), Furthermore, uncertainties associated with the correction of electron momentum scale and resolution are included, covering factors like:

- `EG_RESOLUTION_MATERIALCRYO`: EGamma resolution uncertainty;
- `EG_SCALE`: EGamma scale uncertainty;

- `EG_SCALE_AF2`:EGamma scale uncertainty applied to AF2 (Atlas Fast) MC samples.

5.7.4 Sources of uncertainty from MC modelling

5.7.4.1 Theoretical uncertainties related to $t\bar{t}$ production, hadronization and decay

The uncertainties due to the choice of MC generator are estimated by comparing the nominal $t\bar{t}$ sample with several different MC generators and/or sample configurations within the nominal generator described in 5.2.2.

5.7.4.1.1 Matrix element systematic (`tt_ME`) This uncertainty is estimated by comparing the nominal $t\bar{t}$ simulation with the sample generated with pythia8 and pthard = 1 as specified by the physics modelling group.

5.7.4.1.2 ISR systematic (`tt_ISR`) To estimate the uncertainty on the amount of initial state radiation (ISR)the Var3c A14 eigen-tune variations [63] of the strong coupling constant α_s for (ISR), in the A14 tune is applied. The difference between up and down variations divided by 2 is considered a symmetric uncertainty.

5.7.4.1.3 FSR systematic (`tt_FSR`) The impact of final-state-radiation (FSR) is evaluated using PS weights which vary the renormalisation scale for QCD emission in the FSR by a factor of 0.5 and 2.0, respectively. As explained in [99], this systematic uncertainty suffers from large weights which reduce the statistical power of the sample. Therefore these are restricted to be below 10 times the nominal. The difference between up and down variations divided by 2 is considered a symmetric uncertainty.

5.7.4.1.4 $\mu_{R,F}$ systematic (`tt_muR, tt_muF`) To simulate changes to the amount of parton radiation and potential missing higher-order corrections, the renormalisation (μ_R) and factorisation (μ_F) scales are varied up by a factor of 2 and down by a

factor of 0.5. The difference between up and down variations divided by 2 is taken as a symmetric uncertainty. More specifically, to estimate the systematics from μ_R, we use the generator weights " mu_F = 1.0, mu_R = 0.5 " and " mu_F = 1.0, mu_R = 2.0 ". For the systematics from μ_F, the generator weights " mu_F = 0.5, mu_R = 1.0 " and " mu_F = 2.0, mu_R = 1.0 " are used.

5.7.4.1.5 h_{damp} systematic (`tt_hdamp`) A variation of the Powheg h_{damp} value to 3.0 m_{top} is used to vary the resummation scale. This is then symmetrized to form an uncertainty.

5.7.4.1.6 Gluon recoil systematic (`tt_RecoilTop`) The nominal $t\bar{t}$ Monte Carlo employs the recoiling against b quarks to simulate the gluon recoil scheme. The physics modelling group recommends using the recoil-to-top scheme (DSID 601357) for the estimate of the corresponding systematic uncertainty.

5.7.4.1.7 Parton shower and hadronisation systematic The impact of the parton shower and hadronisation model is evaluated by comparing the nominal generator setup with a sample produced with the `POWHEGBOX` [56, 57, 58, 59] v2 generator interfaced with `Herwig` 7.04 [100, 101]. The details of this alternative simulation can be found in [99]. The difference between the nominal and alternative MC simulations is then symmetrised to form an uncertainty.

5.7.4.2 PDF systematic

To estimate the systematic uncertainty due to PDF we follow the recommendation of the top working group [102]. More precisely, we modify the weight of the MC events using the sample of 30 different variations of PDF defined by PDF4LHC15 set [73] and propagate this modification to the measurement of $R(\mu/e)$. The standard deviation of the distribution of 30 values of $R(\mu/e)$ is taken as the systematic uncertainty from this source (`tt_pdf`).

5.7.4.3 Extrapolating from $Z^0 \to \mu + \mu-$ to $Z^0 \to e + e-$

Within the framework of the standard model, we assume that the decay ratios of the Z^0 boson to $\mu^+\mu^-$ and e^+e^- pairs are equivalent. However, experimental measurements of these ratios find a small but noticeable difference. The Particle Data Group (PDG) cites a current precision of the uncertainty 0.24% [14] for this difference.

5.7.5 Other systematic uncertainties

This analysis considers uncertainties arising from both the process of reconstructing jets and the identification of jets originating from bottom quarks (b-tagging). These uncertainties are grouped under `instrumental_jets` and typically have names starting with `JET_` and `bTagSF_`. While their overall impact is minimal, they are included for completeness.

Additionally, uncertainties recommended by the Top group are included. These address potential discrepancies in pile-up reweighting, jet-vertex tagging, and electron and muon trigger efficiencies.

5.8 Fit validation and Asimov fit results

Asimov fit is a statistical analysis technique used in particle physics experiments where a simulated dataset -Asimov dataset- is constructed based on the expected outcome of a model including known uncertainties. This dataset is then fitted using the chosen analysis method to evaluate the method's performance before analyzing real data. The Asimov fit helps to assess the sensitivity of the method to our signal and identify potential biases in the analysis.

This section discusses the results of the fit to an Asimov dataset.

The output value of $R(\mu/e)$ is 1.000 ± 0.007. Table 5.9 provides a more detailed breakdown of the different sources of uncertainty that contribute to this overall value. The analysis estimates $C(t\bar{t})$ to be 1.000 ± 0.013, $C(Z^0)$ is 1.000 ± 0.002

and $Z_{eff}(\mu/e)$ is 1.000 ± 0.003. It is important to note that the sum of squares of each uncertainty would not give the total systematic uncertainty. This is because of the correlation between nuisance parameters. TRexFitter obtains the correlation matrix by calculating the covariance matrix between the fitted parameters and then normalizing it. Figure 5.11 shows the nuisance parameter correlation matrix for the Asimov fit with a threshold of 20% for the minimum correlation. This figure provides valuable information about the relationships between the fitted parameters.

Systematic uncertainties are included as nuisance parameters in TRExFitter. They are combined in the following groups: Data-driven systematic uncertainties are measured using data, Electron identification and reconstruction, Muon identification and reconstruction, Jets reconstruction, other instrumental uncertainties and Theoretical uncertainties. Each of these groups will be discussed in the following sections.

Uncertainty group	$\Delta R(\mu/e)/R(\mu/e)[\%]$
- Data-driven backgrounds	± 0.11
- Theory	± 0.44
- Instrumental electrons	± 0.04
- Instrumental muons	± 0.2
- Instrumental jets	± 0.3
- Instrumental other	± 0.06
- Normalisation factors	± 0.25
Systematics total	0.62
Data statistics	0.17
Total uncertainty	± 0.64

Table 5.9: Uncertainty breakdown from Asimov fit.

Nuisance parameters

Nuisance parameter ranking (effect on POI)

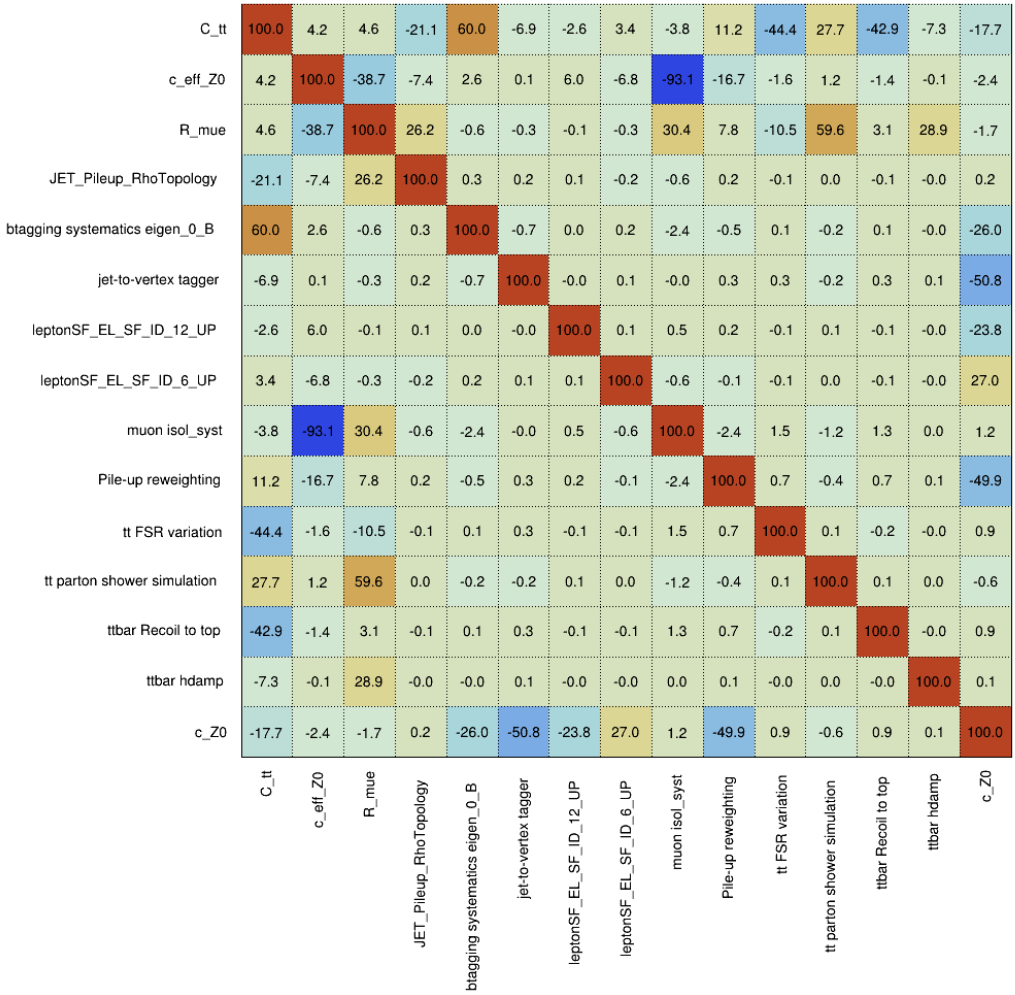

Figure 5.11: Fit parameter correlation matrix for Asimov fit. A high correlation between two parameters indicates that they are strongly correlated, meaning that changing one parameter affects the other. A low correlation suggests that the parameters are relatively independent.

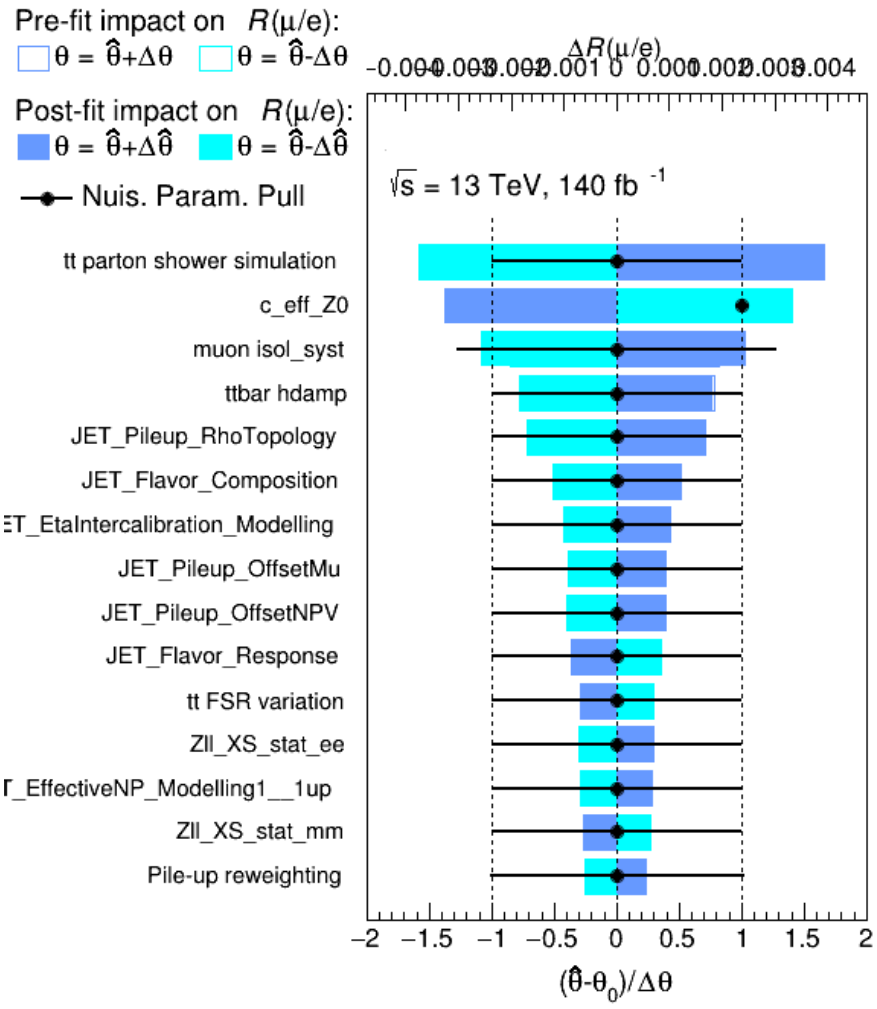

Figure 5.12: Nuisance parameter ranking of all fit parameters for Asimov fit.

The dominant source of systematic uncertainties in the $t\bar{t}$ production cross-section measurement stems from theoretical uncertainties. The parton shower systematic is the largest single contributor, followed by the muon isolation systematic. Jet reconstruction systematic also the jet obtained several positions in the ranking after the muon, as seen in Figure 5.12, which depicts the ranking of nuisance parameters for all fit parameters.

The quality of the fit is satisfactory as evidenced by the absence of pulls or scaling of the nuisance parameters. This indicates that the model adequately describes the data and that the systematic uncertainties are well-characterized.

5.9 Results

The value of the $R(\mu/e)$ ratio was kept hidden to avoid bias from researchers while checking the fit process. This value will be revealed after it has been shown to the top group. This section will illustrate the results before and after the fit. This includes the details of the contribution of the different sources of events in our sample as well as checking the agreement of data/MC, and the influence of nuisance parameters on $R(\mu/e)$.

Before presenting the final results, we will show the pre-fit values to highlight the effect of the fitting procedure on our analysis. Pre-fit in TReXFitter refers to the initial state of the fitting process before any adjustments are made to the parameters based on the data. The contribution of the different sources of the sample before the fit will be presented in yields in Tables 5.10 and 5.11 showing the pre-fit yields for the $t\bar{t}$ and Z^0 channels.

We use the η distribution for validation to perform the fit. The data and MC simulation show good agreement before the fit, as seen in the first row of Figures 5.13 and 5.14 for the $t\bar{t}$ and Z^0 channels, respectively. This agreement is further improved after the fit, as shown in the second row in the same Figures. This improvement is also clear in the Yield after the fit in Table 5.12, where we can compare the number

	$t\bar{t} \to ee$	$t\bar{t} \to \mu\mu$
$tt \to ll$	73000 ± 4000	118000 ± 7000
$tt \to l\tau$	8200 ± 500	13800 ± 900
$tt \to \tau\tau$	238 ± 17	414 ± 31
$Z^0 \to ll$	6360 ± 320	12200 ± 600
$fake$	700 ± 50	223 ± 16
$other$	104 ± 4	148 ± 6
Total	88000 ± 5000	145000 ± 9000
Data	90615	143509

Table 5.10: Yields in the $t\bar{t}$ channel before the fit. It shows that the Dilepton sample is the dominant contributor for $t\bar{t}$.

	$Z^0 \to ee$	$Z^0 \to \mu\mu$
$tt \to ll$	5600 ± 310	9100± 500
$tt \to l\tau$	800 ± 40	1330 ± 80
$Z^0 \to ll$	1.89e06 ± 11000	3.51e06 ± 80000
$fake$	12600 ± 800	1040 ± 70
Total	1.91e6 ± 11000	3.52e06 ± 90000
Data	1.97e6	3.55e06

Table 5.11: Yields in the Z^0 channel before the fit.

of events for data and MC. We can see this agreement as well in Figure 5.15, which illustrates the signal for both ee and $\mu\mu$. Figure 5.13 also shows the composition of samples participating in the $t\bar{t}$ channel analysis. For both the electron and muon regions, the dilepton sample is the most frequent, followed by the lepton-tau and prompt lepton samples. In contrast, Figure 5.14, for Z^0channel, shows only the dilepton events originate from the Z^0 boson, with a negligible contribution from other sources.

	$tt \to ee$	$tt \to \mu\mu$
$tt \to ll$	74800 ± 400	117100 ± 600
$tt \to l\tau$	8440 ± 80	13750 ± 110
$tt \to \tau\tau$	244 ± 12	413 ± 10
$Z^0 \to ll$	6360 ± 320	11900 ± 600
$fake$	700 ± 50	217 ± 15
$other$	104 ± 4	144 ± 5
Total	90620 ± 300	143500 ± 400
Data	90615	143509

Table 5.12: Post fit Yields of the analysis for the $t\bar{t}$ channel, the agreement between data and MC has improved

The normalization parameter $C(t\bar{t})$ processes is extracted as 1.027 ± 0.062 and $C(Z^0)$ is 1.033 ± 0.011 and $C_{eff}(\mu/e)$ is 0.975 ± 0.023.

The fit parameter covariance matrix is shown in Figure 5.16 with a threshold of 20% for the minimum threshold. No major differences were found in the parameter values compared to the Asimov fit shown in Fig. 5.11. The effect of each nuisance parameter on $R(\mu/e)$ and the ranking by largest post-fit effect is shown in Figure 5.17.

The highest contributions to systematic uncertainty come from Theoretical uncertainties. The ordering of the ranking plot is very consistent with that of the

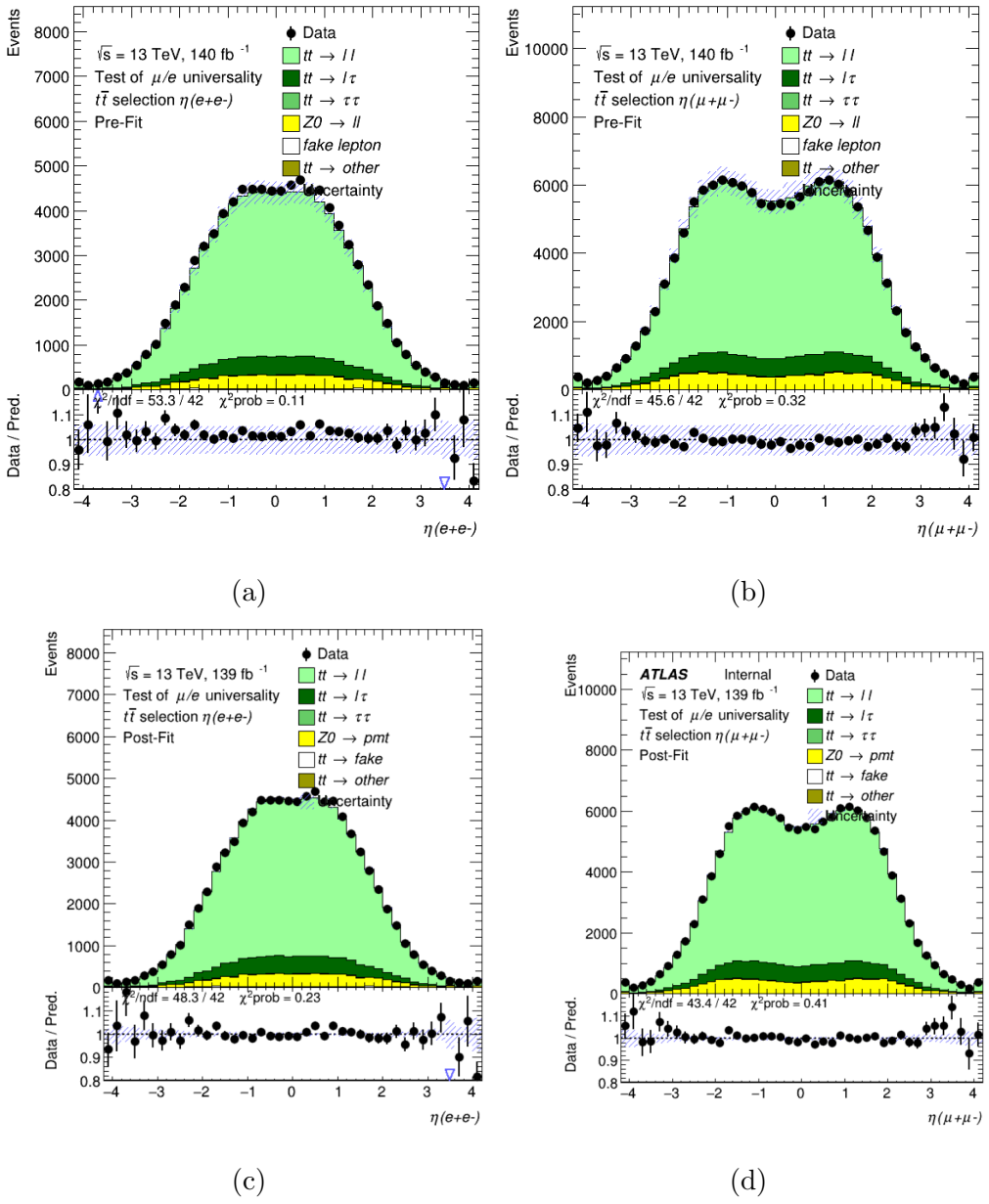

Figure 5.13: η distribution for $t\bar{t}$ channel (the first row before the fit) and (the second row after the fit). Di-lepton sample is the majority of our selected sample and the bottom panel shows the ratio of data to the expected yield, with the blue bands representing the uncertainty. The agreement between the data and MC is improved after the fit.

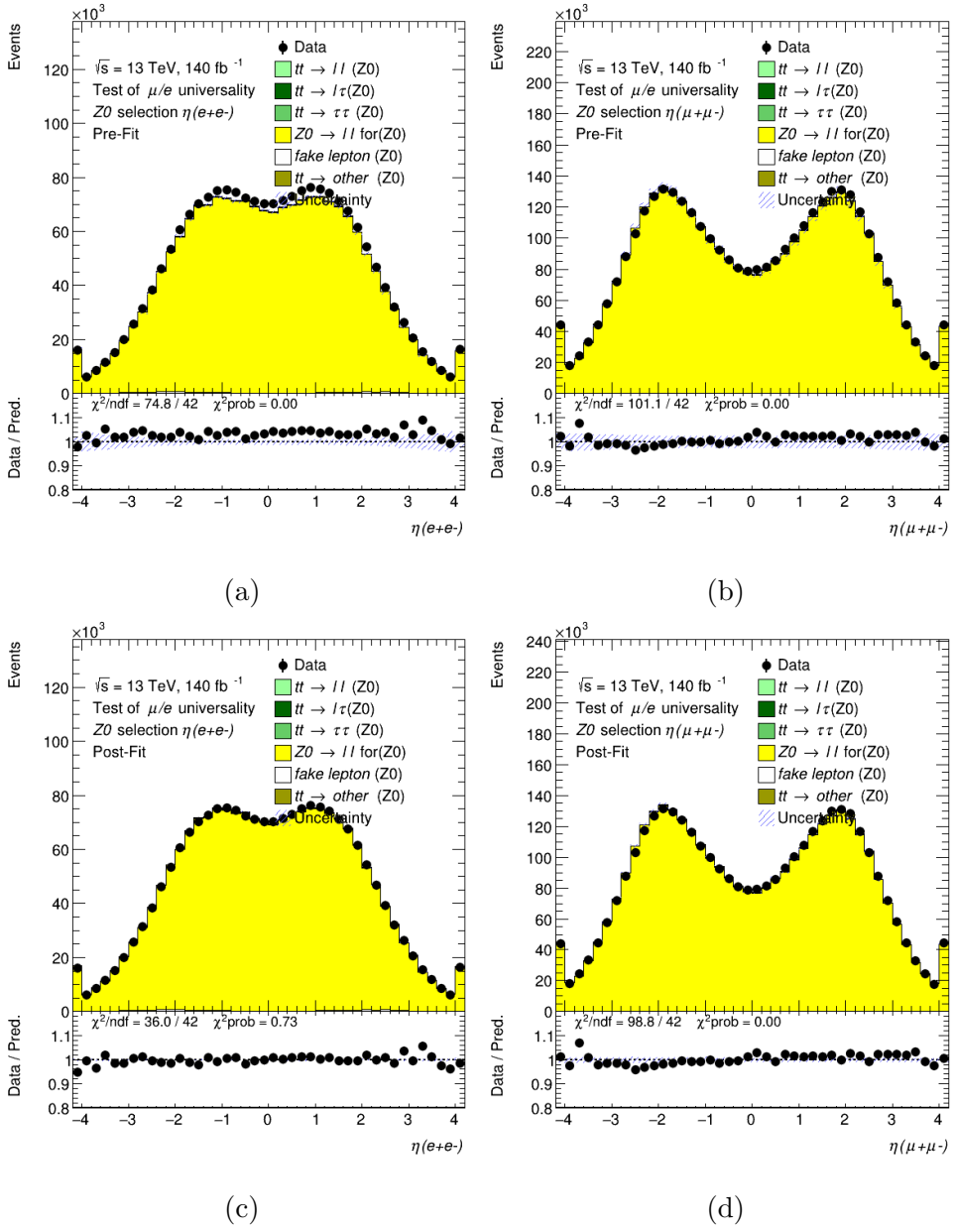

Figure 5.14: The top row shows the η distribution for Z^0 channel before the fit and after the fit (the second row). The Di-lepton contribution dominates the distribution due to the very small number of events from other sources. The bottom box displays the data and expected values, with the uncertainty represented by the blue lines. This visualization demonstrates the improved agreement between data and MC simulation after the fit.

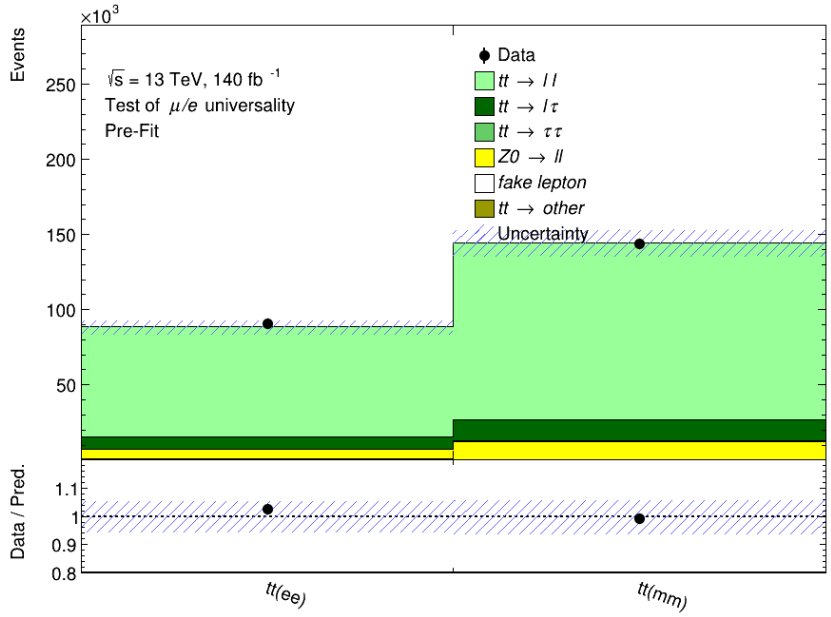

(a)

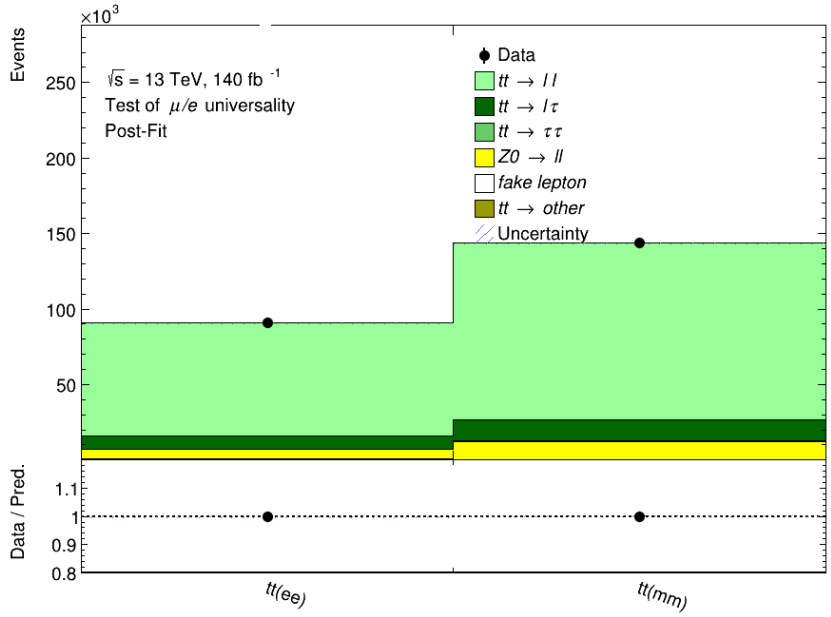

(b)

Figure 5.15: The signal histograms in ee and $\mu\mu$ channel.(a) Pre-fit and (b) after the fit. The agreement between data and MC improved after the fit.

	$Z^0 \to ee$	$Z^0 \to \mu\mu$
$tt \to ll$	5800 ± 600	9100 ± 1000
$tt \to l\tau$	820 ± 80	1330 ± 140
$tt \to \tau\tau$	31.5 ± 3.5	49 ± 5
$Z^0 \to ll$	$1.95e06 \pm 1800$	$3.539e06 \pm 2200$
$fake$	12600 ± 800	1020 ± 60
Total	1.97e6 ± 1400	3.55e06 ± 1900
Data	1.97e6	3.55e06

Table 5.13: Post fit Yields of the analysis for the Z^0 channels, the agreement between data and MC has improved

Asimov fit, preserving the same order of highest impact.

The obtained value of $R(\mu/e)$ uncertainty is

$$\sigma(R(\mu/e)) = 0.00639 \tag{5.19}$$

Table 5.14 provides a comprehensive breakdown of the various uncertainties considered in the analysis.

The achieved systematic uncertainty of 0.006 represents a significant improvement compared to the 0.01 value in the Particle Data Group (PDG). This reduction enhances the precision of our measurement and allows for more sensitive tests of LFU in the future.

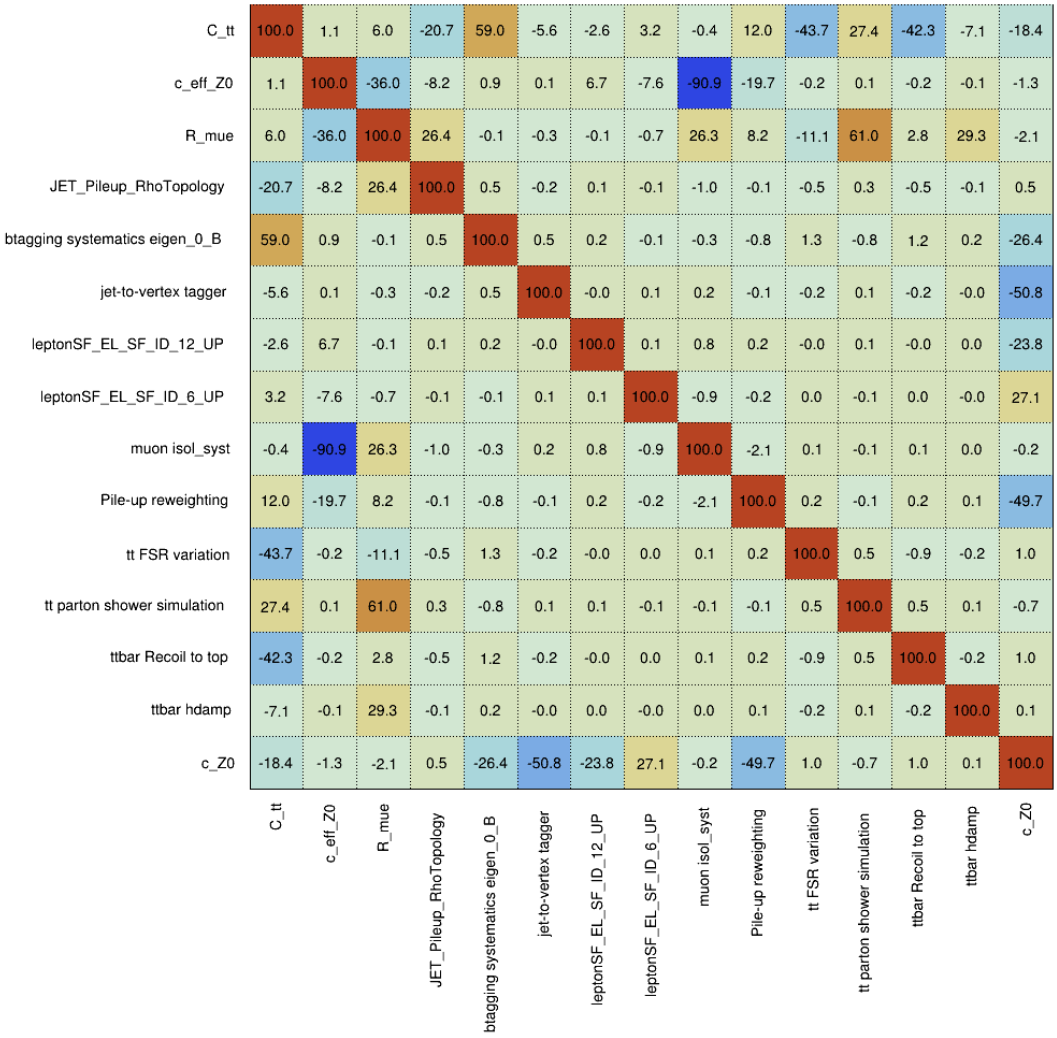

Figure 5.16: Fit parameter correlation matrix.

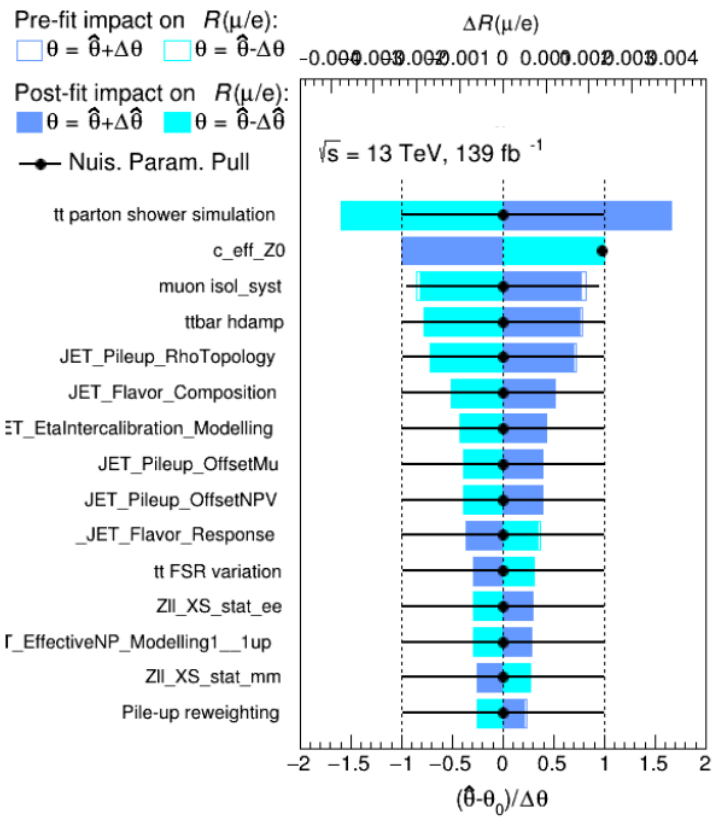

Figure 5.17: Nuisance parameter ranking of all fit parameters

Uncertainty group	$\Delta R(\mu/e)\%$
- Data-driven backgrounds	± 0.11
- Theory	± 0.44
- Instrumental electrons	± 0.04
- Instrumental muons	± 0.2
- Instrumental jets	± 0.3
- Instrumental other	± 0.06
- Normalisation factors	± 0.25
Systematics total	0.62
Data statistics	0.17
Total uncertainty	± 0.64

Table 5.14: Uncertainty breakdown after the fit.

Chapter 6

Conclusions

Lepton flavor universality is an assumption of the Standard Model that the weak interaction between leptons and bosons is independent of the lepton's flavor (electron, muon, or tau). This thesis presents a test of lepton flavor universality by measuring the ratio of branching fractions of the semi-leptonic decay of the top quark to muon and electron through the channels $t \to Wb \to l\nu b$ where $l = \mu, e$. This ratio is

$$R(\mu/e) = \frac{\mathrm{Br}(W \to \mu\nu)}{\mathrm{Br}(W \to e\nu)}. \tag{6.1}$$

by using the data recorded by the ATLAS detector at LHC with an integrated luminosity of $140 fb^{-1}$ of pp collision. The result of this study is blinded until it is shown to the top group. The uncertainty of the value of $R(\mu/e)$ is

$$\sigma(R(\mu/e)) = \pm 0.00639 \tag{6.2}$$

The relative uncertainty has been reduced by 40% from the PDG value. Our investigation into beam spot behaviour across four 2022 pp collision runs (439428, 435333, 435229, and 428580) revealed consistent movement patterns in both vdM and LHCf runs. However, the presence of a crossing angle in physics and LHCf runs introduced some deviations. Notably, the physics run exhibited unexpected movements in beam spot position X (Y direction) and increased width in position Z

(X and Y) for larger separations. Further analysis focused on runs 439428, 435333, and 435229 revealed a consistent pattern in beam spot movement across all three. Additionally, tests confirmed that the scans maintained symmetry across the positive and negative regions.

Our findings provide insights into the beam spot behaviour for different collision configurations. While a consistent pattern emerges, specific runs may exhibit unique characteristics that require further investigation.

For future studies testing lepton flavor universality, consider incorporating data beyond 2015-2018. The higher energy and luminosity of Run 3, which began in 2022, present a valuable opportunity for this research.

Refine selection criteria while maintaining a good signal-to-background ratio. This could involve new kinematic variables like d_0.

Reduce systematic uncertainties that might be affecting the results especially those that become more prominent like theoretical uncertainty in our study, this could involve improved calibration procedures.

Appendix

Appendix A

Run 439428

A.1 The mean position X, Y and Z vs luminosity block

on axis

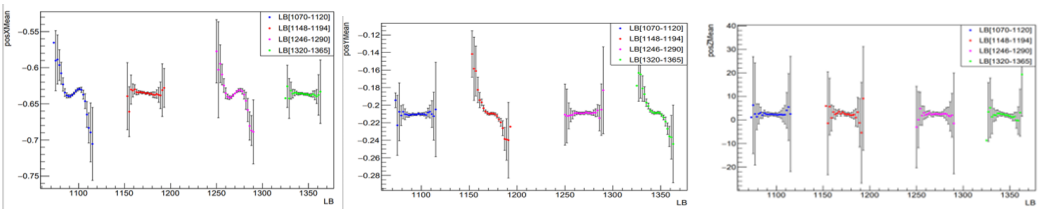

(a) mean position X vs LB (b) mean position Y vs LB (c) mean position Z vs LB

Figure A.1: The mean position X, Y and Z vs lumi block.on-axis

off-axis

A.2 The mean position X, Y and Z vs Nominal separation

on axis in Figure A.3

off axis in Figure A.4

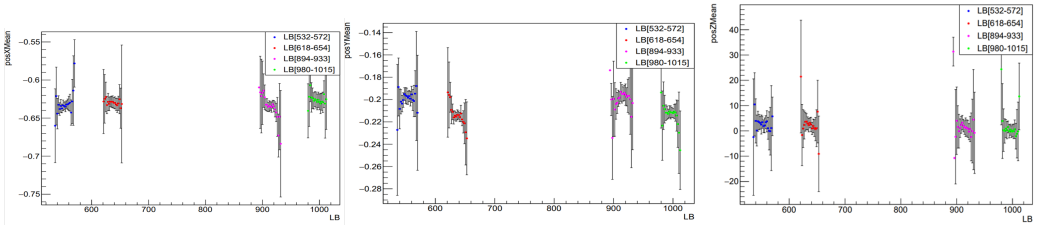

(a) mean position X vs NS (b) mean position Y vs NS (c) mean position Z vs NS

Figure A.2: The mean position X, Y and Z vs lumi block.off-axis

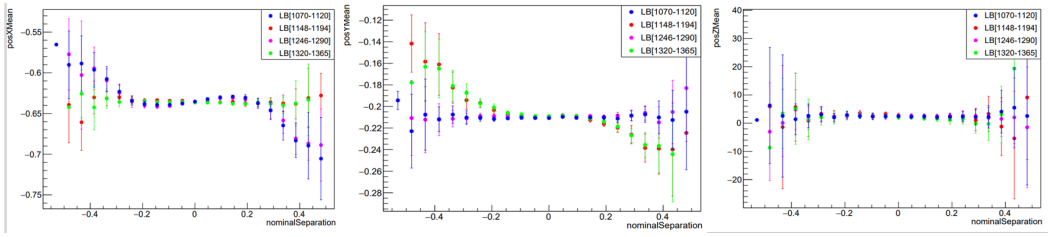

(a) mean position X vs NS (b) mean position Y vs NS (c) mean position Z vs NS

Figure A.3: The mean position X, Y and Z vs Nominal separation. on-axis

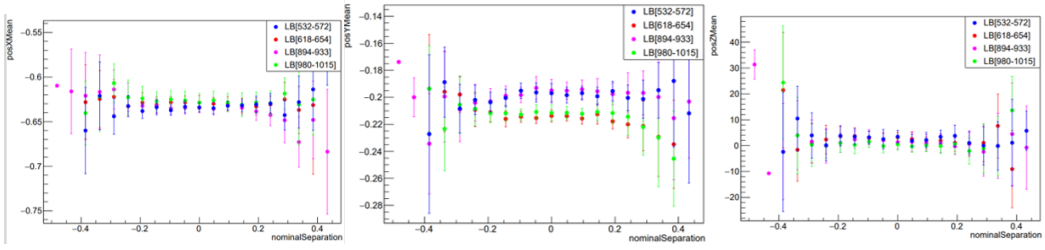

(a) mean position X vs NS (b) mean position Y vs NS (c) mean position Z vs NS

Figure A.4: The mean position X, Y and Z vs Nominal separation. off-axis

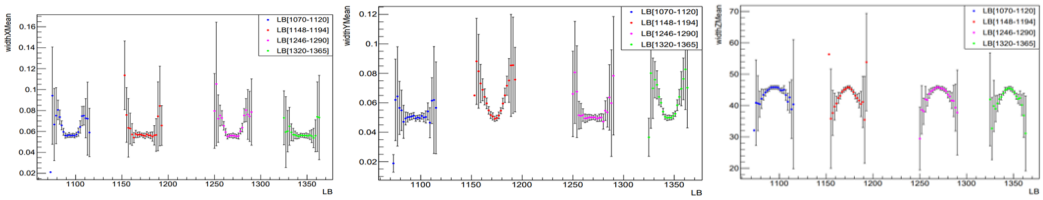

(a) mean width X vs LB (b) mean position Y vs LB (c) mean position Z vs LB

Figure A.5: The width X, Y, Z mean vs Lumi Block. on-axis

A.3 The width X, Y, Z mean vs Lumi Block

on axis

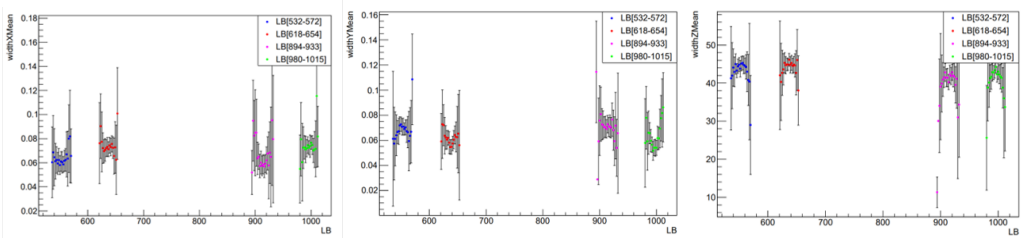

(a) mean width X vs LB (b) mean position Y vs LB(c) mean position Z vs LB

Figure A.6: The width X, Y, Z mean vs Lumi Block. off-axis

A.4 Fitted slope summary run 439428

Scan	Slope Z	Slope X	Slope Y
LB[175-225]	-0.3640 ± 2.7790	0.0239 ± 0.0059	0.0039 ± 0.0050
LB[260-300]	-3.8718 ± 2.6425	-0.0030 ± 0.0054	-0.0283 ± 0.0053
LB[350-400]	-2.2511 ± 2.8776	0.0219 ± 0.0055	0.0031 ± 0.0045
LB[432-480]	-3.0252 ± 2.6101	-0.0057 ± 0.0051	-0.0299 ± 0.0048
LB[532-572]	-1.4501 ± 8.7676	0.0162 ± 0.0203	0.0087 ± 0.0179
LB[618-654]	-6.7275 ± 8.3073	-0.0091 ± 0.0239	-0.0056 ± 0.0152
LB[894-933]	-6.0441 ± 8.8454	-0.0036 ± 0.0205	0.0131 ± 0.0214
LB[980-1015]	-2.8312 ± 8.4453	-0.0112 ± 0.0313	0.0016 ± 0.0163
LB[1070-1120]	-1.1669 ± 2.6411	0.0360 ± 0.0065	0.0030 ± 0.0044
LB[1148-1194]	-3.5702 ± 2.8239	-0.0079 ± 0.0057	-0.0191 ± 0.0058
LB[1246-1290]	-0.5484 ± 2.6527	0.0369 ± 0.0069	0.0001 ± 0.0042
LB[1320-1365]	-4.2333 ± 2.8905	-0.0074 ± 0.0052	-0.0179 ± 0.0057

A.5 Mean width X, Y and Z VS absolute value of nominal separation run 439428

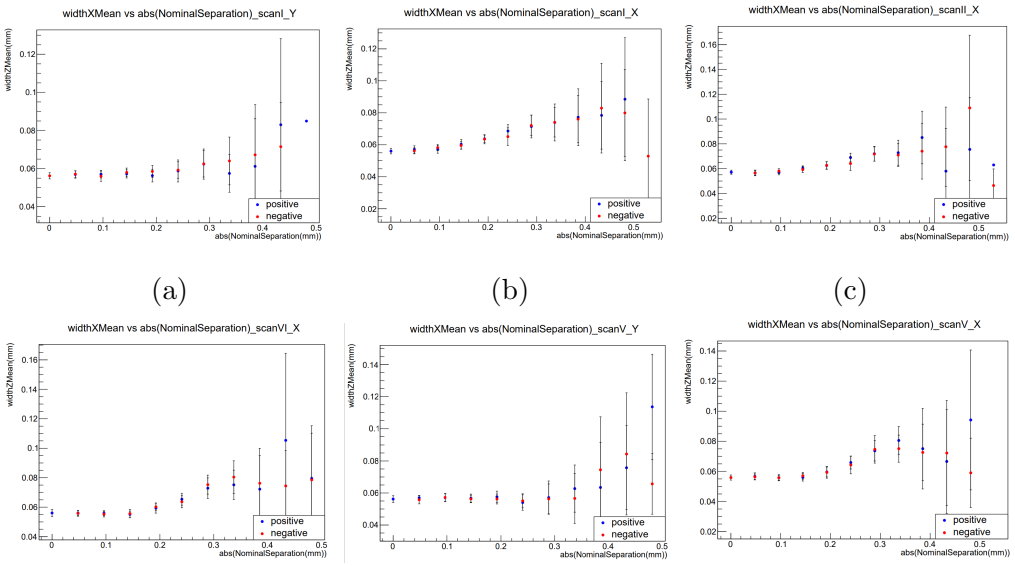

Figure A.7: Mean width X VS absolute value of nominal separation run 439428

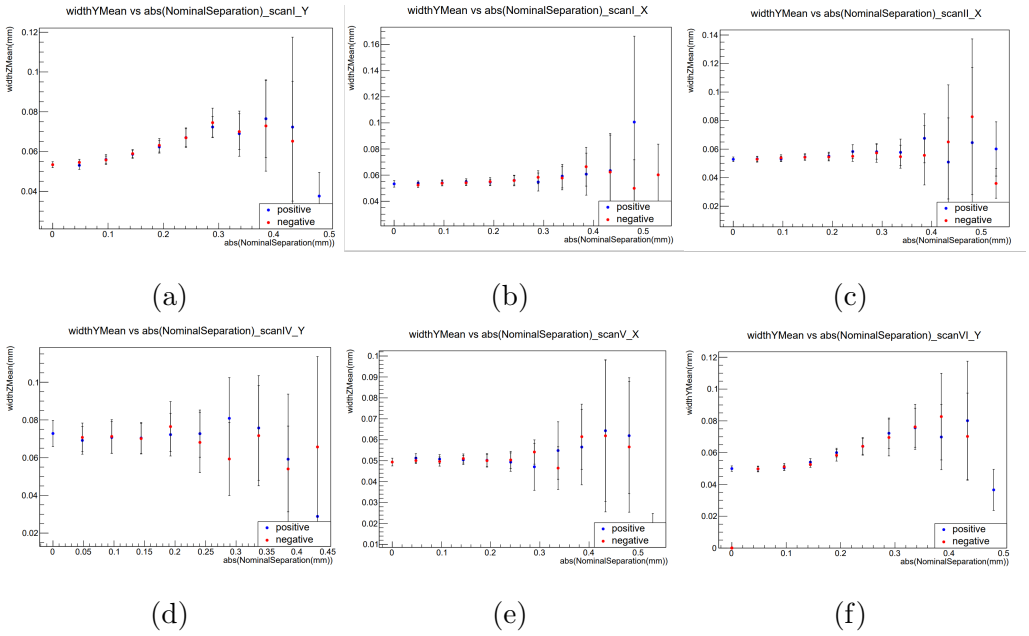

Figure A.8: Mean width Y VS absolute value of nominal separation run 439428

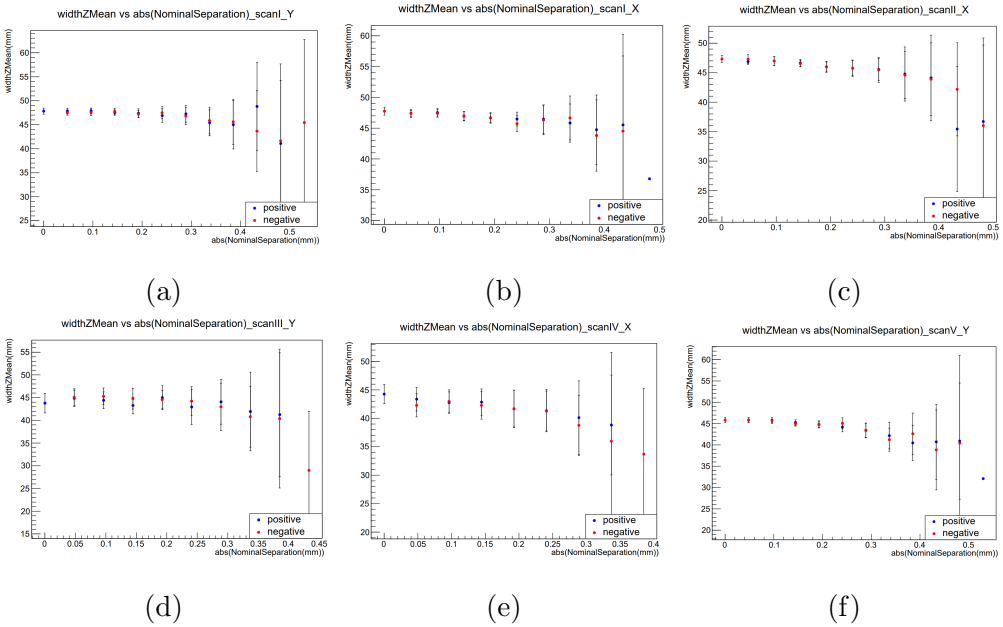

Figure A.9: Mean width Z VS absolute value of nominal separation run 439428

Appendix B

Run 435333

B.1 Fitted slope summary run 435333

scan	posX	posY	posZ
LB[200-232]	-0.0041 ± 0.0148	-0.0196 ± 0.0146	-64.4152 ± 11.0831
LB[235-265]	0.0103 ± 0.0146	0.0095 ± 0.0119	-2.5168 ± 10.1894
LB[445-475]	-0.0042 ± 0.0101	-0.0234 ± 0.0099	-65.3172 ± 7.6672
LB[478-504]	0.0081 ± 0.0109	0.0020 ± 0.0089	-3.4762 ± 7.5146

Appendix C

Run 435229

C.1 The mean position X vs lumi block

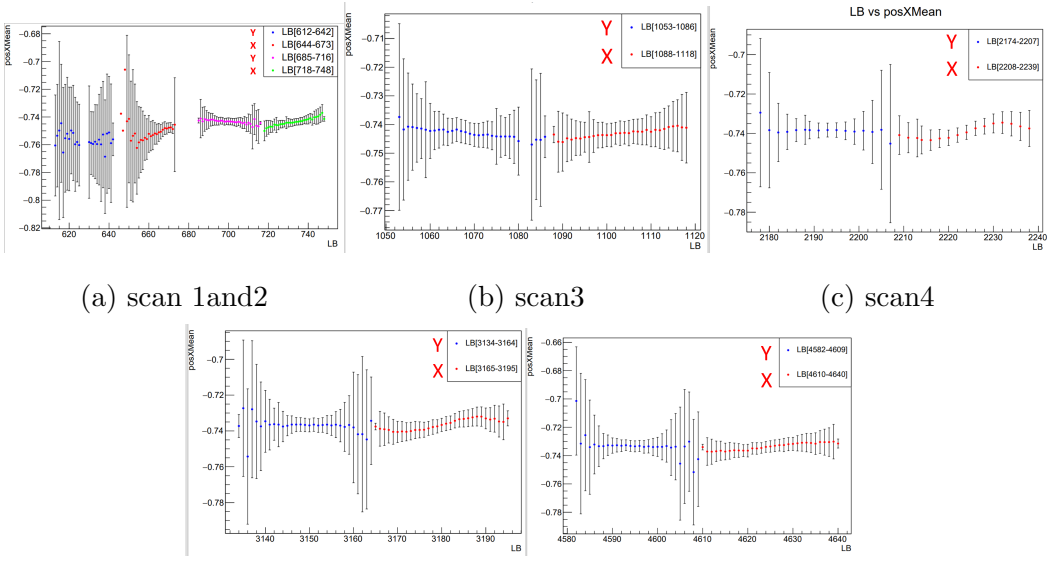

(a) scan 1and2 (b) scan3 (c) scan4

(d) scan5 (e) scan7

Figure C.1: The mean position X vs lumi block- Run 435229

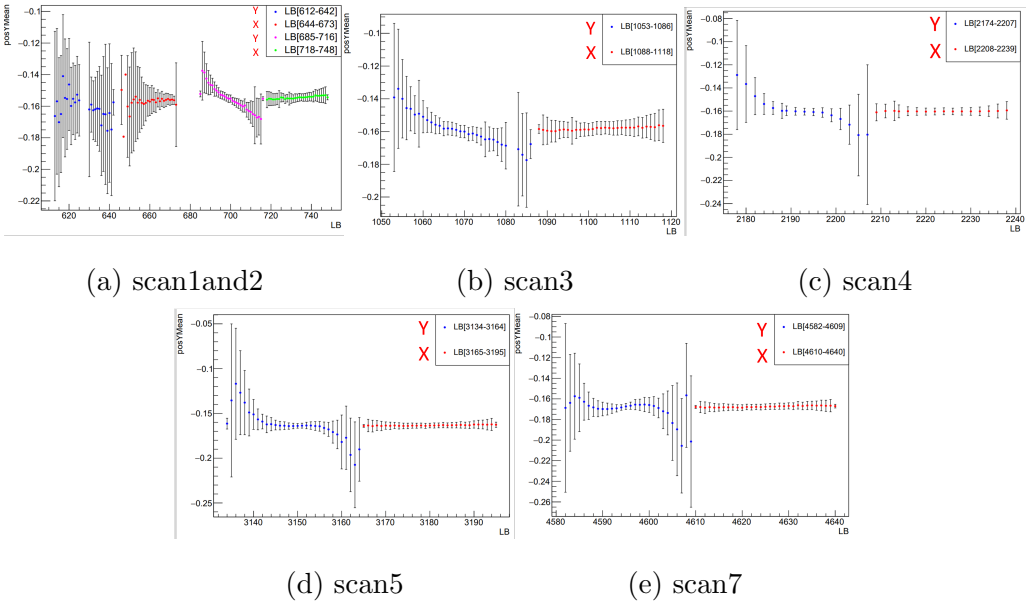

(a) scan1and2 (b) scan3 (c) scan4

(d) scan5 (e) scan7

Figure C.2: The mean position Y vs LB- Run 435229

C.2 The mean position Y vs lumi block

C.3 The mean position Z vs lumi block

C.4 The mean width X vs lumi block- Run 435229

C.5 The mean width Y vs lumi block

C.6 The mean width Z vs lumi block

C.7 Mean width X, Y and Z VS absolute value of nominal separation run 435229

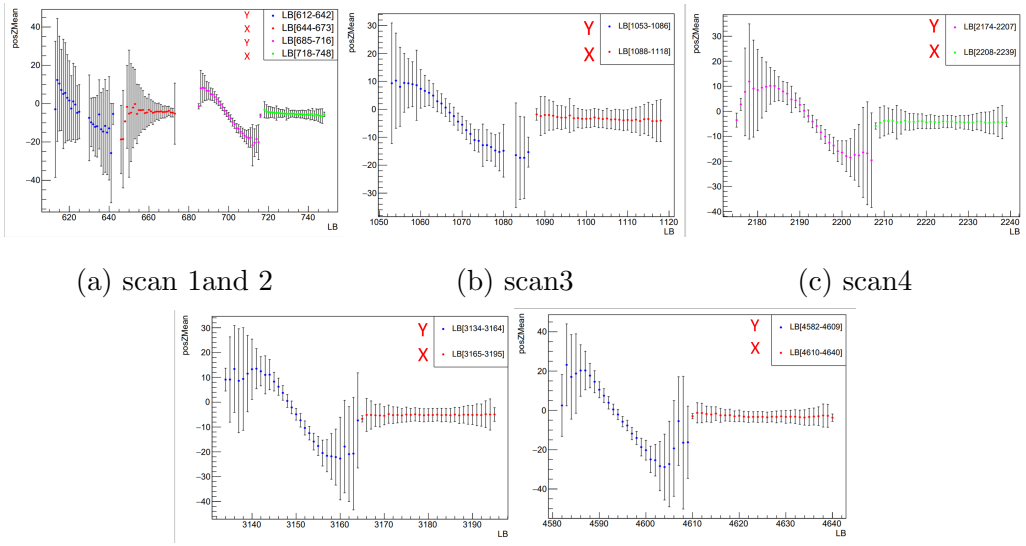

(a) scan 1and 2 (b) scan3 (c) scan4

(d) scan5 (e) scan7

Figure C.3: The mean position Y vs LB- Run 435229

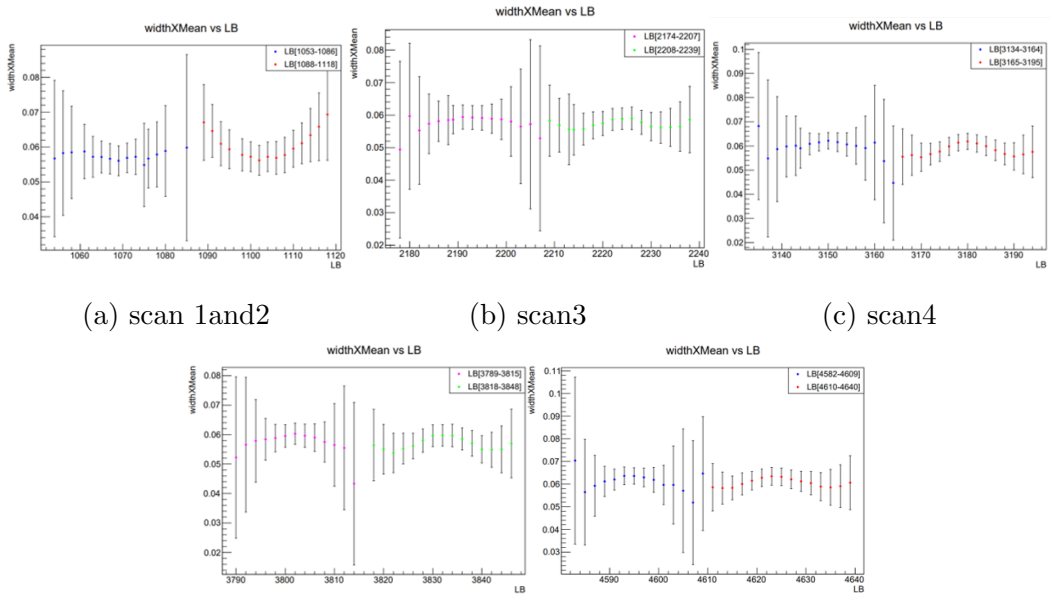

(a) scan 1and2 (b) scan3 (c) scan4

(d) scan5 (e) scan7

Figure C.4: The mean width X vs lumi block -Run 435229

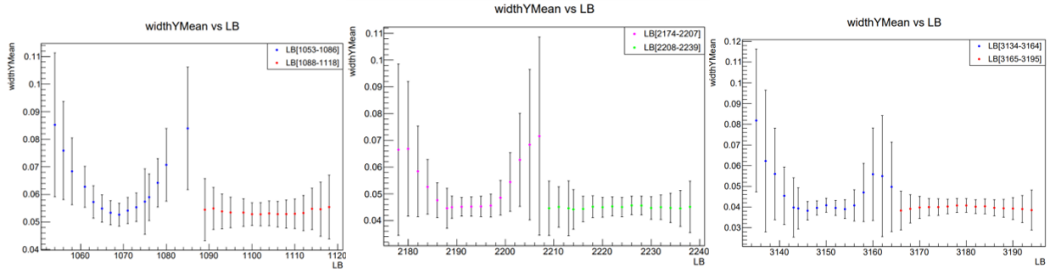

(a) scan1 and 2 (b) scan3 (c) scan4

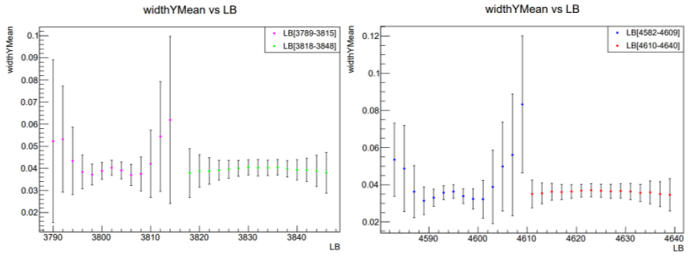

(d) scan5 (e) scan6

Figure C.5: The mean width Y vs lumi block -Run 435229

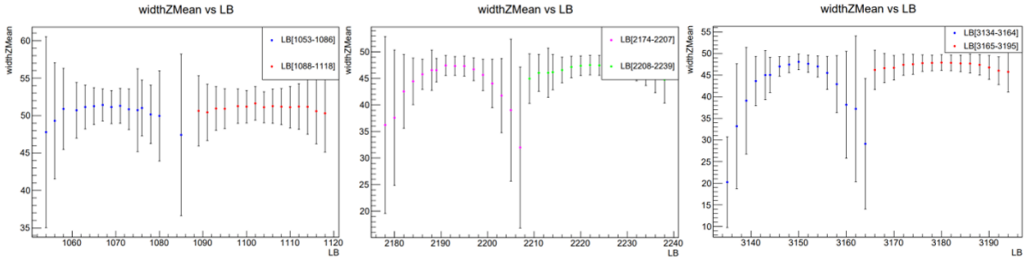

(a) scan1 and2 (b) scan3 (c) scan4

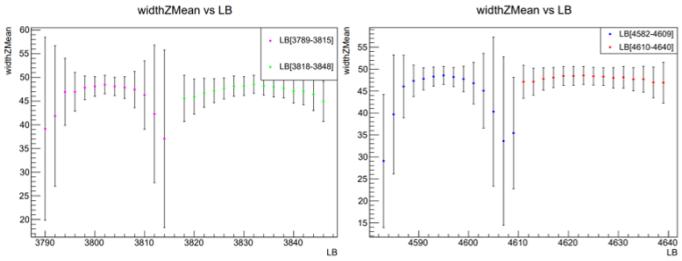

(d) scan5 (e) scan7

Figure C.6: The mean width Z vs lumi block -Run 435229

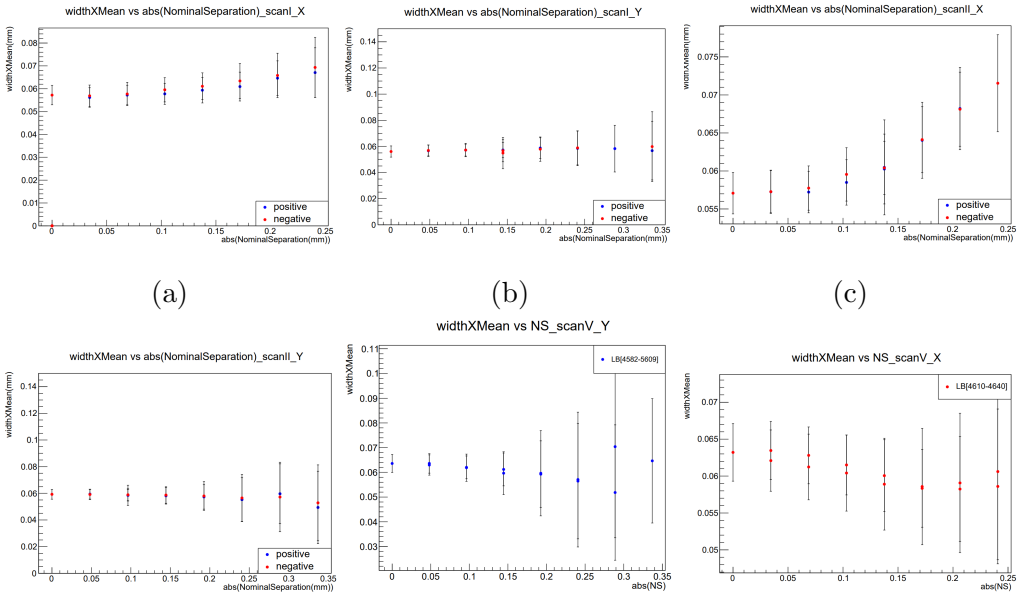

Figure C.7: Mean width X VS absolute value of nominal separation run 435229

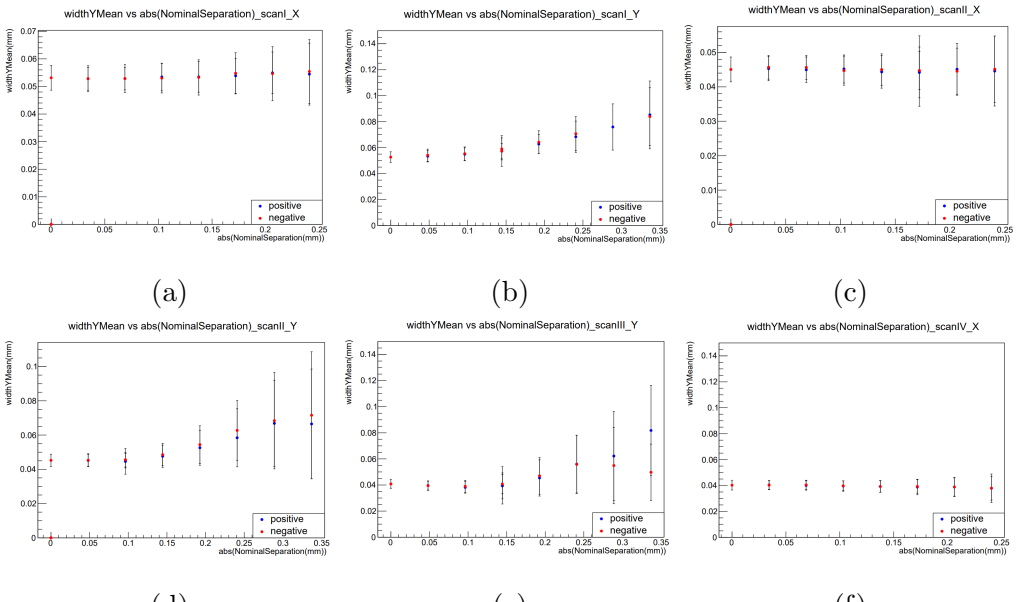

Figure C.8: Mean width Y VS absolute value of nominal separation run 435229

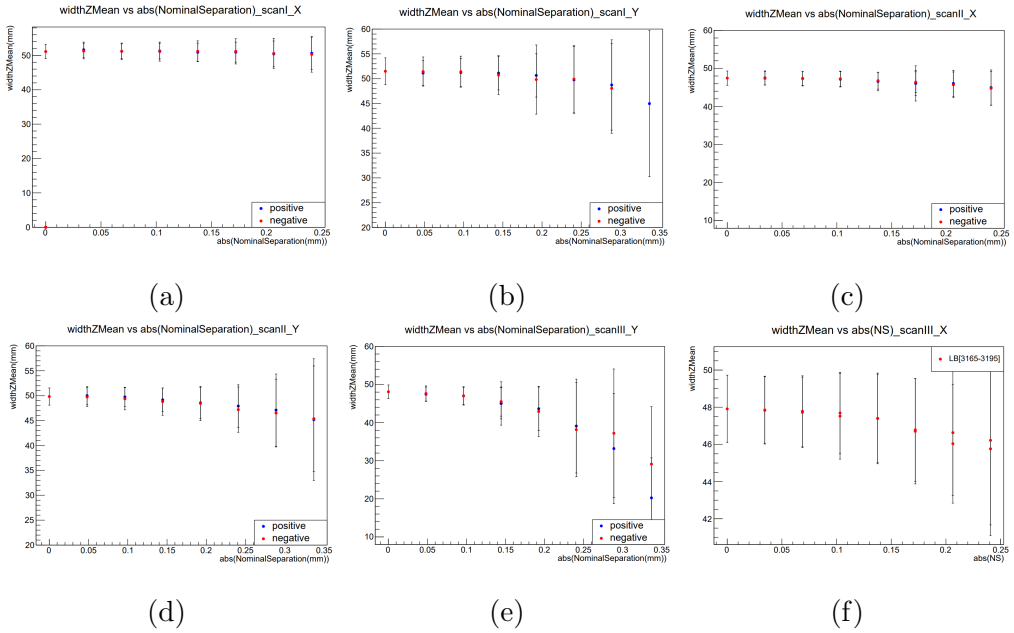

Figure C.9: Mean width Z VS absolute value of nominal separation run 435229

Appendix D

Run 428580

D.1 The mean position X vs lumi block

D.1.0.1 The mean position Y vs luminosity block

D.2 The mean position Z vs luminosity block

D.3 The mean position X, Y and Z vs Nominal separation

D.3.0.1 The mean width X vs luminosity block

D.4 The mean width Y vs luminosity block

D.5 The mean width Z vs lumi block

D.6 Mean width X, Y and Z VS absolute value of nominal separation run 428580

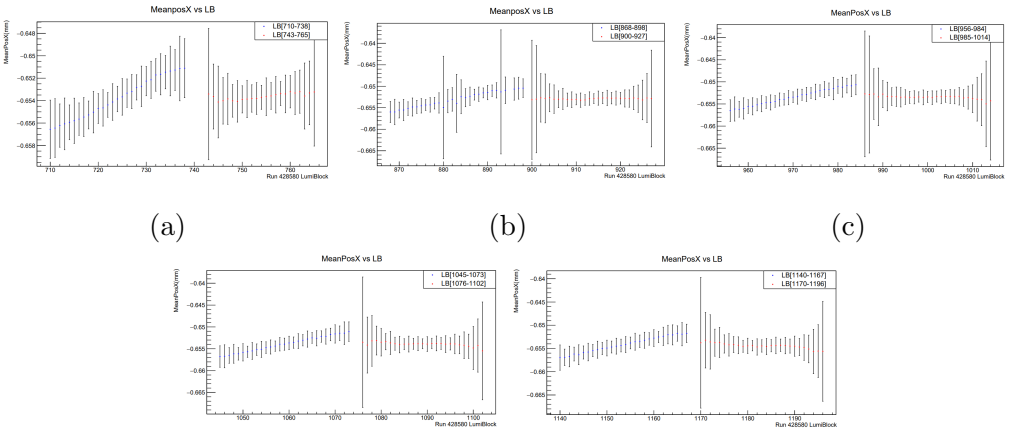

Figure D.1: The mean position X vs luminosity block- Run 428580

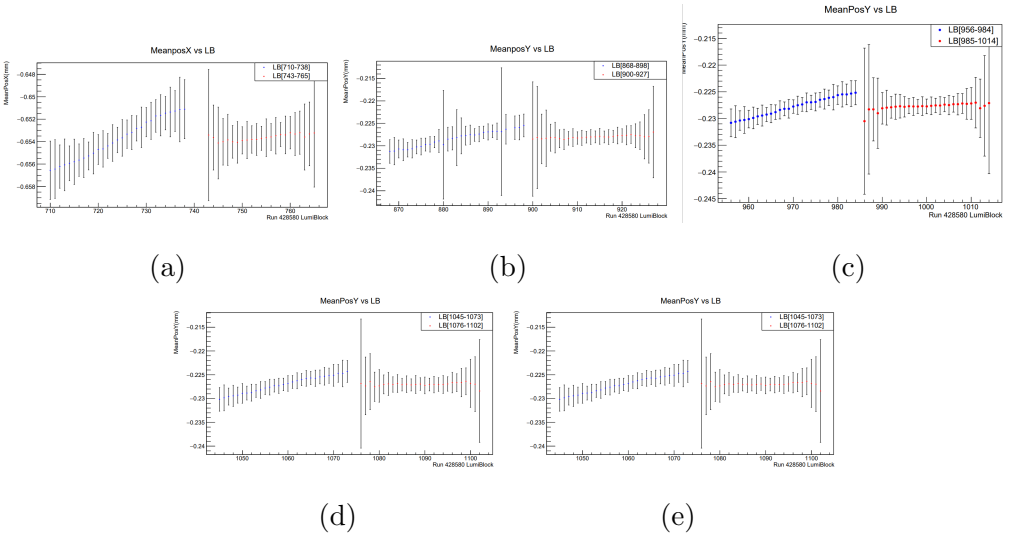

Figure D.2: The mean position Y vs luminosity block- Run 428580

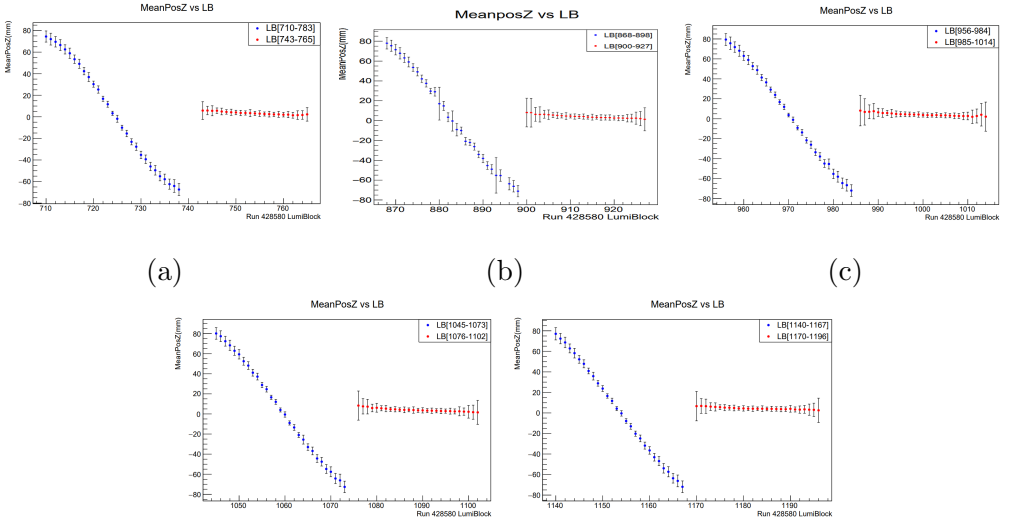

Figure D.3: The mean position Z vs lumi block -Run 428580

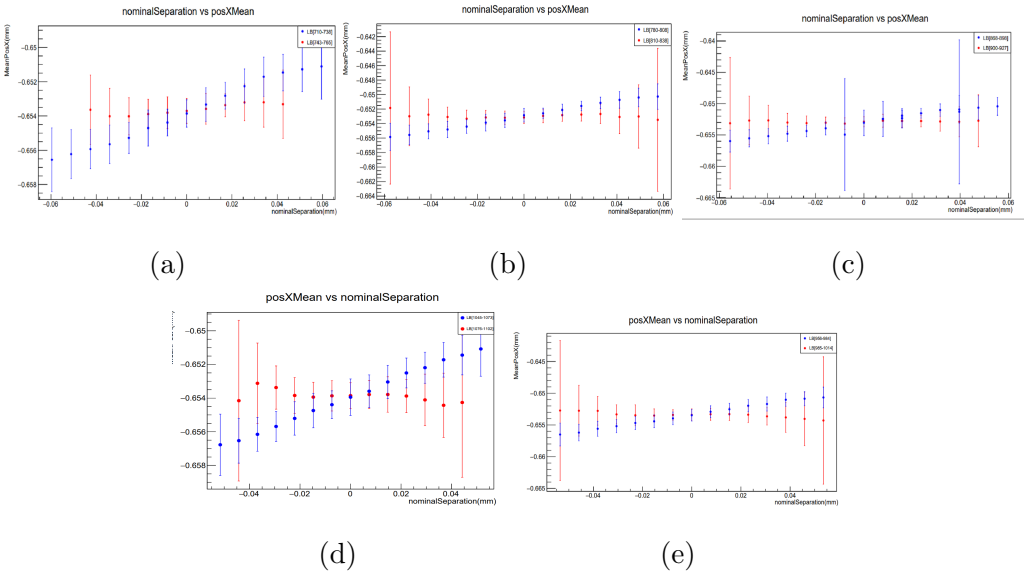

Figure D.4: The mean position X vs Nominal separation -Run 428580

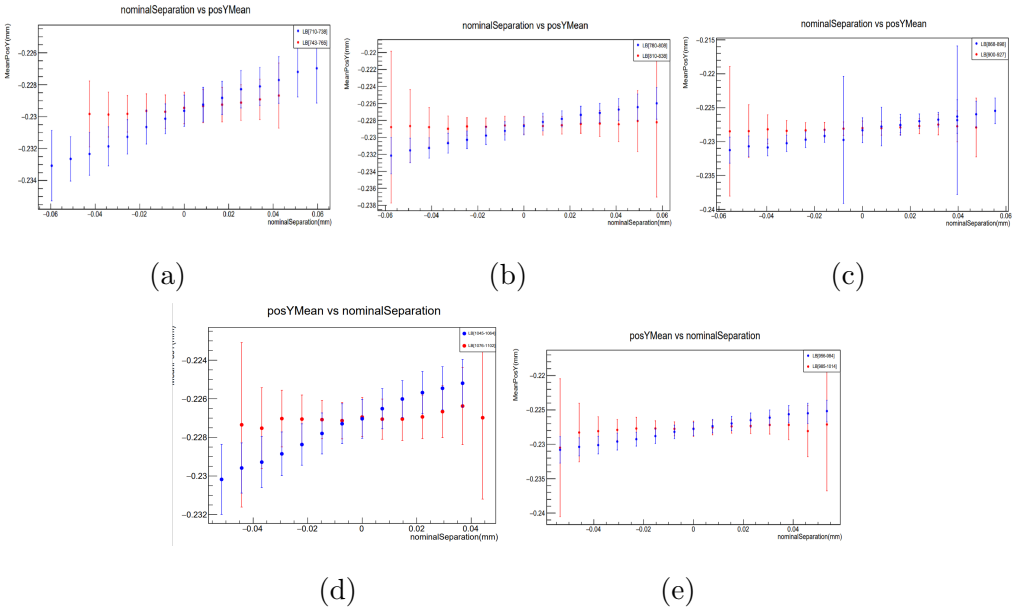

Figure D.5: The mean position Y vs Nominal separation -Run 428580

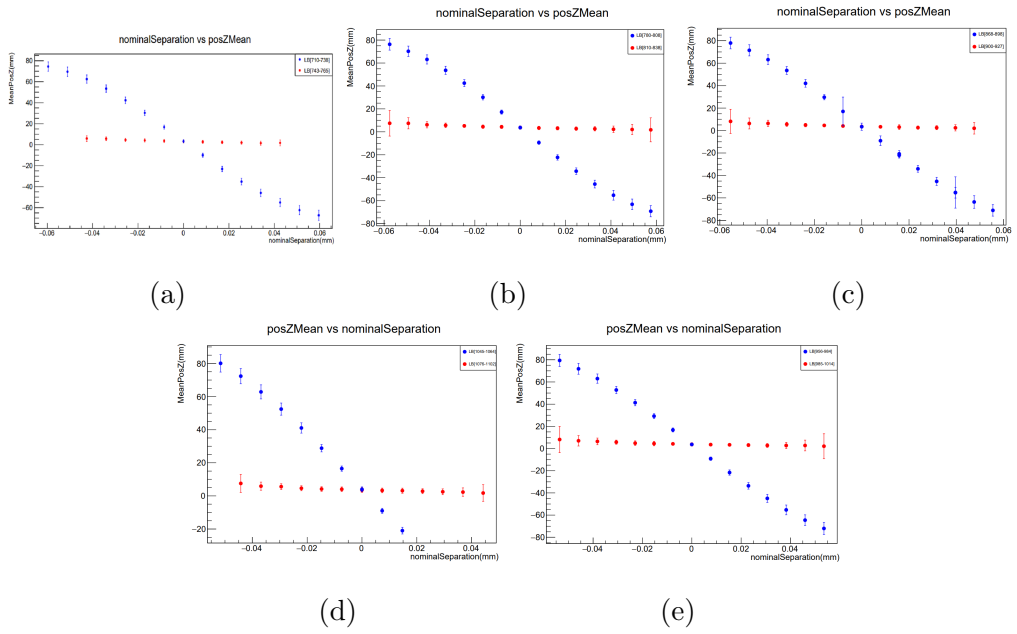

Figure D.6: The mean position Z vs Nominal separation -Run 428580

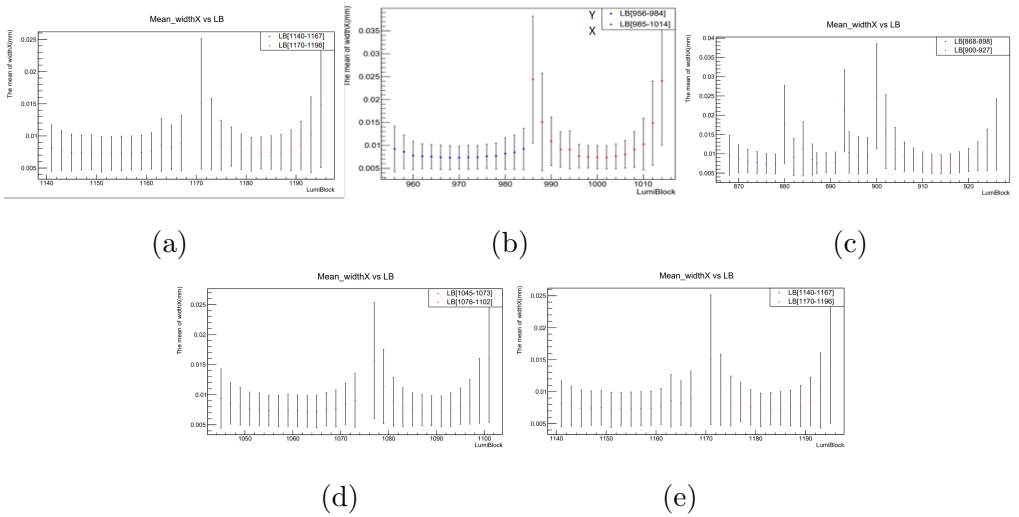

(a) (b) (c)

(d) (e)

Figure D.7: The mean width X vs luminosity block -Run 428580

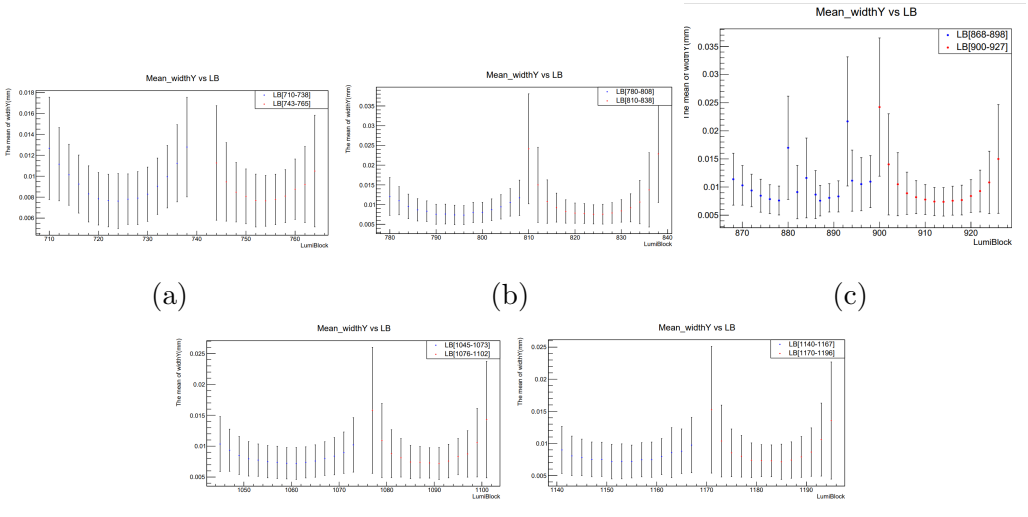

(a) (b) (c)

(d) (e)

Figure D.8: The mean width Y vs lumi block -Run 428580

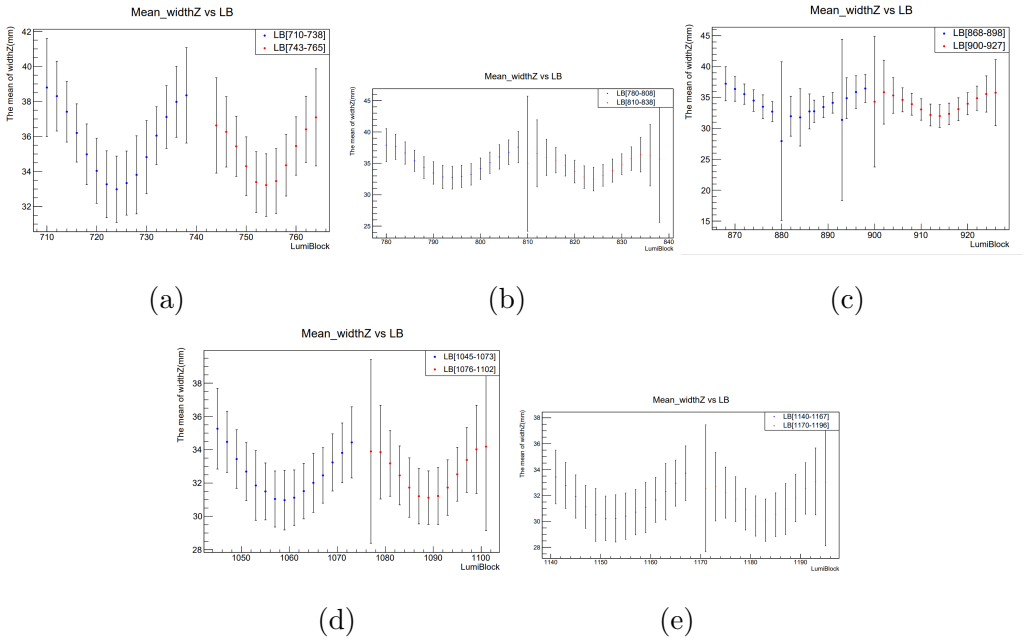

Figure D.9: The mean width Z vs lumi block -Run 428580

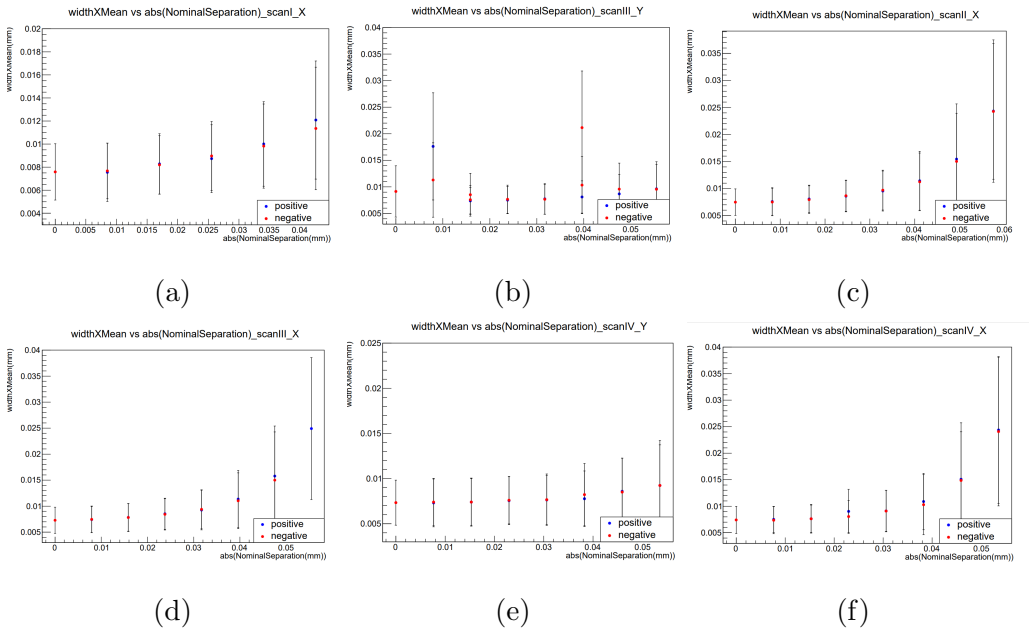

Figure D.10: Mean width X VS absolute value of nominal separation run 428580

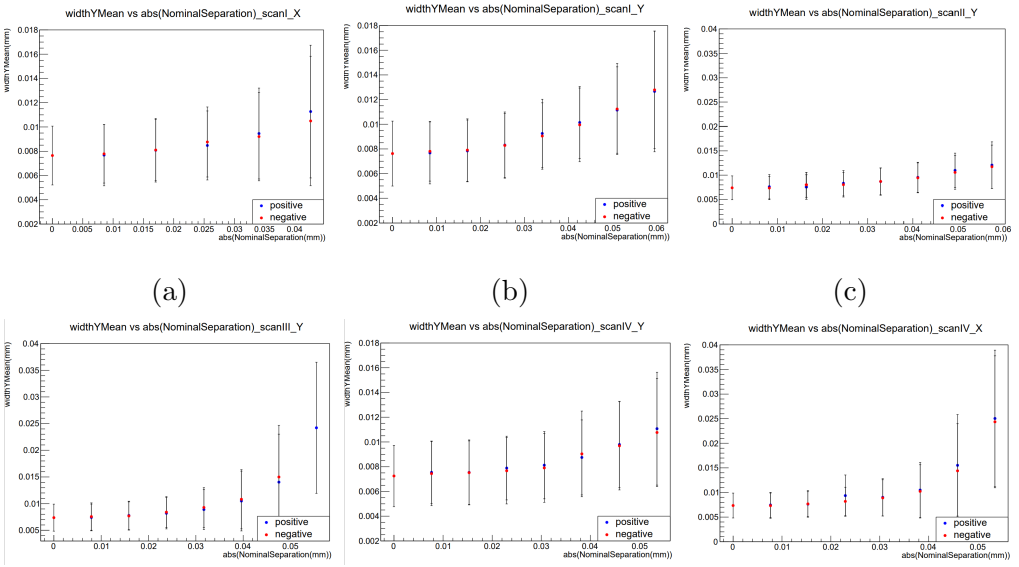

Figure D.11: Mean width Y VS absolute value of nominal separation run 428580

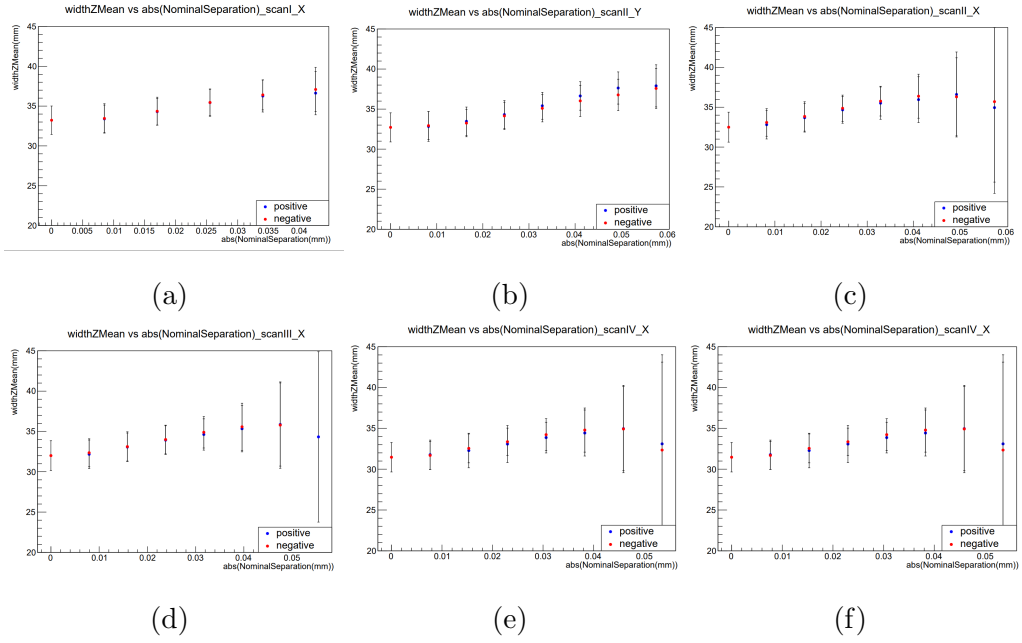

Figure D.12: Mean width Z VS absolute value of nominal separation run 428580

References

[1] Zainab Mohammad K Alsolami, Guennadi Borissov, and Valerie Lang. "A study of beam position and luminosity measurement for Run-3 in ATLAS detector". In: (2024). available for CERN users only. URL: https://cds.cern.ch/record/2886699.

[2] Gabriella Sciolla. "The Mystery of CP violation". In: (2006), pp. 44–50.

[3] André De Gouvêa. "Neutrino Mass Models". In: *Annual Review of Nuclear and Particle Science* 66 (2016), pp. 197–217. ISSN: 01638998. DOI: 10.1146/annurev-nucl-102115-044600.

[4] G. D. Coughlan, J. E. Dodd, and B. M. Gripaios. *The Ideas of Particle Physics: An Introduction for Scientists*. 2006.

[5] Seth Koren. *The Hierarchy Problem: From the Fundamentals to the Frontiers*. 2020. arXiv: 2009.11870 [hep-ph].

[6] Wikimedia Commons. *Standard Model of Elementary Particles Anti*. [Online] Accessed: 28-5-24. URL: https://commons.wikimedia.org/wiki/File:Standard_Model_of_Elementary_Particles_Anti.svg.

[7] Antonio Pich. "Precision tau physics". In: *Progress in Particle and Nuclear Physics* 75 (2014), pp. 41–85. ISSN: 0146-6410. DOI: https://doi.org/10.1016/j.ppnp.2013.11.002.

[8] Workman R. L. et al. "Review of Particle Physics". In: *PTEP* 2022 (2022), p. 083C01. DOI: 10.1093/ptep/ptac097. URL: https://pdg.lbl.gov/2024/reviews/rpp2024-rev-ckm-matrix.pdf.

[9] C. Lazzeroni et al. "Precision measurement of the ratio of the charged kaon leptonic decay rates". In: *Physics Letters B* 719.4 (2013), pp. 326–336. ISSN: 0370-2693. DOI: https://doi.org/10.1016/j.physletb.2013.01.037. URL: https://www.sciencedirect.com/science/article/pii/S0370269313000786.

[10] Vincenzo Cirigliano and Ignasi Rosell. "Two-Loop Effective Theory Analysis of π $(K) \to e\overline{\nu}_e[\gamma]$ Branching Ratios". In: *Phys. Rev. Lett.* 99 (23 Dec. 2007), p. 231801. DOI: 10.1103/PhysRevLett.99.231801. URL: https://link.aps.org/doi/10.1103/PhysRevLett.99.231801.

[11] Aguilar-Arevalo et al. "Improved measurement of the $\pi \to e\nu$ branching ratio". In: (2015). arXiv: 1506.05845v2.

[12] Y. Amhis et al. (Heavy Flavor Averaging Group). *Average of R(D) and $R(D^*)$*. URL: https://hflav-eos.web.cern.ch/hflav-eos/semi/spring21/html/RDsDsstar/RDRDs.html (visited on 05/18/2022).

[13] Aulchenko V. M. et al.(KEDR Collaboration). "Measurement of the ratio of the leptonic widths $\Gamma_{ee}/\Gamma_{\mu\mu}$ for the J/ψ meson". In: (2013), pp. 1–5. DOI: 10.1016/j.physletb.2014.02.046. arXiv: 1311.5005. URL: http://arxiv.org/abs/1311.5005%0Ahttp://dx.doi.org/10.1016/j.physletb.2014.02.046.

[14] Workman R. L. et al. "Review of Particle Physics". In: *PTEP* 2022 (2022), p. 083C01. DOI: 10.1093/ptep/ptac097.

[15] Schael S. et al. "Electroweak measurements in electron-positron collisions at W-boson-pair energies at LEP". In: *Physics Reports* 532.4 (2013), pp. 119–244. DOI: 10.1016/j.physrep.2013.07.004. URL: http://dx.doi.org/10.1016/j.physrep.2013.07.004.

[16] The LHCb Collaboration. "Measurement of forward W $\to e\nu$ production in pp collisions at$sqrts = 8$ TeV". In: (2016). DOI: 10.1007/JHEP10(2016)030.

[17] Armen Tumasyan et al. "Precision measurement of the W boson decay branching fractions in proton-proton collisions at $\sqrt{s} = 13$ TeV". In: *Phys. Rev. D* 105.7 (2022), p. 072008. DOI: 10.1103/PhysRevD.105.072008. arXiv: 2201.07861.

[18] Morad Aaboud et al. "Precision measurement and interpretation of inclusive W^+ , W^- and Z/γ^* production cross sections with the ATLAS detector". In: *Eur. Phys. J. C* 77.6 (2017), p. 367. DOI: 10.1140/epjc/s10052-017-4911-9. arXiv: 1612.03016 [hep-ex]. URL: https://pdglive.lbl.gov/BranchingRatio.action?pdgid=S043.2&home=.

[19] Tony M. Liss and Paul L. Tipton. "The Discovery of the Top Quark". In: *Scientific American* 277.3 (1997), pp. 54–59. ISSN: 0036-8733. DOI: 10.1038/scientificamerican0997-54.

[20] Geoffrey (on behalf of the ATLAS Gilles and CMS collaborations). "Top-quark production at the LHC". In: *La Thuile Physics Workshop*. La Thuile, Aosta Valley (Italy), Mar. 2018. URL: https://cds.cern.ch/record/2314658/files/ATL-PHYS-SLIDE-2018-190.pdf.

[21] S. Navas et al. "Review of particle physics". In: *Phys. Rev. D* 110.3 (2024), p. 030001. DOI: 10.1103/PhysRevD.110.030001.

[22] Lyndon Evans and Philip Bryant. "LHC Machine". In: *Journal of Instrumentation* 3.8 (2008). ISSN: 17480221. DOI: 10.1088/1748-0221/3/08/S08001.

[23] Genessis Perez. "Unitarization Models For Vector Boson Scattering at the LHC". PhD thesis. Jan. 2018. DOI: 10.5445/IR/1000082199.

[24] "The Expected Performance of the ATLAS Inner Detector". In: (2008). URL: https://inspirehep.net/literature/1795269.

[25] P Puzo. "ATLAS calorimetry". In: *Nuclear Instruments and Methods in Physics Research Section A: Accelerators, Spectrometers, Detectors and Associated Equipment* 494.1 (2002), pp. 340–345. ISSN: 0168-9002. DOI:

https://doi.org/10.1016/S0168-9002(02)01490-0. URL: https://www.sciencedirect.com/science/article/pii/S0168900202014900.

[26] Adams D. L. et al. *Muon Reconstruction and Identification Performance in ATLAS: Studies with Simulated Monte Carlo Samples*. Tech. rep. Geneva: CERN, 2009. URL: https://cds.cern.ch/record/1169053/files/ATL-PHYS-PUB-2009-008.pdf.

[27] *The Trigger for Early Running*. Tech. rep. CERN, 2009. URL: https://cds.cern.ch/record/1167692/files/ATL-PHYS-PUB-2009-025.pdf.

[28] Paola Miele and Herman H.J ten Kate. "The superconducting magnet system for the ATLAS detector at CERN". In: *Fusion Engineering and Design* 58-59 (2001), pp. 195–203. ISSN: 0920-3796. DOI: https://doi.org/10.1016/S0920-3796(01)00432-X. URL: https://www.sciencedirect.com/science/article/pii/S092037960100432X.

[29] Cristiano Alpigiani et al. "Luminosity measurement based on inner detector tracks in ATLAS in Run 2". In: January (2022).

[30] ATLAS Collaboration. "Luminosity determination in pp collisions at $\sqrt{s} = 13$ TeV using the ATLAS detector at the LHC". In: December (2022). arXiv: 2212.09379. URL: http://arxiv.org/abs/2212.09379.

[31] Michael Böhler et al. "Evolution of ATLAS conditions data and its management for LHC Run-2". In: *Journal of Physics: Conference Series* 664.4 (2015), p. 042005. DOI: 10.1088/1742-6596/664/4/042005. URL: https://dx.doi.org/10.1088/1742-6596/664/4/042005.

[32] Aad Georges et al. *Electron and photon efficiencies in LHC Run 2 with the ATLAS experiment*. Tech. rep. Geneva: CERN, 2023. arXiv: 2308.13362. URL: https://cds.cern.ch/record/2868520.

[33] Aaboud M. et al. (ATLAS Collaboration). "Electron reconstruction and identification in the ATLAS experiment using the 2015 and 2016 LHC

proton–proton collision data at $\sqrt{s} = 13$ TeV". In: *Eur. Phys. J. C* 79 (2019). DOI: 10.1140/epjc/s10052-019-7140-6.

[34] Aaboud M. et al. "Measurement of the photon identification efficiencies with the ATLAS detector using LHC Run 2 data collected in 2015 and 2016". In: *The European Physical Journal C* 79.3 (2019). ISSN: 1434-6052. DOI: 10.1140/epjc/s10052-019-6650-6. URL: http://dx.doi.org/10.1140/epjc/s10052-019-6650-6.

[35] Aad G. et al. "Jet energy scale and resolution measured in proton–proton collisions at $\sqrt{s} = 13$ TeV with the ATLAS detector". In: *The European Physical Journal C* 81.8 (2021). ISSN: 1434-6052. DOI: 10.1140/epjc/s10052-021-09402-3. URL: http://dx.doi.org/10.1140/epjc/s10052-021-09402-3.

[36] D. Vannicola. "MUON RECONSTRUCTION AND IDENTIFICATION IN THE ATLAS EXPERIMENT AT LHC". In: *Frascati Physics Series* 67 (2018). URL: https://cds.cern.ch/record/2677374/files/1730237_94-98.pdf.

[37] Xabier Cid Vidal. *Taking a closer look at LHC - Detectors*. May 30, 2024. URL: https://www.lhc-closer.es/taking_a_closer_look_at_lhc/1.detectors.

[38] Stefan Höche. "Introduction to parton-shower event generators". In: (2015). arXiv: 1411.4085 [hep-ph].

[39] Torbjorn Sjostrand, Stephen Mrenna, and Peter Z. Skands. "A Brief Introduction to PYTHIA 8.1". In: *Computer Physics Communications* 178.12 (2008), pp. 852–867. DOI: 10.1016/j.cpc.2008.01.036.

[40] René Brun et al. "GEANT: Detector Description and Simulation Tool; Oct1994". In: CERN Program Library (1993). Long Writeup W5013. DOI: 10.17181/CERN.MUHF.DMJ1. URL: https://cds.cern.ch/record/1082634.

[41] Bahr M. et al. "Herwig++ Physics and Manual". In: *Eur. Phys. J. C* 58 (2008), pp. 639–707.

[42] Enrico Bothmann et al. "Event generation with Sherpa 2.2". In: *SciPost Phys.* 7 (2019), p. 034. DOI: 10.21468/SciPostPhys.7.3.034. URL: https://scipost.org/10.21468/SciPostPhys.7.3.034.

[43] J. Alwall et al. "The automated computation of tree-level and next-to-leading order differential cross sections, and their matching to parton shower simulations". In: *Journal of High Energy Physics* 2014.7 (2014). ISSN: 1029-8479. DOI: 10.1007/jhep07(2014)079. URL: http://dx.doi.org/10.1007/JHEP07(2014)079.

[44] Torbjörn Sjöstrand, Stephen Mrenna, and Peter Skands. "A brief introduction to PYTHIA 8.1". In: *Computer Physics Communications* 178.11 (June 2008), pp. 852–867. ISSN: 0010-4655. DOI: 10.1016/j.cpc.2008.01.036. URL: http://dx.doi.org/10.1016/j.cpc.2008.01.036.

[45] Stefano Frixione, Paolo Nason, and Carlo Oleari. "Matching NLO QCD computations with parton shower simulations: the POWHEG method". In: *Journal of High Energy Physics* 2007.11 (Nov. 2007), p. 070. DOI: 10.1088/1126-6708/2007/11/070. URL: https://dx.doi.org/10.1088/1126-6708/2007/11/070.

[46] David J. Lange. "The EvtGen particle decay simulation package". In: *Nuclear Instruments and Methods in Physics Research Section A: Accelerators, Spectrometers, Detectors and Associated Equipment* 462.1 (2001), pp. 152–155. ISSN: 0168-9002. DOI: https://doi.org/10.1016/S0168-9002(01)00089-4. URL: https://www.sciencedirect.com/science/article/pii/S0168900201000894.

[47] L. Evans. *The Large Hadron Collider: A marvel of technology.* 2008, 32(1), 37–40.

[48] The ATLAS Collaboration. "An analytical determination of the parameters of the single-Gaussian model of bunch densities and their impact on the luminosity calibration by the van der Meer method". In: (2010). available only for CERN users. URL: https://cds.cern.ch/record/1523278.

[49] The ATLAS Collaboration. "Performance of primary vertex reconstruction in proton-proton collisions at TeV in the ATLAS experiment". In: (2010).

[50] Juerg Beringer et al. "Offline beam spot reconstruction in ATLAS during Run 1 ". In: (2015). available for CERN users only. URL: https://cds.cern.ch/record/1978679.

[51] The ATLAS Collaboration. *ATLAS DATA SUMMARY*. available for CERN users only. 2022. URL: https://atlas-datasummary.web.cern.ch/2022/runsum.py?style=ALL.

[52] The ATLAS Collaboration. *ATLAS data summary*. available for CERN users only. 2022. URL: https://atlas-datasummary.web.cern.ch/2022/run.py?run=428580.

[53] The ATLAS Collaboration. "An analytical determination of the parameters of the single-Gaussian model of bunch densities and their impact on the luminosity calibration by the van der Meer method". In: (2013), pp. 0–33.

[54] Guennadi Borissov and Emma Marshall. "Test of Lepton Flavour Universality in the decays of top quark to τ lepton or electron". In: (2023). available for CERN users only. URL: https://cds.cern.ch/record/2857873.

[55] ATLAS Collaboration. *ATLAS Publication Committee Home Page*. 2020. URL: https://twiki.cern.ch/twiki/bin/view/AtlasProtected/PubComHome.

[56] Stefano Frixione, Giovanni Ridolfi, and Paolo Nason. "A positive-weight next-to-leading-order Monte Carlo for heavy flavour hadroproduction". In: *JHEP* 09 (2007), p. 126. DOI: 10.1088/1126-6708/2007/09/126. arXiv: 0707.3088 [hep-ph].

[57] Paolo Nason. "A new method for combining NLO QCD with shower Monte Carlo algorithms". In: *JHEP* 11 (2004), p. 040. DOI: 10.1088/1126-6708/2004/11/040. arXiv: hep-ph/0409146.

[58] Stefano Frixione, Paolo Nason, and Carlo Oleari. "Matching NLO QCD computations with parton shower simulations: the POWHEG method". In: *JHEP* 11 (2007), p. 070. DOI: 10.1088/1126-6708/2007/11/070. arXiv: 0709.2092 [hep-ph].

[59] Simone Alioli et al. "A general framework for implementing NLO calculations in shower Monte Carlo programs: the POWHEG BOX". In: *JHEP* 06 (2010), p. 043. DOI: 10.1007/JHEP06(2010)043. arXiv: 1002.2581 [hep-ph].

[60] The NNPDF Collaboration, Richard D. Ball, et al. "Parton distributions for the LHC run II". In: *JHEP* 04 (2015), p. 040. DOI: 10.1007/JHEP04(2015)040. arXiv: 1410.8849 [hep-ph].

[61] ATLAS Collaboration. *Studies on top-quark Monte Carlo modelling for Top2016*. ATL-PHYS-PUB-2016-020. (available for Cern members only). 2016. URL: https://cds.cern.ch/record/2216168.

[62] Torbjörn Sjöstrand et al. "An introduction to PYTHIA 8.2". In: *Comput. Phys. Commun.* 191 (2015), p. 159. DOI: 10.1016/j.cpc.2015.01.024. arXiv: 1410.3012 [hep-ph].

[63] ATLAS Collaboration. *ATLAS Pythia 8 tunes to 7 TeV data*. ATL-PHYS-PUB-2014-021. 2014. URL: https://cds.cern.ch/record/1966419.

[64] NNPDF Collaboration, Richard D. Ball, et al. "Parton distributions with LHC data". In: *Nucl. Phys. B* 867 (2013), p. 244. DOI: 10.1016/j.nuclphysb.2012.10.003. arXiv: 1207.1303 [hep-ph].

[65] D. J. Lange. "The EvtGen particle decay simulation package". In: *Nucl. Instrum. Meth. A* 462 (2001), p. 152. DOI: 10.1016/S0168-9002(01)00089-4.

[66] M. Beneke et al. "Hadronic top-quark pair production with NNLL threshold resummation". In: *Nucl. Phys. B* 855 (2012), pp. 695–741. DOI: 10.1016/j.nuclphysb.2011.10.021. arXiv: 1109.1536 [hep-ph].

[67] Matteo Cacciari et al. "Top-pair production at hadron colliders with next-to-next-to-leading logarithmic soft-gluon resummation". In: *Phys. Lett. B* 710 (2012), pp. 612–622. DOI: 10.1016/j.physletb.2012.03.013. arXiv: 1111.5869 [hep-ph].

[68] Peter Bärnreuther, Michal Czakon, and Alexander Mitov. "Percent-Level-Precision Physics at the Tevatron: Next-to-Next-to-Leading Order QCD Corrections to $q\bar{q} \to t\bar{t} + X$". In: *Phys. Rev. Lett.* 109 (2012), p. 132001. DOI: 10.1103/PhysRevLett.109.132001. arXiv: 1204.5201 [hep-ph].

[69] Michal Czakon and Alexander Mitov. "NNLO corrections to top-pair production at hadron colliders: the all-fermionic scattering channels". In: *JHEP* 12 (2012), p. 054. DOI: 10.1007/JHEP12(2012)054. arXiv: 1207.0236 [hep-ph].

[70] Michal Czakon and Alexander Mitov. "NNLO corrections to top pair production at hadron colliders: the quark-gluon reaction". In: *JHEP* 01 (2013), p. 080. DOI: 10.1007/JHEP01(2013)080. arXiv: 1210.6832 [hep-ph].

[71] Michal Czakon, Paul Fiedler, and Alexander Mitov. "Total Top-Quark Pair-Production Cross Section at Hadron Colliders Through $O(\alpha_S^4)$". In: *Phys. Rev. Lett.* 110 (2013), p. 252004. DOI: 10.1103/PhysRevLett.110.252004. arXiv: 1303.6254 [hep-ph].

[72] Michal Czakon and Alexander Mitov. "Top++: A program for the calculation of the top-pair cross-section at hadron colliders". In: *Comput. Phys. Commun.* 185 (2014), p. 2930. DOI: 10.1016/j.cpc.2014.06.021. arXiv: 1112.5675 [hep-ph].

[73] Jon Butterworth et al. "PDF4LHC recommendations for LHC Run II". In: *J. Phys. G* 43 (2016), p. 023001. DOI: 10.1088/0954-3899/43/2/023001. arXiv: 1510.03865 [hep-ph].

[74] A. D. Martin et al. "Parton distributions for the LHC". In: *Eur. Phys. J. C* 63 (2009), p. 189. DOI: 10.1140/epjc/s10052-009-1072-5. arXiv: 0901.0002 [hep-ph].

[75] A. D. Martin et al. "Uncertainties on α_S in global PDF analyses and implications for predicted hadronic cross sections". In: *Eur. Phys. J. C* 64 (2009), pp. 653–680. DOI: 10.1140/epjc/s10052-009-1164-2. arXiv: 0905.3531 [hep-ph].

[76] H.-L. Lai et al. "New parton distributions for collider physics". In: *Phys. Rev. D* 82 (2010), p. 074024. DOI: 10.1103/PhysRevD.82.074024. arXiv: 1007.2241 [hep-ph].

[77] J. Gao et al. "CT10 next-to-next-to-leading order global analysis of QCD". In: *Phys. Rev. D* 89 (2014), p. 033009. DOI: 10.1103/PhysRevD.89.033009. arXiv: 1302.6246 [hep-ph].

[78] Emanuele Re. "Single-top Wt-channel production matched with parton showers using the POWHEG method". In: *Eur. Phys. J. C* 71 (2011), p. 1547. DOI: 10.1140/epjc/s10052-011-1547-z. arXiv: 1009.2450 [hep-ph].

[79] Stefano Frixione et al. "Single-top hadroproduction in association with a W boson". In: *JHEP* 07 (2008), p. 029. DOI: 10.1088/1126-6708/2008/07/029. arXiv: 0805.3067 [hep-ph].

[80] J. Alwall et al. "The automated computation of tree-level and next-to-leading order differential cross sections, and their matching to parton shower simulations". In: *JHEP* 07 (2014), p. 079. DOI: 10.1007/JHEP07(2014)079. arXiv: 1405.0301 [hep-ph].

[81] Heribertus B. Hartanto et al. "Higgs boson production in association with top quarks in the POWHEG BOX". In: *Phys. Rev. D* 91.9 (2015), p. 094003. DOI: 10.1103/PhysRevD.91.094003. arXiv: 1501.04498 [hep-ph].

[82] Enrico Bothmann et al. "Event generation with Sherpa 2.2". In: *SciPost Phys.* 7.3 (2019), p. 034. DOI: 10.21468/SciPostPhys.7.3.034. arXiv: 1905.09127 [hep-ph].

[83] Tanju Gleisberg and Stefan Höche. "Comix, a new matrix element generator". In: *JHEP* 12 (2008), p. 039. DOI: 10.1088/1126-6708/2008/12/039. arXiv: 0808.3674 [hep-ph].

[84] Federico Buccioni et al. "OpenLoops 2". In: *Eur. Phys. J. C* 79.10 (2019), p. 866. DOI: 10.1140/epjc/s10052-019-7306-2. arXiv: 1907.13071 [hep-ph].

[85] Fabio Cascioli, Philipp Maierhöfer, and Stefano Pozzorini. "Scattering Amplitudes with Open Loops". In: *Phys. Rev. Lett.* 108 (2012), p. 111601. DOI: 10.1103/PhysRevLett.108.111601. arXiv: 1111.5206 [hep-ph].

[86] Ansgar Denner, Stefan Dittmaier, and Lars Hofer. "COLLIER: A fortran-based complex one-loop library in extended regularizations". In: *Comput. Phys. Commun.* 212 (2017), pp. 220–238. DOI: 10.1016/j.cpc.2016.10.013. arXiv: 1604.06792 [hep-ph].

[87] Steffen Schumann and Frank Krauss. "A parton shower algorithm based on Catani–Seymour dipole factorisation". In: *JHEP* 03 (2008), p. 038. DOI: 10.1088/1126-6708/2008/03/038. arXiv: 0709.1027 [hep-ph].

[88] Stefan Höche et al. "A critical appraisal of NLO+PS matching methods". In: *JHEP* 09 (2012), p. 049. DOI: 10.1007/JHEP09(2012)049. arXiv: 1111.1220 [hep-ph].

[89] Stefan Höche et al. "QCD matrix elements + parton showers. The NLO case". In: *JHEP* 04 (2013), p. 027. DOI: 10.1007/JHEP04(2013)027. arXiv: 1207.5030 [hep-ph].

[90] S. Catani et al. "QCD Matrix Elements + Parton Showers". In: *JHEP* 11 (2001), p. 063. DOI: 10.1088/1126-6708/2001/11/063. arXiv: hep-ph/0109231.

[91] Stefan Höche et al. "QCD matrix elements and truncated showers". In: *JHEP* 05 (2009), p. 053. DOI: 10.1088/1126-6708/2009/05/053. arXiv: 0903.1219 [hep-ph].

[92] Charalampos Anastasiou et al. "High-precision QCD at hadron colliders: Electroweak gauge boson rapidity distributions at next-to-next-to leading order". In: *Phys. Rev. D* 69 (2004), p. 094008. DOI: 10.1103/PhysRevD.69.094008. arXiv: hep-ph/0312266.

[93] Rikkert Frederix, Emanuele Re, and Paolo Torrielli. "Single-top t-channel hadroproduction in the four-flavour scheme with POWHEG and aMC@NLO". In: *JHEP* 09 (2012), p. 130. DOI: 10.1007/JHEP09(2012)130. arXiv: 1207.5391 [hep-ph].

[94] Simone Alioli et al. "NLO single-top production matched with shower in POWHEG: s- and t-channel contributions". In: *JHEP* 09 (2009), p. 111. DOI: 10.1088/1126-6708/2009/09/111. arXiv: 0907.4076 [hep-ph]. Erratum: in: *JHEP* 02 (2010), p. 011. DOI: 10.1007/JHEP02(2010)011.

[95] G. Aad et al. "Test of the universality of τ and μ lepton couplings in W-boson decays with the ATLAS detector". In: *Nature Phys.* 17 (2021), p. 813.

[96] ATLAS collaboration. "Test of the universality of τ and μ lepton couplings in W-boson decays with the ATLAS detector". In: *Nature Physics* 17.7 (2021), pp. 813–818. URL: https://www.nature.com/articles/s41567-021-01236-w.

[97] *TRexFitter framework for binned template profile likelihood fits.* available for CERN users only. URL: https://trexfitter-docs.web.cern.ch/trexfitter-docs/.

[98] ATLAS Collaboration. *Test of Lepton Flavour Universality in the decays of top quark to τ lepton or electron*. ATL-COM-PHYS-2023-328. 2023. URL: https://cds.cern.ch/record/2857873/.

[99] ATLAS Collaboration. *Measurement of the ratio of branching fractions of W-boson decays to τs and muons in $t\bar{t}$ events with the ATLAS detector*. ATL-COM-PHYS-2019-212. 2019. URL: https://cds.cern.ch/record/2667199/.

[100] M. Bähr et al. "Herwig++ physics and manual". In: *Eur. Phys. J. C* 58 (2008), p. 639. DOI: 10.1140/epjc/s10052-008-0798-9. arXiv: 0803.0883 [hep-ph].

[101] Johannes Bellm et al. "Herwig 7.0/Herwig++ 3.0 release note". In: *Eur. Phys. J. C* 76.4 (2016), p. 196. DOI: 10.1140/epjc/s10052-016-4018-8. arXiv: 1512.01178 [hep-ph].

[102] *Run 2 Top PDF recommendations*. URL: https://twiki.cern.ch/twiki/bin/viewauth/AtlasProtected/TopMCPDFReccommendations.